UNIVERSITY OF CALIFORNIA,
IRVINE

Transdermal Micro-Implantable Metabolite Sensor with Optical Communication

DISSERTATION

submitted in partial satisfaction of the requirements
for the degree of

DOCTOR OF PHILOSOPHY

in Biomedical Engineering

by

John Warren Weidling

Dissertation Committee:
Professor Elliot Lawrence Botvinick, Chair
Associate Professor Bernard Choi
Assistant Professor Elliot Hui
Associate Professor Jonathan Lakey

2014

DEDICATION

To

my wife

I bet you didn't realize quite how long it would take when you suggested that I follow my scientific interests and get a PhD. I never believed I could be at this place before I met you. Thank you for giving me this experience and providing the most amazingly fulfilling support and love throughout my journey.

and my parents

Thank you for allowing me the freedom to find out who I am, and helping me along my path in so many ways. You told me I could be as tall as I want to be; I feel very tall now, thanks to you.

"The fundamental thing is the opportunity to be creative"
Martin Rodbell, PhD
Nobel Prize in Medicine 1994

Thank you Professor Botvinick for providing me with abundant opportunity and instilling in me a thirst for knowledge and advancement of medical technologies.

TABLE OF CONTENTS

LIST OF FIGURES

ACKNOWLEDGMENTS

My committee chair, Dr. Elliot Botvinick, has an infectious exuberance for solving medical problems through invention and discovery. His guidance as well as his motivating enthusiasm were the main impetus to the completion of this work. I thank him for introducing me to his world and welcoming me into it with such openness.

I would like to thank my committee members, Professor Elliot Hui, Professor Jonathan Lakey, and Professor Bernard Choi, whose insights and questions led us down many crucial paths in the completion of this work.

I thank the lab of Dr. Matthew Brenner whose animal models and advice greatly advanced the completion of this work.

In addition, I thank all the students and other researchers who worked with me along the way. Special thanks to Dr. Samir Shreim, Princeton Saroha, Emilia de Alonso, Ben Lakey, Erik Noel, and Dr. Sean White.

CURRICULUM VITAE

John Warren Weidling

2008	B.S. in Mechanical Engineering, with a Focus in BioMechanical Engineering, University of Kansas
2008-2010	Corporate Management Trainee / Front Line Supervisor BNSF Railway, Inc.
2011-2013	Engineering Consultant, Metronom Health, Inc.
2012-2014	Graduate Student Researcher, Beckman Laser Institute, University of California, Irvine
2012	M.S. in Biomedical Engineering, University of California, Irvine
2014	PhD. in Biomedical Engineering, University of California, Irvine

FIELD OF STUDY

Continuous Optical Implantable Metabolite Sensors

PUBLICATIONS AND CONFERENCE PROCEEDINGS

Weidling, J., De Alonso, E., White, S., Botvinick, E. "Optical Continuous Lactate Monitor for Combat Casualty Care", Military Health System Research Symposium August 2014.

Weidling, J., Sameni, S., Lakey, J. R., & Botvinick, E. (2014). Method measuring oxygen tension and transport within subcutaneous devices. *Journal of biomedical optics*, *19*(8), 087006-087006.

Weidling, J., Botvinick, E. "Implantable Optical Continuous Lactate Sensor in Cyanide Poisoning Model", Annual meeting of the Biomedical Engineering Society, Seattle, WA September 2013

Weidling, J., Isikman, S. O., Greenbaum, A., Ozcan, A., & Botvinick, E. "Can capillaries grown in 3D culture be imaged without the use of an optical lens system?", Annual meeting of the Biomedical Engineering Society, Seattle, WA September 2013

Weidling, J., Isikman, S. O., Greenbaum, A., Ozcan, A., & Botvinick, E. (2012). Lens-free computational imaging of capillary morphogenesis within three-dimensional substrates. *Journal of biomedical optics*, *17*(12), 126018-126018.

Kniazeva, E., **Weidling, J. W.,** Singh, R., Botvinick, E. L., Digman, M. A., Gratton, E., & Putnam, A. J. (2012). Quantification of local matrix deformations and mechanical properties during capillary morphogenesis in 3D. *Integrative Biology*, *4*(4), 431-439.

ABSTRACT OF THE DISSERTATION

Transdermal Micro-Implantable Metabolite Sensor with Optical Communication

By

John Warren Weidling

Doctor of Philosophy in Biomedical Engineering

University of California, Irvine, 2014

Professor Elliot Lawrence Botvinick, Chair

Early warning of impending shock, organ failure, and hypoperfusion are critical to implementing an effective treatment approach in emergency medicine. However, vital signs often do not change until a patient is already in critical condition, and it is too late to intervene effectively. Blood lactate levels have been suggested as a more sensitive parameter for measuring a patient's condition, because lactate levels change early during life-threatening situations such as hemorrhagic shock and sepsis. In fact, frequent serial measurements of lactate over the course of treatment that guide a goal-directed therapy have been shown to decrease mortality rates significantly. Unfortunately, lactate guided treatment is rarely practiced due to the logistical burden of taking serial measurements using point-of-care devices or as part of a lab panel. To address this unmet need, a microchip device to continuously monitor lactate for the duration of inpatient care has been developed. It was found that the microchip could be made such that it is implanted just under the skin surface and an optical probe is used to measure the reported response on the skin surface by passing and receiving light through skin. The microchip responds to changes in lactate concentration by utilizing an enzyme with high specificity and selectivity

for lactate. A molecule that reports the enzyme-mediated response is embedded in the microchip. Manufacturing techniques have been developed to reproduce the microchips effectively, and the chips have been tested for use and accuracy in rabbit models of cyanide poisoning, where lactate levels change rapidly. The microchip platform has the ability to be loaded with alternate chemistries for detecting other bio-analytes, such as glucose, oxygen, CO_2, pH, etc. An optical probe suitable for passing light through skin and receiving the microchip light emission for use in animal studies was created along with software to analyze the emission signals. When calibrations of implanted chip response to lactate were compared to gold-standard blood lactate measurements across the physiological and pathological range in 12 separate models of cyanide poisoning in rabbits the average error was 11%.

INTRODUCTION

The use of light to interrogate and interact with biological phenomena continues to be a growing field of study. This is because light is generally less invasive/destructive than other approaches (such as removing fluids or tissues for analysis, or inserting objects, such as electrodes for measurement of biological properties) and interacts with individual molecules and atoms providing exquisitely fine detail in some cases. Light, in many forms, is used in medicine from diagnosis through treatment. Markers that interact or bind to specific biological components and have unique optical properties have made diagnosis through histology and rapid assays possible. In this work, I have used light as a measurement tool in basic research of cellularized constructs and *in vivo* studies to determine: stiffness near capillary tip cells, concentration of oxygen inside implanted gels, and concentration of lactate in tissue under pathological conditions. My work with cell mechanics and imaging prepared me for the bulk undertaking and main focus of my thesis: the measurement of lactate using an optic-based implant.

The main results of my findings are as follows:

- Stiffness of fibrin extra-cellular matrix (ECM) near capillary tips is higher than surrounding area as measured by microrheology of ECM material.
- Capillaries grown in 3-dimensional culture can be imaged without the use of lenses, which could enable low-cost high-throughput imaging for drug-screening platforms.
- Oxygen-sensitive dyes (metallo-porphyrins) can be measured through tissue with LEDs and a large area photodetector. Oxygenation/perfusion of implants can be measured using this technique

- In redox based bio-analyte sensors, multiplexing small reaction chambers increases signal without changing response time or sensitivity range.
- Lactate was measured continuously through tissue from an implanted sensor in rabbits subjected to cyanide poisoning.

Chapter One

Measuring the Growing Capillary's Environment

I began my work with light and biology by studying the effects of external mechanics on cellular processes on a micro-scale. A series of experiments was performed to determine 1) A measurement of the ECM stiffness near capillary tip cells (<20 micron from tip cells) and 2) the effect of changes in environmental matrix stiffness on capillary growth. A former professor of the biomedical engineering department at UCI, Dr. Andrew Putnam, had worked extensively on the relationship between capillaries and their ECM. His group had found that as ECM concentration was increased beyond typical *in vivo* values that capillary growth was inhibited(Ghajar et al., 2008). The increase in ECM concentration increased the stiffness of the ECM, decreased the pore size, and increased the number of binding sites for proteins and other substances. Dr. Putnam wondered what factor comprised the main mechanism of the growth inhibition, but first he needed to know what the cells were experiencing, mechanically, on a magnitude scale relevant to a single cell. He knew that common macro-rheology used to determine the bulk stiffness of hydrogels would not provide him with the detail needed to answer his question. Dr. Putnam also knew that a Dr. Elliot Botvinick was building, in his lab at UCI, a system capable of measuring hydrogel stiffness around an area of about 3-6 square microns, called a micro-rheometer. Macro-rheology, in comparison, measures hydrogel stiffness on the order of $1.76*10^8$ square microns. With this knowledge, Dr. Putnam asked the Botvinick lab to measure the stiffness around capillary tip cells to determine what a growing cell would feel.

One of my first tasks in the lab was to grow capillaries in petri dishes and measure the ECM stiffness near tip cells. In order to measure the ECM stiffness within 20 microns of capillary tip cells I had to use a method of mechanical measurement on a very small scale called Active Micro-Rheology (AMR). I was trained on the use of the Botvinick lab AMR system and the culture of capillary bead assays used to grow finite groups of capillaries in 3-dimensions *in vitro*. In collaboration with Dr. Putnam's PhD student Ekaterina Kniazeva, I added my findings from the AMR measurements of ECM stiffness near capillary tip cells to her findings on other factors involved in ECM remodeling during capillary growth. The results were published in the Journal of Integrative Biology, April 2012(Kniazeva et al., 2012). Reprinted with permission:

1.1

Quantification of local matrix deformations and mechanical properties during capillary morphogenesis in 3D‡‡

Ekaterina Kniazeva,[a] John W. Weidling,[a] Rahul Singh,[b] Elliot L. Botvinick,[a] Michelle A. Digman,[c] Enrico Gratton,[a] andAndrew J. Putnam
[a]Biomedical Engineering Department, Natural Sciences II, Room 3201, University of California, Irvine, Irvine, CA 92697-2715
[b]Department of Biomedical Engineering, 2154 Lurie BME Building, 1101 Beal Ave., University of Michigan, Ann Arbor, MI 48109-2110., Email:ude.hcimu@mantup; Fax: 734-647-4834; Tel: 734-615-1398
[c]Department of Developmental and Cell Biology, Natural Sciences II, Room 3204, University of California, Irvine, Irvine, CA 92697-2715

Abstract

Reciprocal mechanical interactions between cells and the extracellular matrix (ECM) are thought to play important instructive roles in branching morphogenesis. However, most studies to date have failed to characterize these interactions on a length scale relevant to cells, especially in three-dimensional (3D) matrices. Here we utilized two complementary methods, spatio-temporal image correlation spectroscopy (STICS) and laser optical tweezers-based active microrheology (AMR), to quantify endothelial cell (EC)-mediated deformations of individual ECM elements and the local ECM mechanical properties, respectively, during the process of capillary morphogenesis in a 3D cell culture model. In experiments in which the ECM density was systematically varied, STICS revealed that the rate at which ECs deformed individual ECM fibers on the microscale positively correlated with capillary sprouting on the macroscale. ECs expressing constitutively active V14-RhoA displaced individual matrix fibers at significantly faster rates and displayed enhanced capillary sprouting relative to wild-type cells, while those expressing dominant-negative N19-RhoA behaved in an opposite fashion. In parallel, AMR revealed a local stiffening of the ECM proximal to the tips of sprouting ECs. By quantifying the dynamic physical properties of the cell-ECM interface in both space and time, we identified a correlation linking ECM deformation rates and local ECM stiffening at the microscale with capillary morphogenesis at the macroscale.

Introduction

Abnormal angiogenesis is present in a variety of pathological conditions ranging from cancerous tumors, psoriasis, blindness and arthritis, to heart and brain ischemia, neurodegeneration, hypertension, osteoporosis and heart disease.[1] The ability to control angiogenic sprouting within affected tissues is important to generate therapeutic solutions to these conditions. Acquiring a fundamental understanding of the interdependence of angiogenesis, tissue structural properties, and cell-ECM interactions may significantly enhance efforts to develop new approaches that promote healthy vessel formation.

Previous studies have demonstrated that ECM compliance influences cell-generated contractile forces in two-dimensional (2D) cell cultures.[2,3] These actin-mediated contractile forces are governed in part by the activity of the small GTPase RhoA, and appear to be a critical link between ECM mechanical properties and cell function in 2D.[4] RhoA and its signaling partners have also been implicated in capillary morphogenesis.[5,6]Previous 2D cell culture studies have shown that ECM ligand density can control growth and morphology of capillary formation[7] and that mechanical cues affect tubulogenesis.[8–10] In 3D tissues, we have studied how matrix density affects formation of blood vessels both *in vitro* and *in vivo*,[11–16] adapting a model first described by Nehls and Drenckhahn where ECs are grown on microcarrier beads within a fibrin matrix.[17]Fibrin is one of the major structural proteins involved in the provisional matrix during wound healing,[18] and thus provides an appropriate substrate for an angiogenesis model.

To better understand the reciprocal and dynamic nature of the cell-ECM interface and its effects on capillary morphogenesis, here we have employed two relatively sophisticated physics-based methods, STICS and AMR. STICS revealed that the rates at which nascent vessels exerted forces on the ECM at the micron and submicron length scales correlated with the phenotypic responses observed on the larger length scale. Furthermore, both sprouting and the rates of matrix deformation were maximized in gels whose concentration matched the physiologic concentration of fibrin in a provisional blood clot. AMR revealed that the ECM is locally stiffened at the tips of sprouting capillaries. Collectively, these two methods revealed a predictive new correlation spanning multiple length scales that describes the mechanochemical regulation of capillary sprouting in 3D.

Materials and methods

Quantification of capillary morphogenesis

This study exploited a fibrin-based 3D cell culture model of angiogenesis assembled as described in the electronic supplementary information (ESI†). The model yields robust networks of capillary-like structures with hollow, well-defined lumens,[13] and these structures are capable of forming functional anastomoses with host vessels upon implantation.[14] High-resolution images of sprouting capillary-like networks were obtained with an Olympus IX51 microscope, and quantified using Image J software (National Institutes of Health) as previously described.[15] A minimum of ten beads were randomly selected per condition, with only isolated beads quantified to avoid vessels anastomosing with neighboring networks. Total network lengths for each bead in each condition were then documented and averaged. The resulting plots of average total network length over time were generated using KaleidaGraph (Synergy Software, Reading, PA). A broad range of fibrin concentrations (1, 1.5, 2, 2.5, 5, 10 mg ml^{-1}), spanning the physiologic value (≈2.5 mg ml^{-1}) found in a provisional clot during wound healing,[19] was explored in this study.

Spatio-temporal image correlation spectroscopy: imaging and analysis

ECM displacements surrounding the nascent vessel-like structures were quantified using spatio-temporal image correlation spectroscopy (STICS). Fibrin-based constructs were imaged after 6 days of culture as this time point allowed for sufficient vessel development

in all conditions. Brightfield phase-contrast and confocal reflectance imaging were performed using an Olympus FluoView FV1000 confocal laser scanning microscope equipped with a 60X 1.2NA water immersion objective and an Argon Ion laser at 488 nm. The constructs were scanned every 15 s in a single focal plane for a total of 250 images for each condition, and these image stacks were sequentially compiled to generate videos of each data set. STICS was then applied to obtain velocity maps for individual fibers in a given ECM region of interest, and to derive the average velocity modulus of regions of ECM surrounding the sprouting vessels. STICS analysis was executed using an automated method within SimFCS software developed by the Laboratory for Fluorescence Dynamics (www.lfd.uci.edu). Complete mathematical derivation of the STICS analysis and extraction of velocity data has been published previously,[20] but a summary of the method can be found in the Supporting Material section.

STICS data presented in this manuscript were analyzed in blocks of 32 pixels by 32 pixels that overlap by 16 pixels (unless otherwise noted). Using relatively small regions allowed high resolution to be achieved within the resulting flow maps. SimFCS software displayed vector arrows to represent the rates of ECM displacement for each block, such that one arrow was placed in the center of each block. The length of the arrow directly corresponds to the magnitude of the velocity and the direction of the arrow corresponds to the direction of flow. Numerical data of this representation could be easily extracted within the software and velocity values are reported in μm h^{-1} within the final figures.

Quantification of ECM mechanical properties *via* macro- and microrheology

Macroscale mechanical characterization of the fibrin gels was accomplished *in situ* on an AR G2 rheometer (TA Instruments, New Castle, DE) equipped with a Peltier stage and 20 mm stainless steel parallel plate geometry. The Peltier stage was cooled to 4 °C, and 320 μL of fibrinogen solution was injected into a 1050 μm gap between the plate and stage. The edge of the plate was sealed with silicone oil (Arcos Organics, Morris Plains, NJ) to prevent evaporation and the top plate was lowered to 1000 mm. The temperature was increased from 4 °C to 37 °C over 5 min and then held at 37 °C for 45 min while the clotting was monitored at 1% strain and 1 rad s^{-1}. All gels fully clotted within 45 min as indicated by a plateau in G′. The viscoelastic properties of the hydrogel were examined by a frequency sweep from 1 to 100 rad s^{-1} at 1% strain, and the averages over the linear region (1 to 10 rad s^{-1}) of both G′ and G″ were recorded. This procedure was repeated five times at each concentration.

Mechanical properties within fibrin gels near and away from sprouting vessels were measured by AMR using a previously described system.[21] In AMR, we use a focused laser beam to optically trap a microbead that is embedded within a 3D matrix. The amplitude-phase response of the bead is recorded as the trapping beam is sinusoidally oscillated. For these experiments, the trapping beam was oscillated with an amplitude of 60 nm through frequencies 5, 10, 20 50, 75, and 100 Hz. The stiffness, G*, of the fibrin matrix was calculated as previously described.[21] Silica beads of 2 μm diameter were mixed into fibrinogen solutions prior to polymerization and assembly of the angiogenesis model inside 35 mm diameter glass-bottom Petri dishes (No. 1.5 glass, MatTek). This resulted in a disperse distribution of silica beads within the fibrin-based angiogenesis model, where

each bead could be manipulated by laser tweezers for AMR measurements. On day 6 (consistent with the STICS measurements), G was measured near to capillary tips (within 20 μm) and far from capillaries (greater than 500 μm away).

Modulation of EC-generated tractional forces

EC-generated tractional forces were modulated in two ways. The first involved the expression of genetic constructs expressing constitutively active (V14) or dominant negative (N19) mutants of the small GTPase RhoA. Cells expressing GFP were used as a control. HUVECs were treated with appropriate adenoviral supernatants 3 days prior to fibrin tissue assembly to yield cultures that were 70% infected as determined by GFP expression. A RhoA G-LISA assay (Cytoskeleton, Denver, CO) was performed using HUVEC lysates to confirm the expected up- or down-regulation of RhoA activity (ESI†, Fig. S2). The second approach involved direct application of one of the following compounds to the tissue constructs with every media change: Y27632 (30 μM; Calbiochem, La Jolla, CA), which inhibits the Rho-associated protein kinase (ROCK) and thus ROCK-mediated myosin light chain phosphorylation;[22] BDM (10 mM; Calbiochem), which inhibits the myosin ATPase downstream of myosin light chain phosphorylation;[23] ML-7 (10 μM; Sigma-Aldrich, St. Louis, MO), a potent and selective inhibitor of myosin light chain kinase;[24] and blebbistatin (50 μM; Calbiochem), which preferentially binds to the myosin ATPase intermediate with ADP and phosphate bound at the active site and slows down phosphate release.[25] Drug concentrations were based on previous literature, as well as dose-response studies performed in our lab.

Statistical analysis

Statistical analyses were performed using KaleidaGraph (Synergy Software). Data were represented as mean total network length ± standard deviation for angiogenesis quantification. ECM displacement data is represented as average velocity ± standard deviation. G-LISA data is shown as normalized RhoA activity levels ± standard deviation. A one-way analysis of variance (ANOVA) was performed to assess statistical significance among data sets. Statistical significance was assumed when $p < 0.05$.

Results

Characterizing ECM displacements *via* spatio-temporal image correlation spectroscopy

A major goal of this study was to determine if the effects of EC-mediated contractile forces could be quantified on a length scale relevant for individual cell-ECM interactions during capillary morphogenesis. To achieve this goal, we performed STICS analysis[26] on sets of confocal reflectance images (Fig. 1A). Using SimFCS software (www.lfd.uci.edu), image correlation analysis was performed on each stack of images in space and time, where each image within the stack was divided into 225 analysis regions, or boxes, each 32 by 32 pixels. A velocity vector was calculated for each of the boxes, compiled and represented as a detailed velocity map (Fig. 1B and C). These velocity maps provided a representation of both the magnitude and rates of displacements of individual ECM fibers under the influence

of cell-generated forces. In these experiments, the dynamic nature of individual filaments within the fibrin ECM was particularly striking (See ESI†, Movie S1, A–C).

To validate the method, STICS analysis was performed on acellular fibrin gels lacking EC-coated beads. Such experiments yielded extremely small velocity vectors, verifying that individual elements within the ECM move very little due to thermal fluctuations and environmental vibrations in the absence of any EC-generated tractional forces (Fig. 1D). Similarly, in tissues with EC-coated beads, STICS measurements far away from vessel sprouts showed very little matrix displacement (Fig. 1D). Another notable feature of the data was the observation that the direction of velocity vectors varied significantly within the 250-image stacks. This implies either that the cells both push or pull on the surrounding 3D matrix fibers within a relatively short period of time, or they do one or the other in a cyclic fashion (Fig. 1E).

After validating the STICS method in the context of capillary morphogenesis, we examined how changes in fibrin matrix density affect the rates at which ECs displace individual ECM elements and the effects of over-expressing constitutively-active (V14) and dominant-negative (N19) forms of RhoA in the ECs. (ECs expressing GFP were used as a vector control). We focused on areas of the ECM immediately adjacent to the tips of the vessels of interest, and tabulated average velocity moduli. The rates at which the ECs displaced individual ECM fibers depended heavily on fibrin concentrations, initially increasing as matrix density was increased from 1.0 mg ml^{-1} to 2.5 mg ml^{-1}, and then decreasing as the matrix density was increased further to 5 and 10 mg ml^{-1} (Fig. 2; see also Fig. 4A). In 3D cultures containing ECs expressing V14-RhoA, ECM velocities were significantly elevated relative to wild-type controls; by contrast, those containing ECs expressing N19-RhoA showed significant reductions in ECM velocities (Fig. 2). These effects were similar in all fibrin concentrations. Cells expressing GFP alone displaced the ECM no differently than wild-type cells. Representative videos of raster scanned image stacks for tissue constructs containing ECs infected with each of the adenoviral vectors in 2.5 mg ml^{-1} fibrin are shown in the Supplementary Information (ESI†,Movie S1, A–C). Similar data were also acquired for tissue cultures treated with contractile inhibitors; constructs in which cell-generated forces were inhibited with BDM, ML-7, Y27632, or blebbistatin exhibited lower displacement rates of individual ECM elements compared to untreated controls (ESI†, Fig. S2).

Rates of ECM displacement correlate with angiogenic vessel sprouting

To better understand how ECM displacement rates might relate to the overall outcome of capillary morphogenesis, we quantified the magnitude of capillary formation in our assay as a function of fibrin concentration and with ECs expressing mutant forms of RhoA. Across all matrix conditions, the trends show that capillary morphogenesis achieved by ECs over-expressing V14-RhoA was greater than that achieved by wild-type cells, with significant increases in 2, 2.5, 5, and 10 mg ml^{-1} fibrin gels (Fig. 3A–F). By contrast, morphogenesis decreased in cultures containing ECs expressing N19-RhoA, with significant reductions relative to wild-type cells in a subset of matrix compositions (Fig. 3A–F). Cells expressing GFP alone formed capillary networks to the same extent as wild-type cells. Furthermore, consistent with our published results,[12,13] increasing fibrin concentration from 2.5 to 10 mg

ml^{-1} caused a significant reduction in capillary sprouting (Fig. 3D–F; see also Fig. 4B and D). However, perhaps unexpectedly, fibrin concentrations lower than 2.5 mg ml^{-1} also caused significant reductions in capillary sprouting (Fig. 3A–C; see also Fig. 4B and D).

When these macroscale metrics of morphogenesis were combined with the microscale STICs data shown in Fig. 2 and simply replotted, the data reveal that the fibrin concentration at which the rate of cell-mediated ECM deformation is maximized (Fig. 4A) is the same concentration found to be most optimal for angiogenic sprouting (Fig. 4B). The combination of the data reveals a positive and somewhat linear correlation between the rates of matrix deformation and the extent of capillary sprouting (Fig. 4C). Pairwise statistical comparisons for both ECM deformation rates and total network lengths as a function of ECM concentration for each EC condition (control, V14, N19, and GFP) are shown in tabular form in Fig. 4D, with significant differences ($p < 0.05$) highlighted in gray.

ECM Velocities are a function of vessel proximity and location

To define the limits within which the EC-generated contractile forces can propagate through the ECM, we again applied STICS to investigate the dependence of ECM velocity on vessel proximity and location relative to the vessel tip. These experiments were limited to the optimal 2.5 mg ml^{-1} matrices. The imaged regions spanned larger areas around the vessel tips as well as ECM lateral to the vessel stalks (Fig. S3A-B). Each set of images was divided into four quadrants, or fragments, which were then analyzed separately to make the STICs computations more tractable (Fig. S3A-B). In tissue constructs containing ECs expressing the mutant forms of RhoA, the results mirror those obtained only by looking proximal to the sprouting tips (Fig. 2). Specifically, the rates of ECM deformation lateral to the vessel stalks were highest in fragment 1 (closest to the vessel tip), elevated in conditions containing ECs expressing V14-RhoA, and diminished when ECs expressed N19-RhoA. The rates of ECM deformation dropped off significantly as the distance from the vessel tip increased (Fig. S3C). Similarly, ECM velocities decreased significantly as the distance from the vessel tip increased from fragment 4 to fragment 1 (Fig. S3D). These data suggest that the EC-generated contractile forces propagate into the surrounding ECM up to at least 200 μm (the size of the image analyzed in this part of the study). ECM displacements were observed even in locations lateral to the vessel stalk, suggesting significant cell-ECM interactions along the entirety of the vessel.

Microrheology reveals local stiffening of the matrix near the tips of sprouting capillaries

Finally, to complement our STICS-based methodology, we also utilized laser tweezers-based active microrheology (AMR) to quantify local changes in the mechanical properties of the ECM during the process of capillary morphogenesis. We first performed macroscale shear rheology to confirm that increasing the fibrin matrix density across the range from 1 to 10 mg ml^{-1} increased the bulk mechanical properties of our gels. As expected, the shear elastic modulus, G′, of the gels increased monotonically as the fibrin content of the gels increased (Fig. 5A). We then performed AMR experiments only in the 2.5 mg ml^{-1} fibrin gels based on our data showing this concentration optimally supported capillary sprouting (Fig. 4). The AMR methodology yielded two interesting results. First, the data showed that the presence of the cells significantly increased the baseline shear elastic modulus (G′) of

the fibrin matrix (Fig. 5B), with values in the range from 100–700 Pa. By comparison, macroscale shear rheology of acellular gels showed that 2.5 mg ml^{-1} acellular fibrin gels have a shear elastic modulus of about 25 Pa (Fig. 5A). We have previously shown that the G′ values of acellular 2.5 mg ml^{-1} fibrin gels obtained from AMR are not statistically different than those obtained by macroscale shear rheology;[21] therefore, we attribute the observed differences in G′ to pre-stress imposed by the presence of the cells, rather than due to differences in the scale of the two different measurements. Second, we observed significant differences in the magnitudes of the local shear elastic moduli of fibrin gels depending on the proximity of the measurements to the sprouting capillaries (Fig. 5B), with mean values of G′ close to the vessellike structures nearly 2x higher than those values obtained from locations more than 500 μm away from a nascent sprout. This latter observation suggests a very significant pericellular stiffening of the ECM proximal to the tips of the sprouting capillaries.

Discussion

Endothelial cell-generated tractional forces, balanced by the ECM's resistance to those forces, have long been proposed to modulate angiogenesis.[7] There is now strong experimental evidence to support this hypothesis, with traction forces linked to endothelial cell branching,[27] the formation of capillary-like structures,[8,9,15] and the transcriptional control of soluble proangiogenic molecules.[28] In recent years, it has also been fairly well established that ECM physical property changes correlate with changes in single cell phenotype.[29,30]However, most studies have relied on bulk mechanical property measurements to characterize the ECM, while only a few have attempted to characterize the local properties of the cell-ECM interface. In this study, we utilized a combination of methods to quantitatively investigate the local dynamics of the cell-ECM interface during angiogenic sprouting in a 3D ECM.

The first method we used, spatio-temporal image correlation spectroscopy, enabled the locations of individual matrix elements to be tracked as a function of time. This time- and position-dependent information provided quantification of the rates at which individual matrix fibers were displaced due to traction forces generated by sprouting ECs. We chose day 6 for our STICS analysis because there was sufficient vessel development in all conditions by this time point. The sprouting vessel tips were adequately separated from the microcarrier beads and could therefore be imaged and analyzed without the actual beads disrupting the measurements. Furthermore, ECs in this assay are actively forming capillaries at this time point, as we have shown previously.[12,13,15] This is reinforced by the data in Fig. 3, which show that the total vessel network lengths across all matrix conditions more than double from day 6 to day 9. Combining STICS with our total network length metric of capillary morphogenesis revealed a surprising, and previously unobserved, correlation: that maximal capillary sprouting occurs in matrices that can be most rapidly displaced by cells. Particularly notable was the fact that maximal capillary sprouting (quantified on a millimeter length scale) and maximal matrix deformation rates (quantified on a micron length scale) occurred in fibrin gels whose concentration closely matched the physiological conditions found in native fibrin clots.[19]

This positive correlation between maximal sprouting and matrix deformation rates was identified by performing complementary experiments in which either cell generated tractional forces or the ECM's resistance to those forces was modulated. Tractional force generation was manipulated either genetically by expressing mutant forms of RhoA or pharmacologically through the use of several small molecule inhibitors of contractility. ECs expressing constitutively active RhoA reproducibly displayed increased capillary formation across a range of ECM conditions (as measured by total network length) when compared to wild-type controls (Fig. 3). By contrast, ECs expressing dominant negative RhoA showed reduced capillary morphogenesis. We have previously shown that inhibiting contractile force generation pharmacologically disrupts capillary growth and stability.[15] The data here show that ECs expressing V14-RhoA displace the ECM at significantly faster rates than do wild-type or GFP-sham controls (Fig. 2). Cells expressing N19-RhoA (Fig. 2) and those treated with contractile inhibitors (Fig. S2, ESI†) showed reduced matrix displacement rates across all ECM conditions, with significant differences relative to control cells in a subset of conditions.

The ECM's mechanical resistance to cell generated tractional forces was modulated by varying the density of the fibrin gels (Fig. 5A). Optimal angiogenic sprouting and maximal rates of ECM displacement occurred in 2.5 mg ml^{-1} fibrin gel constructs. In lower density gels, angiogenic sprouting and the rates of ECM displacement were reduced; similar reductions were observed in gel concentrations above this 2.5 mg ml^{-1}threshold (Fig. 4). This same type of biphasic dependency was previously reported in 2D cell migration studies.[31] Two possible explanations may account for the results in lower density gels. Either these mechanically weaker gels do not provide sufficient mechanical resistance to the cell-generated forces, or they lack sufficient cell binding sites to promote the formation and maintenance of the capillary networks. In the higher density gels, which are both mechanically stronger and theoretically provide an increased number of adhesive binding sites, diffusion limits imposed by the increased numbers of fibrin fibers may also play a significant role in decreased vessel formation.[12] Our current study cannot discern between these different possibilities, but did not aim to do so, in part because these parameters are also lumped together in native clots *in vivo*. Instead, the positive correlation identified here between local matrix deformation rates on the microscale and morphogenesis on the macroscale suggests that both softer and stiffer matrices may be incapable of supporting maximal capillary sprouting in part because the rates at which cells displace them are suboptimal.

We also used the STICS methodology to characterize the distance over which EC-generated tractional forces can propagate within the surrounding ECM. Our data clearly indicate that as the distance from the side of the vessel and in front of the vessel tip is increased, the matrix displacement rates fall off significantly within the first 200 mm (Fig. S3). A recent study by Winer *et al.* demonstrated that tractional stress exerted on the ECM by a single cell can create a local ECM stiffness gradient and provide a means for mechanical interaction with other cells up to 5 cell lengths from their periphery.[32] The distances over which EC-generated tractional forces propagate are of a similar magnitude. However, our current experimental set-up limits the amount of area surrounding the vessel that can be

imaged and subjected to STICS. Analyzing greater areas might allow the actual propagation limit to be better pinpointed.

The STICS analysis utilized here was also limited to images generated from a single plane. Using 2D fibronectin-modified polyacrylamide gels substrates, Maskarinec *et al.* showed that cell-induced displacements in the *z* direction can be comparable to, or greater than, those in the *xy* plane.[33] Thus, characterizing the movement of the matrix surrounding the entirety of the vessel in *x*, *y*, and *z* planes could conceivably provide even more insights regarding the role of cell-ECM mechanics, but implementing STICS in 3D is computationally challenging.

Complementing STICS, our experiments using AMR revealed a significant pericellular stiffening of the ECM proximal to the sprouting capillary-like structures (Fig. 5B). Gjorevski and Nelson reported something similar in the context of mammary epithelial morphogenesis, showing that branching initiates from sites of high mechanical strain.[34] However, translating metrics of strain into measures of stress requires some simplifying assumptions about the mechanical properties of the matrix, many of which may be incorrect for fibrillar matrices derived from naturally-occurring biopolymers (*e.g.*, Matrigel, collagen, fibrin). The most common assumption is that the ECM behaves largely in a homogeneous fashion. However, our AMR data here, sampling multiple different beads within a given gel, reveal that the local viscoelastic properties are highly heterogeneous (as demonstrated by the range of values in Fig. 5B). One approach to overcoming this issue is to use an amorphous synthetic gel whose properties are much more homogeneous. A recent study by Legant, *et al.* did just that, translating bead displacements in a 3D hydrogel with well-defined elastic properties into tractional forces and essentially achieving 3D traction force microscopy.[35] However, our approach using AMR enables the local mechanical properties of individual filaments within a 3D ECM to be directly measured, an essential step towards achieving 3D traction force microscopy in fibrillar ECMs. In the future, we envision combining STICS (to quantify strain imposed by cells on the ECM) with AMR (to quantify local G⍰) to quantitatively assess the distribution of cell-generated stresses during capillary morphogenesis, without the need for any simplifying assumptions.

Finally, it is important to acknowledge that we have simplified this study by ignoring the impact of cell-mediated ECM remodeling on matrix deformation rates and local mechanical properties. We have previously examined the role of matrix remodeling in more detail in previous studies.[13,15,36,37] Here, we chose to focus on a single time point, rather than assessing how these local matrix properties evolve as a function of culture time. Importantly, combining STICS and AMR in a future longitudinal study will enable us to better understand how local ECM remodeling alters the mechanical microenvironment in which a cell resides, something that existing macroscale methods cannot provide.

Conclusions

In conclusion, this study used a sensitive image correlation method and micro-scale rheology to quantitatively monitor ECM displacements and local mechanical properties within a 3D tissue during the complex multicellular process of capillary morphogenesis.

The first of these methods uncovered a multiscale correlation linking fibrin concentration, cell-generated matrix displacement rates, and capillary sprouting, while the second revealed significant local stiffening of the ECM near the tips of the nascent capillaries. Quantifying the local mechanical information content of the cell-ECM interface in both space and time using the approaches developed here may enable the mechanochemical regulation of other complex morphogenetic processes in 3D to be carefully and systematically characterized.

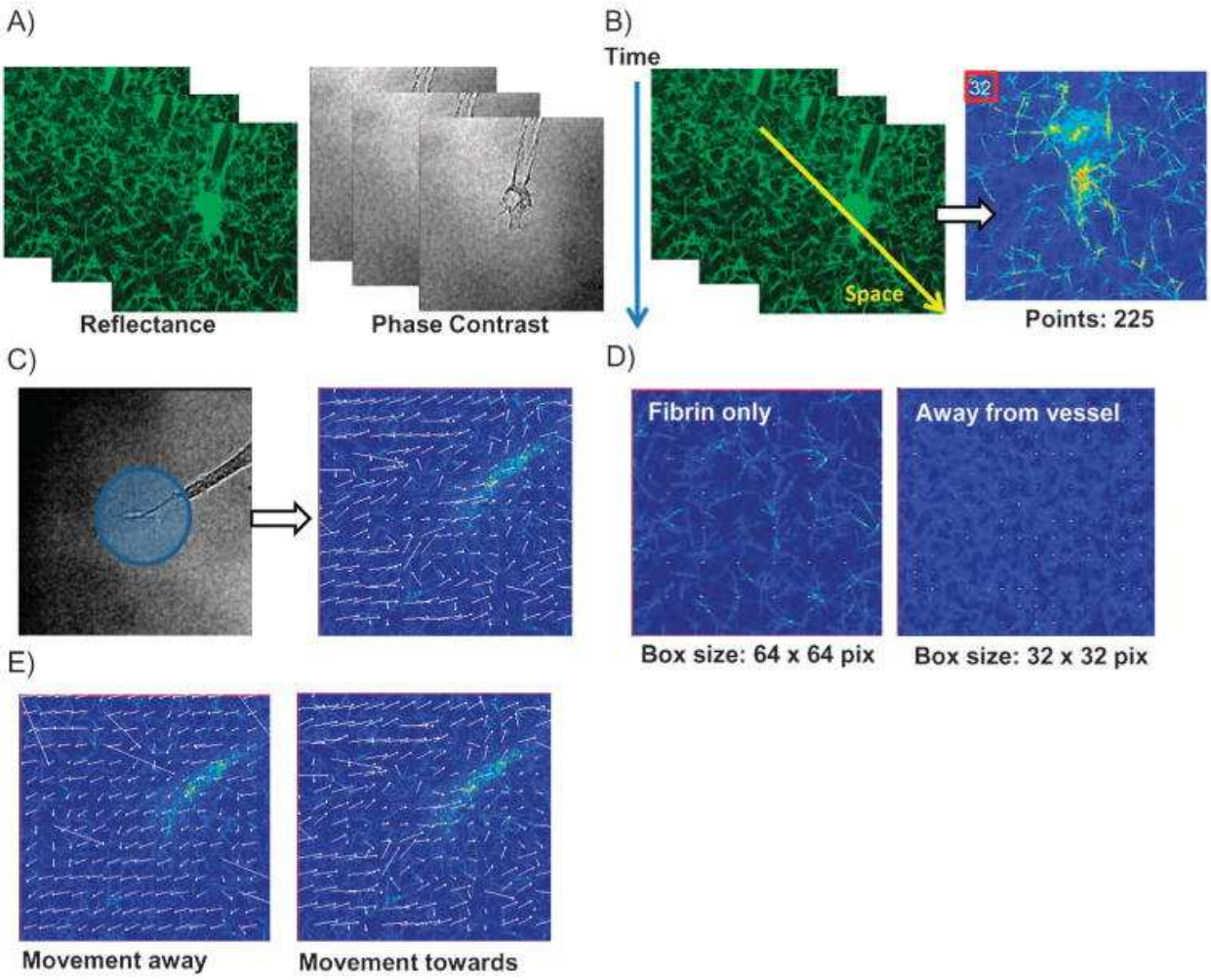

Figure 1: STICS experimental set-up. (A) Typical data output set, image dimensions 105 × 105 μm. (B) Spatio-temporal image correlation spectroscopy analysis diagram, right image dimensions 52.5 × 52.5 μm. (C) Final velocity map obtained *via* STICS analysis; left image is 105 × 105 μm, right image is 52.5 × 52.5 μm. (D) Verification of minimal matrix displacement within acellular fibrin (left) and far away from a sprouting vessel (right); images are 52.5 × 52.5 μm. (E) Evidence of the surrounding matrix moving away (left) or towards (right) the vessel; images are 52.5 × 52.5 μm. All representative images are within 2.5 mg ml^{-1} fibrin.

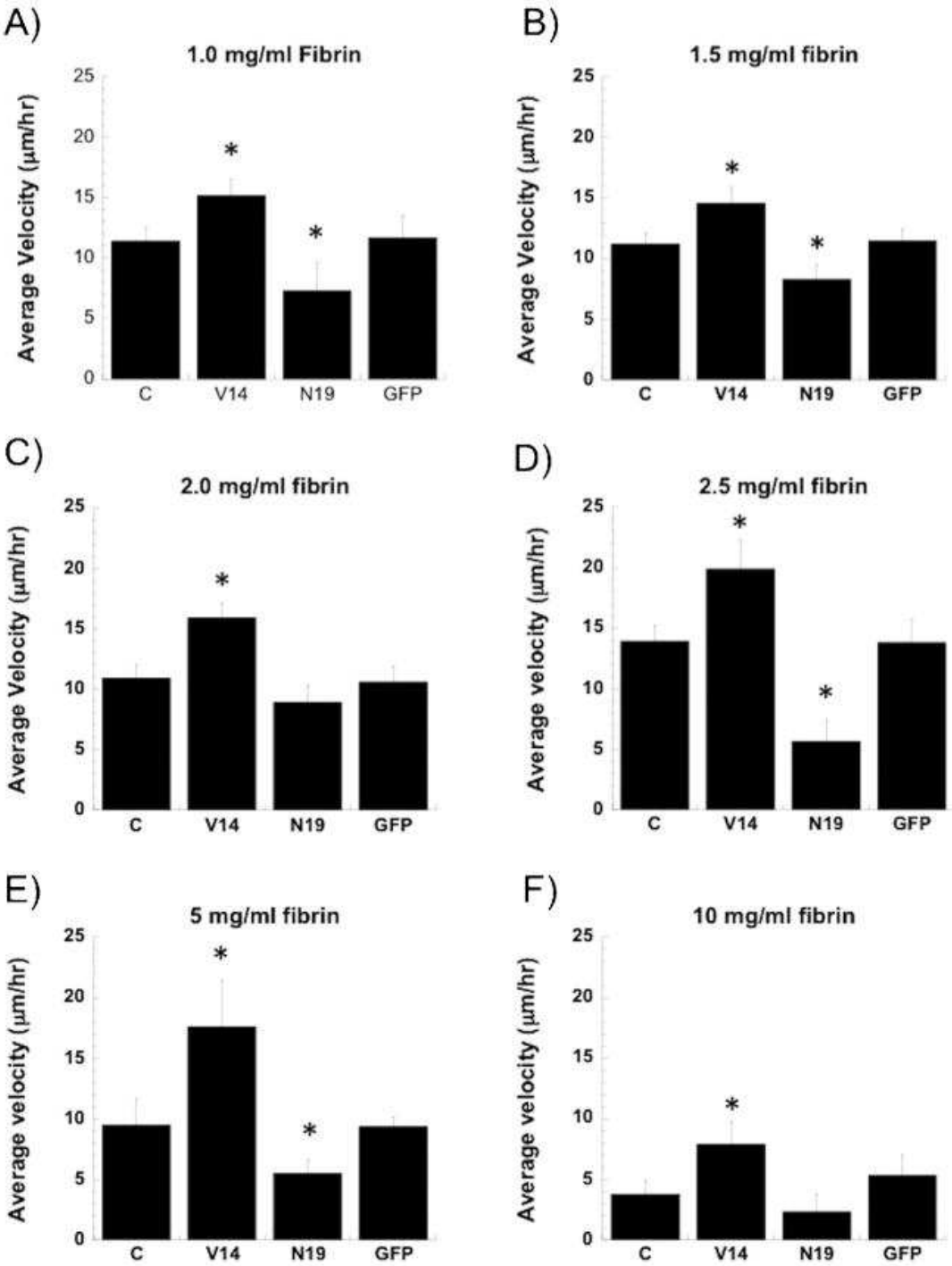

Figure 2: STICS analysis of average matrix displacement velocity surrounding vessel tips in (A) 1.0 mg ml^{-1}; (B) 1.5 mg ml^{-1};(C) 2.0 mg ml^{-1}; (D) 2.5 mg ml^{-1}; (E) 5 mg ml^{-1}; (F) 10 mg ml^{-1} 3D fibrin tissues and analyzed at day 6. The *x*-axis labels indicate the type of HUVECs used in the assay, with "C" = wild type controls, "V14" = cells expressing constitutively active V14-RhoA, "N19" = cells expressing dominant negative N19-RhoA, and "GFP" = cells expressing GFP (as a sham control). For each graph, $N = 3$. The error bars represent standard deviation, with the asterisks indicating statistical significance ($p < 0.05$) between the marked test sample and the wild type control.

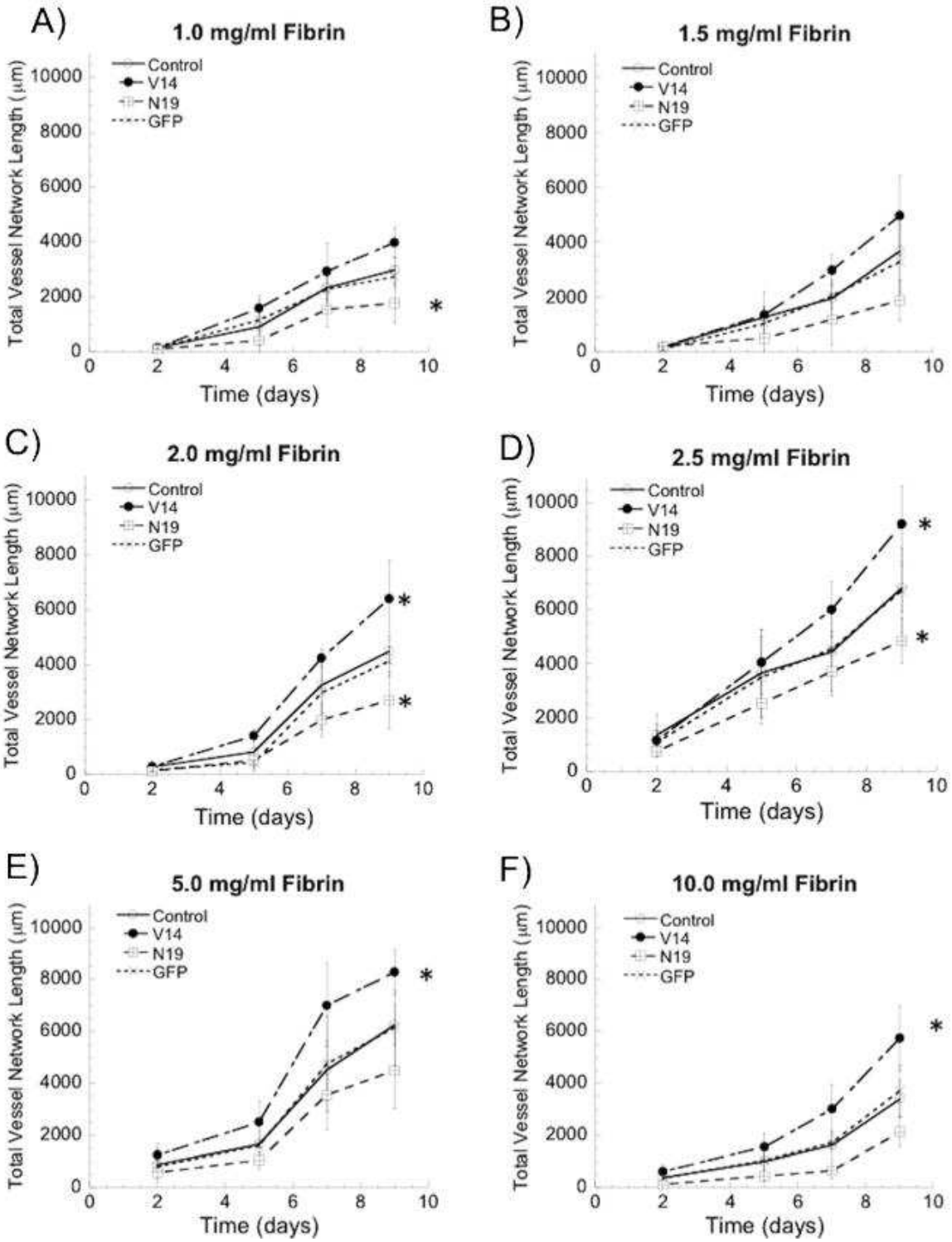

Figure 3: Quantification of total capillary network lengths by wild-type ECs (control) and ECs expressing V14-RhoA, N19-RhoA and empty vector GFP in (A) 1.0 mg ml^{-1}; (B) 1.5 mg ml^{-1}; (C) 2.0 mg ml^{-1}; (D) 2.5 mg ml^{-1}; (E) 5.0 mg ml^{-1}; (F) 10 mg ml^{-1} 3D fibrin tissues; $N = 10$ for each data point, error is represented as standard deviation, asterisk indicates statistical significance between associated control and test sample, such that $p < 0.05$.

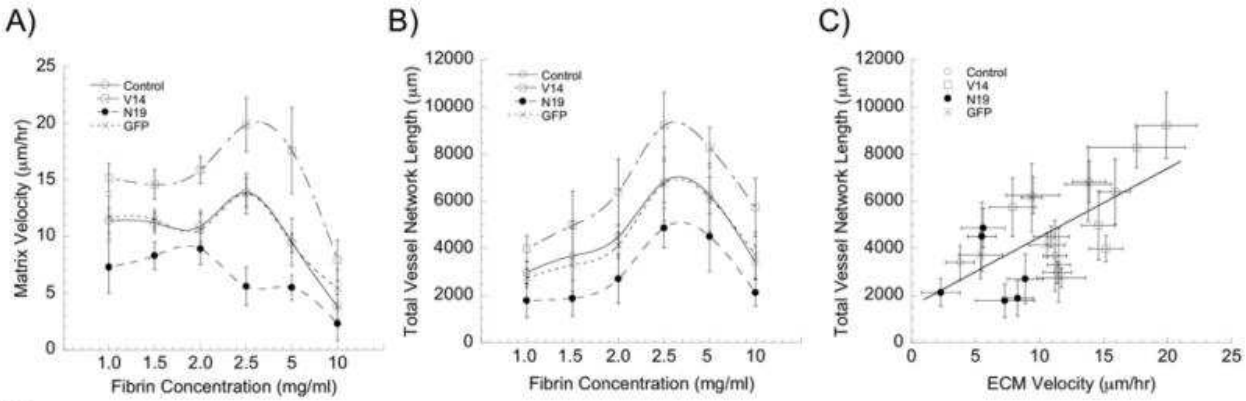

D)

Velocity

Figure 4A	1 and 1.5	1 and 2	1 and 2.5	1 and 5	1 and 10	1.5 and 2	1.5 and 2.5	1.5 and 5	1.5 and 10	2 and 2.5	2 and 5	2 and 10	2.5 and 5	2.5 and 10	5 and 10
Control	7.92E-01	6.39E-01	6.35E-02	2.33E-01	1.03E-03	7.75E-01	3.90E-02	2.68E-01	7.95E-04	5.31E-02	3.96E-01	2.42E-03	3.59E-02	4.53E-04	1.43E-02
V14	6.27E-01	5.17E-01	4.00E-02	3.56E-01	4.59E-03	2.75E-01	2.83E-02	2.68E-01	6.14E-03	6.01E-02	5.01E-01	2.81E-03	4.29E-01	2.17E-03	1.62E-02
N19	5.29E-01	3.59E-01	3.55E-01	2.87E-01	3.36E-02	6.15E-01	8.27E-02	3.75E-02	5.32E-03	5.71E-02	2.72E-02	4.73E-03	9.52E-01	6.39E-02	3.73E-02
GFP	9.16E-01	4.92E-01	2.29E-01	1.23E-01	1.31E-02	4.06E-01	1.21E-01	3.29E-02	5.19E-03	7.72E-02	2.56E-01	1.58E-02	1.82E-02	4.38E-03	4.38E-03

Network Length

Figure 4B	1 and 1.5	1 and 2	1 and 2.5	1 and 5	1 and 10	1.5 and 2	1.5 and 2.5	1.5 and 5	1.5 and 10	2 and 2.5	2 and 5	2 and 10	2.5 and 5	2.5 and 10	5 and 10
Control	1.80E-01	6.99E-07	4.27E-10	1.09E-09	1.50E-01	1.14E-01	1.95E-05	1.29E-04	5.93E-01	7.41E-07	7.61E-06	6.43E-04	1.46E-01	1.94E-08	9.25E-08
V14	6.04E-02	7.32E-05	2.05E-09	9.01E-11	6.54E-04	3.74E-02	3.06E-06	7.38E-06	2.14E-01	2.69E-04	1.83E-03	2.82E-01	8.98E-02	1.49E-05	4.62E-05
N19	7.53E-01	3.19E-02	5.96E-08	5.66E-05	2.50E-01	5.77E-02	1.39E-07	9.80E-05	4.33E-01	7.67E-05	5.78E-03	1.41E-01	5.07E-01	1.19E-07	1.75E-04
GFP	3.02E-01	4.48E-06	4.01E-07	1.23E-06	1.01E-02	1.22E-01	1.14E-04	4.84E-04	4.74E-01	1.13E-04	6.74E-04	2.52E-01	4.06E-01	7.11E-05	3.57E-04

Figure 4: Matrix displacement rates correlate with the extent of angiogenic sprouting. (A) Matrix displacement rates are modulated by alterations in RhoA activity, and are typically maximized in 2.5 mg ml^{-1} fibrin gels (except in the ECs expressing N19-RhoA). (Data replotted from Fig. 3; statistics represented therein). (B) Total vessel network lengths are similarly modulated by alterations in RhoA activity, and are maximized in 2.5 mg ml^{-1} fibrin gels. (Data replotted from Fig. 4; statistics represented therein). (C) Combining these data reveals a positive correlation between the rates of matrix deformation and the extent of capillary sprouting. (D) Significance tables showing the *p*-values for each pairwise comparison within a given EC group (control, V14, N19, and GFP) across the range of fibrin concentrations (significant differences are shaded gray).

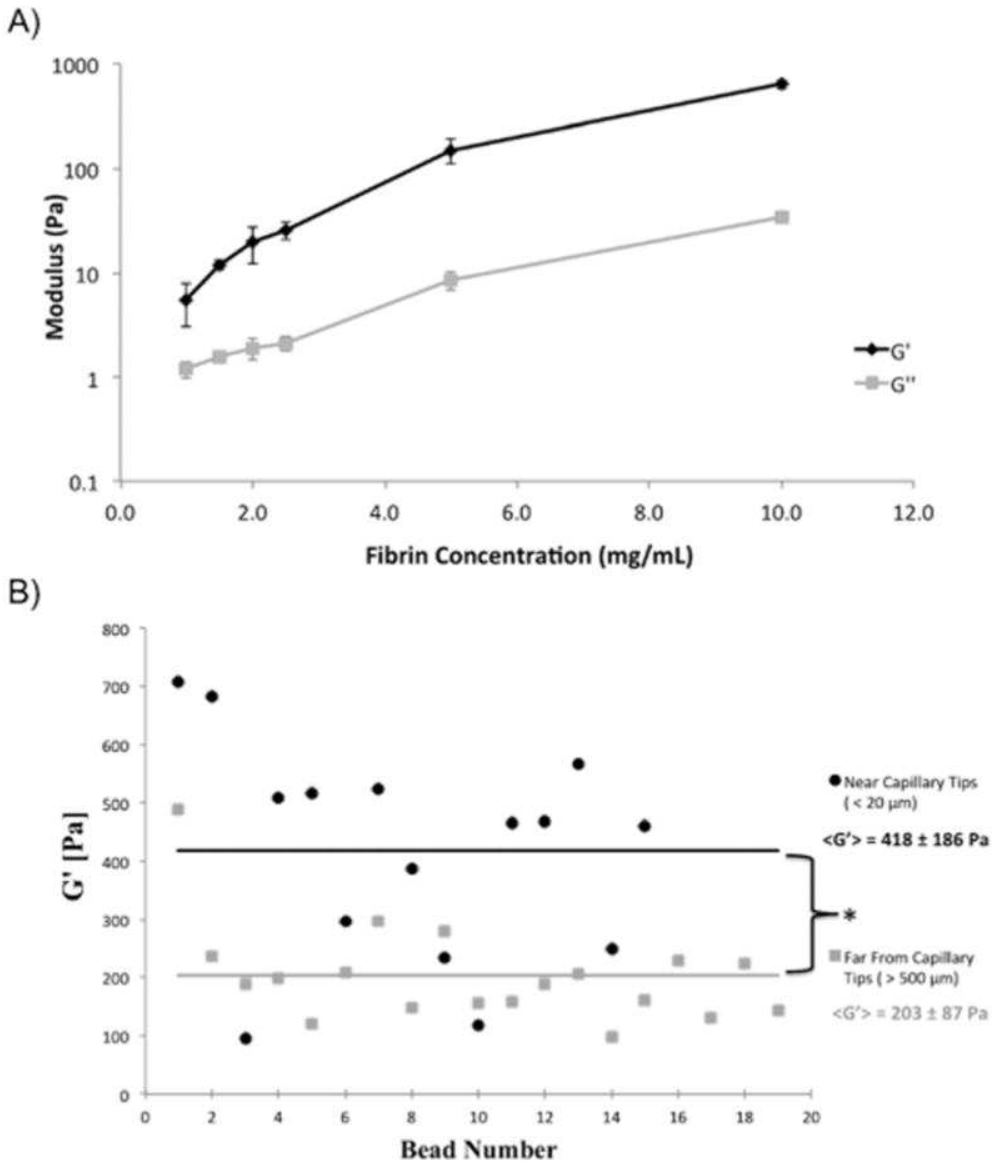

Figure 5: (A) Characterization of the macroscopic rheological properties of fibrin gels as a function of their concentration. The shear elastic (G′) and viscous (G″) moduli both increase with increasing fibrin concentration. $N = 5$ samples for each concentration; error is represented as standard deviation. All data points within a given data set (*i.e.*, all G′ values) are significantly different from each other ($p \ll 0.01$). (B) Active microrheology (AMR) in 2.5 mg ml^{-1} fibrin gel capillary morphogenesis model used to report local stiffness, G′, near to (<20 μm) and far from (> 500 μm) capillary tips. Each point is the averaged G′ value of one bead oscillated through a range of frequencies (5, 10, 20, 50, 75, and 100 Hz). G′ is calculated by tracking the bead's movement when a focused laser trap oscillates the bead at an amplitude of 60 nm at different frequencies. The solid lines represent the mean values of G′, which are highly significantly different (p = 8.74e-05).

References

1. Carmeliet P. Nat Med. 2003;9:653–660. [PubMed]

2. Lo CM, Wang HB, Dembo M, Wang YL. Biophys J. 2000;79:144–152. [PMC free article] [PubMed]

3. Reinhart-King CA, Dembo M, Hammer DA. Biophys J. 2005;89:676–89. doi: 10.1529/biophysj.104.054320. [PMC free article] [PubMed] [Cross Ref]

4. Shiu YT, Li S, Marganski WA, Usami S, Schwartz MA, Wang YL, Dembo M, Chien S. Biophys J.2004;86:2558–2565. [PMC free article] [PubMed]

5. Hoang MV, Whelan MC, Senger DR. Proc Natl Acad Sci U S A. 2004;101:1874–1879.[PMC free article] [PubMed]

6. Bayless KJ, Davis GE. J Biol Chem. 2004;279:11686–11695. [PubMed]

7. Ingber DE, Folkman J. Cell. 1989;58:803–805. [PubMed]

8. Sieminski AL, Hebbel RP, Gooch KJ. Exp Cell Res. 2004;297:574–584. [PubMed]

9. Deroanne CF, Lapiere CM, Nusgens BV. Cardiovasc Res. 2001;49:647–658. [PubMed]

10. Vailhe B, Lecomte M, Wiernsperger N, Tranqui L. Angiogenesis. 1998;2:331–344. [PubMed]

11. Griffith CK, Miller C, Sainson RC, Calvert JW, Jeon NL, Hughes CC, George SC. Tissue Eng.2005;11:257–266. [PubMed]

12. Ghajar CM, Chen X, Harris JW, Suresh V, Hughes CC, Jeon NL, Putnam AJ, George SC. Biophys J.2008;94:1930–1941. [PMC free article] [PubMed]

13. Ghajar CM, Blevins KS, Hughes CCW, George SC, Putnam AJ. Tissue Eng. 2006;12:2875–2888.[PubMed]

14. Chen X, Aledia AS, Ghajar CM, Griffith CK, Putnam AJ, Hughes CC, George SC. Tissue Eng A.2009;6:1363–1371. [PMC free article] [PubMed]

15. Kniazeva E, Putnam AJ. Am J Physiol: Cell Physiol. 2009;297:179–187. [PubMed]

16. Kniazeva E, Kachgal S, Putnam AJ. Tissue Eng A. 2011;17:905–14. doi: 10.1089/ten.TEA.2010.0275.[PMC free article] [PubMed] [Cross Ref]

17. Nehls V, Drenckhahn D. Microvasc Res. 1995;50:311–322. [PubMed]

18. Tonnesen MG, Feng X, Clark RAF. J Invest Dermatol Symp Proc. 2000;5:40–46. [PubMed]

19. Weisel JW. Science. 2008;25:456–457. [PubMed]

20. Rossow MJ, Mantulin WW, Gratton E. J Biomed Opt. 2009;14:024014. [PMC free article] [PubMed]

21. Kotlarchyk MA, Shreim SG, Alvarez-Elizondo MB, Estrada LC, Singh R, Valdevit L, Kniazeva E, Gratton E, Putnam AJ, Botvinick EL. PLoS One. 2011;6:e20201. doi: 10.1371/journal.pone.0020201.[PMC free article] [PubMed] [Cross Ref]

22. Ishizaki T, Uehata M, Tamechika I, Keel J, Nonomura K, Maekawa M, Narumiya S. Mol Pharmacol.2000;57:976–983. [PubMed]

23. Ostap EM. J Muscle Res Cell Motil. 2002;23:305–308. [PubMed]

24. Saitoh M, Ishikawa T, Matsushima S, Naka M, Hidaka H. J Biol Chem. 1987;262:7796–7801.[PubMed]

25. Kovacs M, Toth J, Hetenyi C, Malnasi-Csizmadia A, Sellers JR. J Biol Chem. 2004;279:35557–35563.[PubMed]

26. Hebert B, Costantino S, Wiseman PW. Biophys J. 2005;88:3601–3614. [PMC free article] [PubMed]
27. Fischer RS, Gardel M, Ma X, Adelstein RS, Waterman CM. Curr Biol. 2009;19:260–265.[PMC free article] [PubMed]
28. Mammoto A, Connor KM, Mammoto T, Yung CW, Huh D, Aderman CM, Mostoslavsky G, Smith LEH, Ingber DE. Nature. 2009;457:1103–1108. [PMC free article] [PubMed]
29. Engler A, Sen S, Sweeney H, Discher D. Cell. 2006;126:677–689. [PubMed]
30. Huebsch N, Arany P, Mao A, Shvartsman D, Ali O, Bencherif S, Rivera-Feliciano J, Mooney D. Nat Mater. 2010;9:518–526. [PMC free article] [PubMed]
31. Peyton SR, Putnam AJ. J Cell Physiol. 2005;204:198–209. doi: 10.1002/jcp.20274. [PubMed][Cross Ref]
32. Winer JP, Oake S, Janmey PA. PLoS One. 2009;4:6382. [PMC free article] [PubMed]
33. Maskarinec SA, Franck C, Tirrell DA, Ravichandran G. Proc Natl Acad Sci U S A. 2009;106:22108–22113. [PMC free article] [PubMed]
34. Gjorevski N, Nelson CM. Integr Biol. 2010;2:424–34. doi: 10.1039/c0ib00040j. [PMC free article][PubMed] [Cross Ref]
35. Legant W, Miller J, Blakely B, Cohen D, Genin G, Chen C. Nat Methods. 2010;7:969–971.[PMC free article] [PubMed]
36. Ghajar CM, Kachgal S, Kniazeva E, Mori H, Costes SV, George SC, Putnam AJ. Exp Cell Res.2010;316:813–25. doi: 10.1016/j.yexcr.2010.01.013. [PMC free article] [PubMed] [Cross Ref]
37. Kachgal S, Putnam AJ. Angiogenesis. 2011;14:47–59. doi: 10.1007/s10456-010-9194-9.[PMC free article] [PubMed] [Cross Ref]

1.2 Capillary Growth Aligns with the Direction of an Added Strain

In addition to the micro-rheology measurements published, I also observed the effects of changes in ECM stiffness on the alignment of capillary growth. Rather than increasing the concentration of ECM material to increase stiffness, I used a device designed by the Botvinick lab to stretch and compress ECM to create a stiffness gradient. The device consists of a frame with a well designed for insertion of a 35 mm petri dish, connected to an arm attached to a plastic post that inserts into the dish and can be rotated (Figure 1.1A). The petri dish can then be filled with a hydrogel containing cells which forms around the post and attaches to the post. The post can then be twisted after the gel is formed creating a stiffness gradient that moves out from the post (Figure 1.1B). Hence, the device was affectionately named Mr. Twisty. A description of the Mr. Twisty device was published in the journal PLoS one in 2011 (Kotlarchyk et al., 2011).

I used the same capillary bead assay described in my previous publication with the Putnam lab along with Mr. Twisty to observe the effects of the twist on capillary growth. Mr. Twisty was assembled with a glass bottom petri dish and the fibrin gel containing coated beads was formed in the dish and around the post. This was repeated for a second device. On day 2 of culture I rotated the post of one of the devices, while the other device was not rotated. Capillary growth continued for 7 days total and the dishes were imaged on day 7. The capillaries in the twisted dish grew in alignment with each other in a specific orientation, while the capillaries in the un-twisted dish grew in all directions (Figure 1.2).

Mr. Twisty

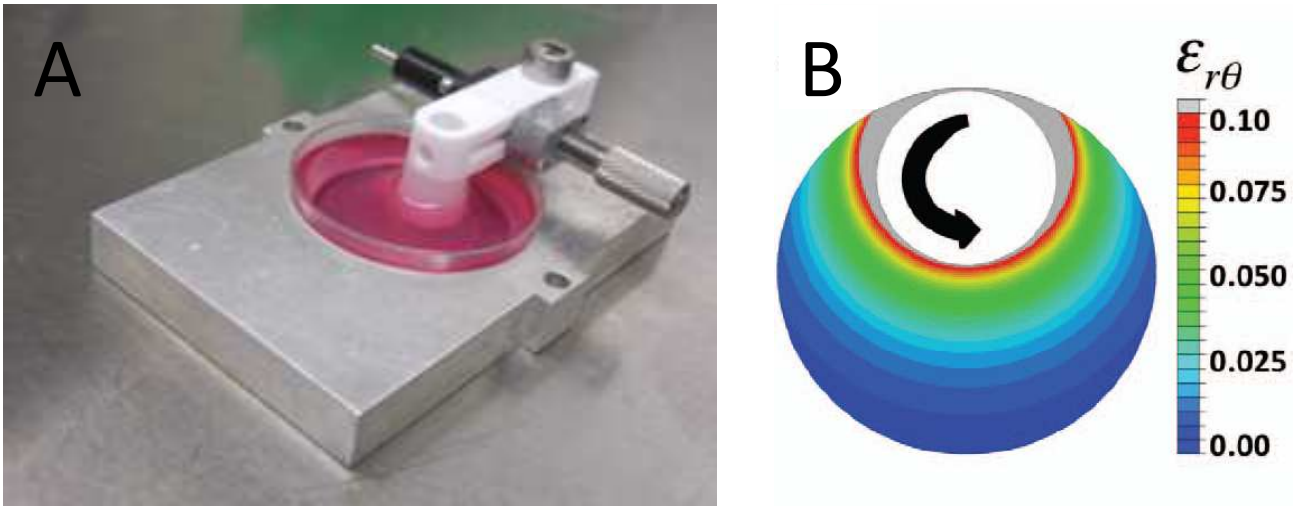

Figure 1.1: (A) The Botvinick Lab has developed a strain gradient device to take advantage of the nonlinear stress-strain relationship in biological materials in order to create a stiffness gradient and correlate cellular response to that gradient. AMR is used to map out the actual stiffness in the sample. (B) Finite Element Analysis (FEA) of shear strain, $\varepsilon_{r\theta}$, created in a 2.5 mg/ml fibrin gel in response to 2.4˚ rotation of the post (shown in white). (Kotlarchyk et al., 2011)

Capillary Growth Aligns With Direction of Strain In Mr. Twisty

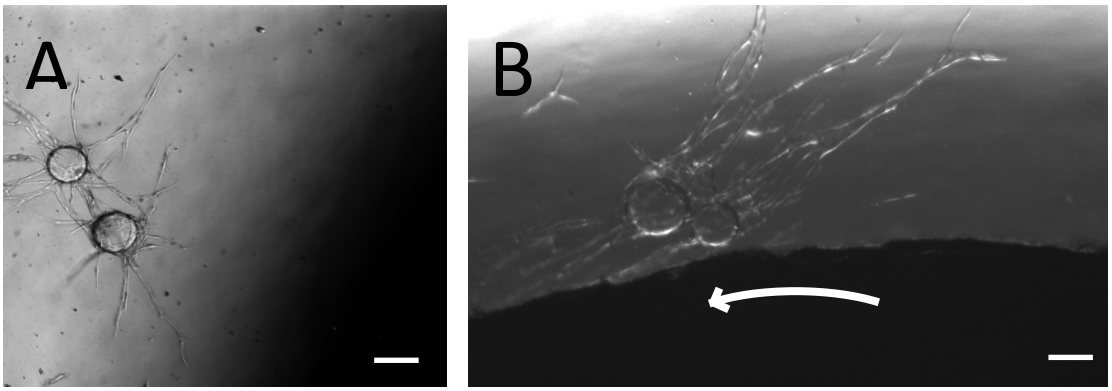

Figure 1.2: (A) Day 7 of culture without twist. Capillaries near the post experience no induced strain and grew normally. (B) Day 7 of capillary morphogenesis assay in Mr. Twisty near post (Twisted 6˚ on Day 2). Capillaries grew preferentially along the direction of strain (white arrow). Scale Bars are 200 μm.

Chapter 2

Direct, On-Chip Imaging of Capillaries Grown in 3D Culture

I came across an opportunity to collaborate with a group from University of California Los Angeles who was working on moving the laboratory microscope into the field. Dr. Aydogan Ozcan's research group had shown that cells grown in monolayers (2D cultures) could be imaged without the use of a lens by collecting a holographic (shadow) image of the cells and applying an algorithm to digitally reconstruct the holographic image into the true image of the cells (Seo, Su, Tseng, Erlinger, & Ozcan, 2009). This allowed them to construct a compact unit capable of imaging cells, such as blood smears, attached to a smart phone for field use. Dr. Ozcan and his students Serhan Isikman and Alon Greenbaum wondered if they could image 3 dimensional structures using a similar technique. The capillaries I had been growing for mechanical studies seemed the perfect 3D culture to test lens-free imaging on, and so, a collaboration was born.

Dr. Isikman and I attempted a few different methods of imaging the capillaries grown in 3D with their holographic imaging setup, but when the algorithm was applied to the raw images the reconstruction fell short of supplying sufficient resolution to make out the fine details of capillaries (though the raw holograms already conveyed the basic shape and location of the capillaries). Alon Greenbaum joined our effort when Dr. Isikman realized that the multi-height phase recovery (MHPR) algorithm that Alon was working on might be perfect for our application. He was right, and when the MHPR algorithm was applied to the holographic images the capillaries showed up with as much detail as images of the same capillaries under a scientific grade laboratory microscope equipped with a 10x objective

lens. The description of our findings was published in The Journal of Biomedical Optics, Dec 2012, as follows (Weidling, Isikman, Greenbaum, Ozcan, & Botvinick, 2012):

2.1

Lens-free computational imaging of capillary morphogenesis within three-dimensional substrates

John Weidling,[a] Serhan O. Isikman,[b] Alon Greenbaum,[b] Aydogan Ozcan,[b,c,d] and Elliot Botvinick[a,e,f]

[a]University of California Irvine, Biomedical Engineering Department, Irvine, California

[b]University of California Los Angeles, Electrical Engineering Department, Los Angeles, California

[c]University of California Los Angeles, Bioengineering Department, Los Angeles, California

[d]University of California Los Angeles, California NanoSystems Institute, Los Angeles, California

[e]University of California Irvine, Beckman Laser Institute, Irvine, California

[f]University of California Irvine, Edwards Lifesciences Center for Advanced Cardiovascular Technology, Irvine, California

Address all correspondence to: Elliot Botvinick, University of California, Irvine, California. Tel: 949-824-9613; Fax: 949-824-9968

Abstract.

Endothelial cells cultured in three-dimensional (3-D) extracellular matrices spontaneously form microvessels in response to soluble and matrix-bound factors. Such cultures are common for the study of angiogenesis and may find widespread use in drug discovery. Vascular networks are imaged over weeks to measure the distribution of vessel morphogenic parameters. Measurements require micron-scale spatial resolution, which for light microscopy comes at the cost of limited field-of-view (FOV) and shallow depth-of-focus (DOF). Small FOVs and DOFs necessitate lateral and axial mechanical scanning, thus limiting imaging throughput. We present a lens-free holographic on-chip microscopy technique to rapidly image microvessels within a Petri dish over a large volume without any mechanical scanning. This on-chip method uses partially coherent illumination and a CMOS sensor to record in-line holographic images of the sample. For digital reconstruction of the measured holograms, we implement a multiheight phase recovery method to obtain phase images of capillary morphogenesis over a large FOV (24mm^2) with $\sim 1.5\mu\text{m}$ spatial resolution. On average, measured capillary length in our method was within approximately 2% of lengths measured using a $10\times$ microscope objective. These results suggest lens-free on-chip imaging is a useful toolset for high-throughput monitoring and quantitative analysis of microvascular 3-D networks.

Keywords: three-dimensional culture, capillary morphogenesis, tissue engineering, angiogenesis, lens-free imaging, on-chip microscopy, computational microscopy, holographic microscopy

1. Introduction

Conventional light microscopy has been a vital tool in the life sciences by giving noninvasive visual access to micro-objects such as cells and microorganisms. Although significant improvements have been achieved to improve spatial resolution and contrast,[1-12] one important restriction of light microscopy for many applications has been the limited field-of-view (FOV) and depth-of-focus (DOF). That is, for applications where large areas and/or volumes need to be screened, one typically needs to mechanically scan the sample under the microscope, demanding long scan times and relatively complex hardware. Lens-free on-chip holographic microscopy offers an alternative platform that overcomes this limitation.[13–25] Unlike conventional light microscopy, lens-free on-chip microscopy does not rely on optical magnification. Instead, it uses the emerging large-format sensor architectures with small pixel sizes together with novel imaging algorithms to compensate for the lack of optical components such as lenses or objectives. Therefore, it enables imaging large areas (e.g., >24 to 30mm^2) at submicrometer spatial resolution in a compact and cost-effective set-up.[18,19,21–25]

In addition to the limited FOV, the short DOF associated with objective lenses poses further challenges, especially if the sample has a three-dimensional (3-D) structure, such as a tissue culture in a Petri dish where objects might be distributed at different depths. For such 3-D samples, in addition to lateral scanning, re-focusing by depth-scanning also becomes necessary. While high-end microscopes can perform both lateral and depth scanning automatically, these systems are cost-prohibitive and bulky. In contrast, lens-free on-chip holographic imaging provides particular advantages by offering the ability to perform post exposure digital auto-focusing (or depth-scanning) using holographic reconstruction over a depth-of-field of up to ~4 to 5 mm.[21,22] Owing to the partially coherent holographic image acquisition scheme (unlike e.g., contact imaging techniques) the detector records the information regarding the entire 3-D structure of the sample, and lens-free images can be digitally reconstructed at any depth of interest over an extended depth-of-field.[21,22]

One important biological system that can be observed at the scale and resolution of lens-free imaging is a cultured microvascular capillary network. The study of capillary network formation, or capillary morphogenesis and angiogenesis, is vital to the fields of wound healing and tissue engineering of prevascularized implants,[26] tumor mediated vascularization,[27] and various diseases.[28] Often times the growth and morphology of a complex capillary network must be monitored and quantified over many days in order to determine the effects of experimental conditions such as the addition of a putative drug.[29] Capillary tubule formation is commonly quantified by the average tubule length, number of tubules, tubule area, and number of branch points.[30] Since such measurements require micron-scale resolution, samples are traditionally imaged by conventional light

microscopy, which due to its small FOV and shallow DOF precludes rapid quantification of the entire culture volume. As a compromise, results are averaged across a discrete number of regions using a time-intensive process.[31-37] Numerous image analysis algorithms including packages for NIH ImageJ, Analyze Skeleton and AngioQuant[38,39] have been developed for accurate hands-free quantification of capillary growth,[31,33,40] leaving image acquisition as the primary rate-limiting step. While commercial high content imaging systems (e.g., BD Pathway 855) can scan the entire sample in 3-D, these systems are relatively expensive and slow because they rely on mechanical scanning.

In contrast to existing approaches, our lens-free on-chip technique enables imaging of the entire sample with sufficient resolution to draw statistical conclusions regarding changing morphology using existing image processing techniques. To demonstrate its proof of concept, here we present the use of lens-free on-chip microscopy to image capillaries grown in a 3-D *in vitro* system, without the use of lenses or mechanical scanning, and with sufficient spatial resolution to accurately determine vessel number, vessel length and vessel area.

2. Materials and Methods

2.1. Capillary Morphogenesis Model

A model for capillary morphogenesis as first described by Nehls and Drenckhahn was implemented in Ref. [41]. Primary human umbilical vein endothelial cells (HUVECs) were grown on microcarrier beads imbedded in a crosslinked fibrin hydrogel and given pro-angiogenic signaling factors naturally released by fibroblast cells cultured on top of the gel. HUVECs were first expanded in cell culture flasks to passage number three and then cultured on the surface of 150 to 210 μm diameter carrier beads (Cytodex). Beads were immersed in a 2.5mg/ml solution of fibrinogen (bovine, Sigma) in EBM-2 media (Lonza) at approximately 100 beads/ml solution. The solution was then pipetted into a 35 mm diameter Petri dish with type 1 glass bottom (MatTek) containing 20 μl of thrombin (Sigma). A clotting cascade forms a fibrin gel thus imbedding the carrier beads within a 3-D extracellular matrix. Once the gel is formed, normal human lung fibroblast cells (NHLFs) grown out to passage five were seeded onto a Transwell container (Corning) that is placed on top of the gel allowing signaling factors released by the fibroblasts to diffuse down into the gel while keeping the fibroblasts mechanically separated from the gel (Fig. 1). Next, 2 ml of EGM-2 media (Lonza) was added to each sample with media exchanged every other day. Capillary sprouting from the carrier beads begins by day two with large interconnected capillary networks forming by day seven. Imaging was performed on day seven.

2.2. Lens-free On-Chip Imaging Setup

The lens-free on-chip imaging setup, shown in Fig. 1, is composed of a partially coherent light source and an opto-electronic sensor array (complementary metal-oxide-semiconductor (CMOS) Model #MT9P031, Micron Technology; pixel size: 2.2 μm, 5 mega pixels). The sample is placed directly on the top of the sensor chip such that the distance, $z2$, between the objects and the active area of the detector is ~ 1 to 2 mm. The sample is illuminated using a near infrared light emitting diode (LED, λ=950nm) that is butt-coupled to a multimode optical fiber that has a core-diameter of 100 μm. The distance, $z1$, between the light source and the sample is typically $\sim$10cm, and its placement does not require sensitive alignment.
An infrared LED was selected in our imaging experiments since it was found to reduce the background noise from multiple scattering within the fibrin gel, and this also minimizes the phase-wrapping problems in the reconstructed lens-free phase images as phase delay is inversely proportional to the wavelength. Since the light impinging on the sample is partially coherent both temporally and spatially,[13,14] the unperturbed portion of the illumination interferes with the waves scattered by the objects. The sensor records this interference pattern, i.e., an in-line hologram of the objects placed on the chip. Owing to its unique geometrical configuration where $z1 \gg z2$, in-line holograms are recorded with unit magnification over a large imaging FOV that equals the active area of the sensor-array, in this case 24mm^2 (Fig. 2), which can further increase to e.g., >15cm^2 with a different choice of sensor-array.[16]

2.3. Digital Holographic Reconstruction

Lens-free images are reconstructed using digital beam propagation techniques based on the angular spectrum approach.[42] In this approach, lens-free images are convolved with the impulse response of free space propagation. This operation is done in the Fourier domain, by multiplying the 2D Fourier transform of lens-free images with the transfer function of free space propagation, which can be expressed as:[42]

$$H_c(f_x, f_y) = \begin{cases} e^{j2\pi\frac{z}{\lambda}\left[1-(\lambda f_x)^2-(\lambda f_y)^2\right]^{1/2}} & \sqrt{f_x^2+f_y^2} \le \dfrac{1}{\lambda}\,. \\ 0 & \text{otherwise} \end{cases} \quad (1)$$

In Eq. (1), f_x and f_y denote spatial frequencies of the input field along x and y, respectively, λ is the illumination wavelength in free space, and z is the distance to which the original

field is propagated. After multiplication by this transfer function, an inverse Fourier transform provides the output at the desired plane.

When the above-mentioned digital beam-propagation is performed on the measured lens-free holograms, the reconstructed images exhibit artifacts due to the "twin-image" noise. Stated differently, since imaging sensors are only sensitive to the intensity of an optical field, the initial phase of the complex field at the hologram plane, which is unknown, is assumed to be zero before digital propagation, giving rise to artifacts in the reconstructed image. In order to obtain a refined reconstructed image that does not suffer from this twin-image noise, phase recovery algorithms should be used to retrieve the unknown phase at the hologram plane. One way of achieving this is to use a size-constrained iterative phase recovery algorithm,[14] where the object size is used as additional information (i.e., size-constraint) in the reconstruction process. The object size can generally be estimated from the initial reconstruction despite the contamination due to the twin-image noise, as the boundaries of the objects can still be determined. For lens-free imaging of capillaries, however, the complex morphology of the sample makes it challenging to estimate the capillary shape and size, hampering the use of size-constrained phase recovery algorithms. As a result, here we utilized an alternative phase-recovery algorithm, multi-height phase recovery (MHPR),[24,25,43] which does "not" require the knowledge of the object size or shape as additional information, but instead uses multiple intensity measurements.

2.4. Multi-Height Phase Recovery

In this iterative phase-retrieval technique, multiple in-line holograms (i.e., intensity measurements) are recorded for the same object, where each measurement is performed at a different $z2$ distance. For lens-free imaging of capillaries, two intensity measurements were sufficient to effectively retrieve the phase of the optical field at the hologram plane. The change in $z2$ distance is achieved by placing or replacing a coverslip with a thickness of, for example, $\sim 150\,\mu$m as a spacer between the sample and the sensor. This operation may also cause a slight translation and rotation of the sample with respect to the sensor array between two successive lens-free image acquisitions. Therefore, the two measured lens-free holograms are first registered to each other in order to compensate for any translational or rotational motion. The exact $z2$distances do not need to be known a priori, since an auto-focus algorithm[17] as described below is utilized to estimate this parameter. After image registration, the MHPR algorithm is invoked to retrieve the missing phase of the sample holograms. The algorithm works by propagating the measured fields back and forth between the two planes of measurement. At each iteration, the algorithm enforces the recorded (i.e., measured) amplitude at the corresponding height (i.e., $z2$), while keeping the updated phase for the next iteration. This way, the missing phase is retrieved

in ~10 iterations without modifying the measured amplitude values, resulting in a refined lens-free image where the twin-image noise is significantly suppressed.

2.5. Digital Autofocusing Algorithm

An important attribute of lens-free holography is that it enables imaging of samples over a long depth-of-field, as long as the holograms of objects at large distances above the sensor (e.g., 1 to 5 mm) have sufficient signal-to-noise ratio.[21,22] This ability is particularly useful for imaging capillary morphogenesis due to the inherent 3-D nature of the sample. Imaging an extended depth-of-field is achieved by reconstructing the holograms at different depths-of-interest, which is equivalent to focusing a conventional microscope objective lens at different depths. However, digitally selecting the object-to-detector distance ($z2$), which maximizes the contrast and the signal-to-noise ratio of the object, can be a tedious task when imaging objects over a large volume. Towards this end, we implemented an autofocus algorithm to automatically determine the best plane of focus for imaging different capillaries across the sample volume.[17]

This autofocus algorithm is based on the fact that the edges of the object should be the sharpest at the plane of best focus. To estimate the sharpness of the edges, first a Sobel operator is used to detect edges in the vertical and horizontal directions. Second, the edge images are combined by using the two-norm (i.e., the square root of the sum of the squares). Third, the variance of the resultant image is calculated, where a high variance indicates existence of sharp edges. Therefore our autofocus algorithm scans several $z2$ distances spaced by e.g., 1 μm distances in order to find the $z2$ distance with the maximum edge variance, i.e., the best focus. It should be noted that this auto-focus algorithm is invoked twice in order to estimate the $z2$ distances for both measurement planes. For a typical sample, the difference in the $z2$ distances of the two lens-free holograms does not exceed 50 μm. Consequently, once the $z2$ distance for one of the lens-free holograms is determined, the search space for the $z2$ distance of the second hologram is rather small, achieving fast convergence.

3. Results and Discussion

To obtain microscopic 3-D images of the sample, the recorded lens-free in-line holograms are digitally reconstructed[14] where the recorded amplitude is initially multiplied by a reference plane wave and the resulting optical field is back-propagated[42] to the sample/object plane. Due to the in-line holographic recording scheme, the reconstructed images exhibit twin image noise [e.g., Fig. 3(a2) and 3(b2)], which degrades the lens-free image quality by concealing an object's fine features and giving rise to artificial intensity modulations that may lead to a biological misinterpretation. The arrows in Fig. 3 point to exemplary regions where the twin image hampers accurate interpretation of the

reconstructed images, either by concealing the actual structure, or sometimes creating artifacts that misleadingly appear like capillaries.

To digitally eliminate this twin image noise, as detailed in Sec. 2, a MHPR algorithm is invoked to enable accurate interpretation of our lens-free reconstructed images. A visual comparison of Fig. 3(a3) and 3(b3) to 3(a2) and 3(b2), particularly in the regions indicated by the arrows, clearly demonstrates the significance of our MHPR approach to lens-free 3-D imaging of capillaries. Figure 3(a4) and 3(b4) further demonstrate this improvement by showing profiles along the white lines in 3(a2), 3(b2), 3(a3), and 3(b3). These plots illustrate that using multi-height phase retrieval the modulations due to capillaries get stronger, increasing the image contrast, while false modulations due to the twin-image artifacts are now significantly suppressed.
It should be noted that pixel super-resolution techniques that digitally increase the spatial resolution of lens-free on-chip imaging were not implemented here.[18,19,21–23] As a result, the lens-free imaging platform utilized here provides a modest spatial resolution of ~ 1.5 to 2.0 μm (still subpixel considering that the CMOS chip has a pixel size of 2.2 μm),[14] which was more than sufficient for the quantitative analysis of vessel length in our application. We compared the average capillary length of a 3-D sample measured by both the MHPR-based lens-free microscopy [Fig. 4(a)] and an inverted microscope with a $10\times$ objective lens (Nikon, $\mathrm{NA}=0.1$) under bright field illumination [Fig. 4(b)]. In these measurements, capillary length was estimated as the linear distance from the center of the bead to the tip of each capillary. Based on these measurements, vessel length differences between the two methods were found to be less than 2% indicating that lens-free imaging can faithfully replace traditional microscopy in our model system. Importantly, the lens-free system has the advantage of its extraordinarily large FOV and DOF. The microscopic image shown in Fig. 4(b) acquired with a $10\times$ objective lens has a FOV of $0.86\times 0.65\mathrm{mm}$ allowing only one carrier bead to be imaged at a time, while the full FOV of the lens-free image (see Fig. 5) is 24 mm^2(i.e., >35 fold larger than the FOV of the microscope objective) allowing all the carrier beads to be imaged simultaneously without the need for mechanical scanning. Note that this FOV of the lens-free imaging technique is only limited by the active area of the detector chip, and sample areas larger than e.g., $15\mathrm{cm}$ can also be imaged by using wide-field CCD sensor-arrays.[16,44]

In summary, we have demonstrated that imaging of capillary morphogenesis is possible without the use of any lenses or mechanical scanning over a large FOV in 3-D culture. The resolution, image contrast and signal-to-noise-ratio achieved in the reconstructed holographic images were sufficient to extract useful structural information such as vessel

length, diameter, area, number of vessels, vessel shape, vessel interactions and the volume fraction of tissue that had been vascularized. The large FOV, depth-of-field, cost-effectiveness, and ease-of-use of the lens-free on-chip imaging platform make it attractive to researchers studying capillary growth under the influence of, for example, chemical or mechanical cues. A high throughput system for measuring growth over large volumes in multiple samples may be possible with the use of lens-free imaging, thus enabling high content screening of 3-D tissue cultures.

Acknowledgments

We wish to acknowledge Dr. Ekaterina Kniazeva for assisting with the capillary culture, Dr. Samir Shreim for assisting with the optical setup and Prof. Christopher Hughes for the supply of HUVECs. E. Botvinick acknowledges the Laser Microbeam and Medical Program (LAMMP), an NIH/NIBIB Biomedical Technology Center (P41EB05890) and the NSF Physical and Engineering Sciences in Engineering program (CMMI-1233697). A. Ozcan also acknowledges the support of the Presidential Early Career Award for Scientists and Engineers (PECASE), ARO Young Investigator Award, NSF CAREER Award, the ONR Young Investigator Award 2009 and the NIH Director's New Innovator Award DP2OD006427 from the Office of The Director, NIH.

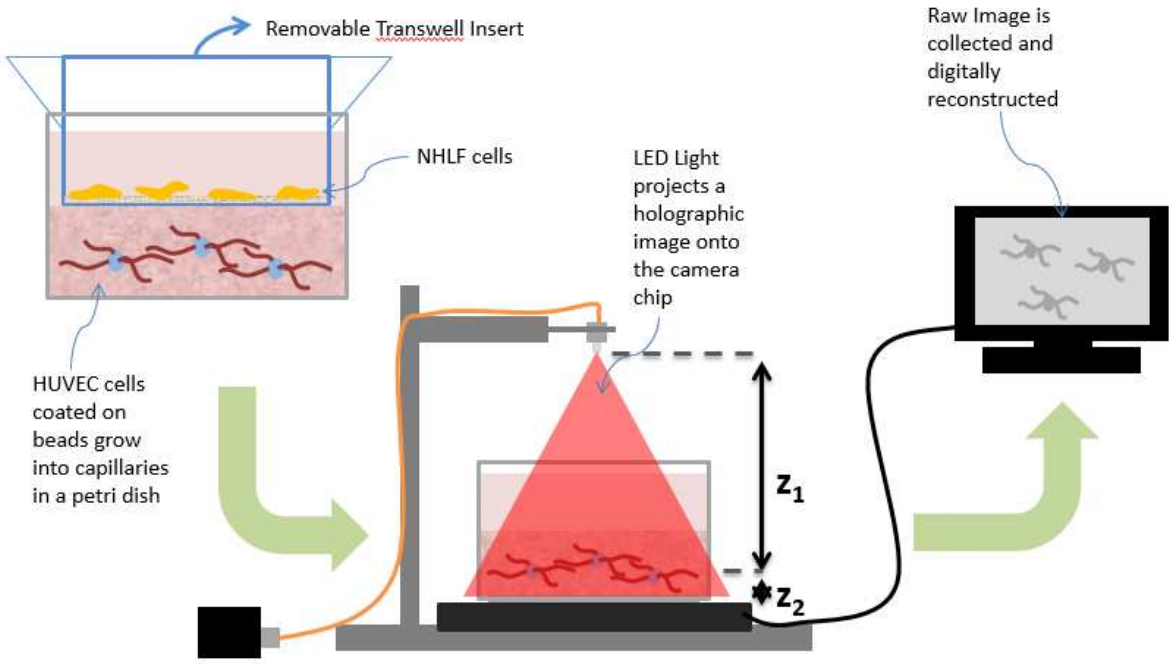

Figure 1: Schematic of our tissue culture system and lens-free computational imaging apparatus. NHLF fibroblasts are cultured on the top surface of a Transwell insert, which is placed within a 35 mm glass-bottom Petri dish. HUVECs were first cultured onto microcarrier beads, which were then embedded within a crosslinked fibrin hydrogel. Soluble signals released from the fibroblasts stimulate the HUVECs to spontaneously form capillaries. The insert was removed prior to imaging. A partially coherent fiber-coupled LED light source illuminates the Petri dish, which is placed above the CMOS chip to record the holographic image of the sample over a large field-of-view and extended depth-of-field; *z*1 is the distance between the light source and the object; *z*2 is the distance between the objects (capillaries) and the active area of the detector, which is changed by placing or removing a glass coverslip underneath the sample. A computer reconstructs lens-free images according to described algorithms.

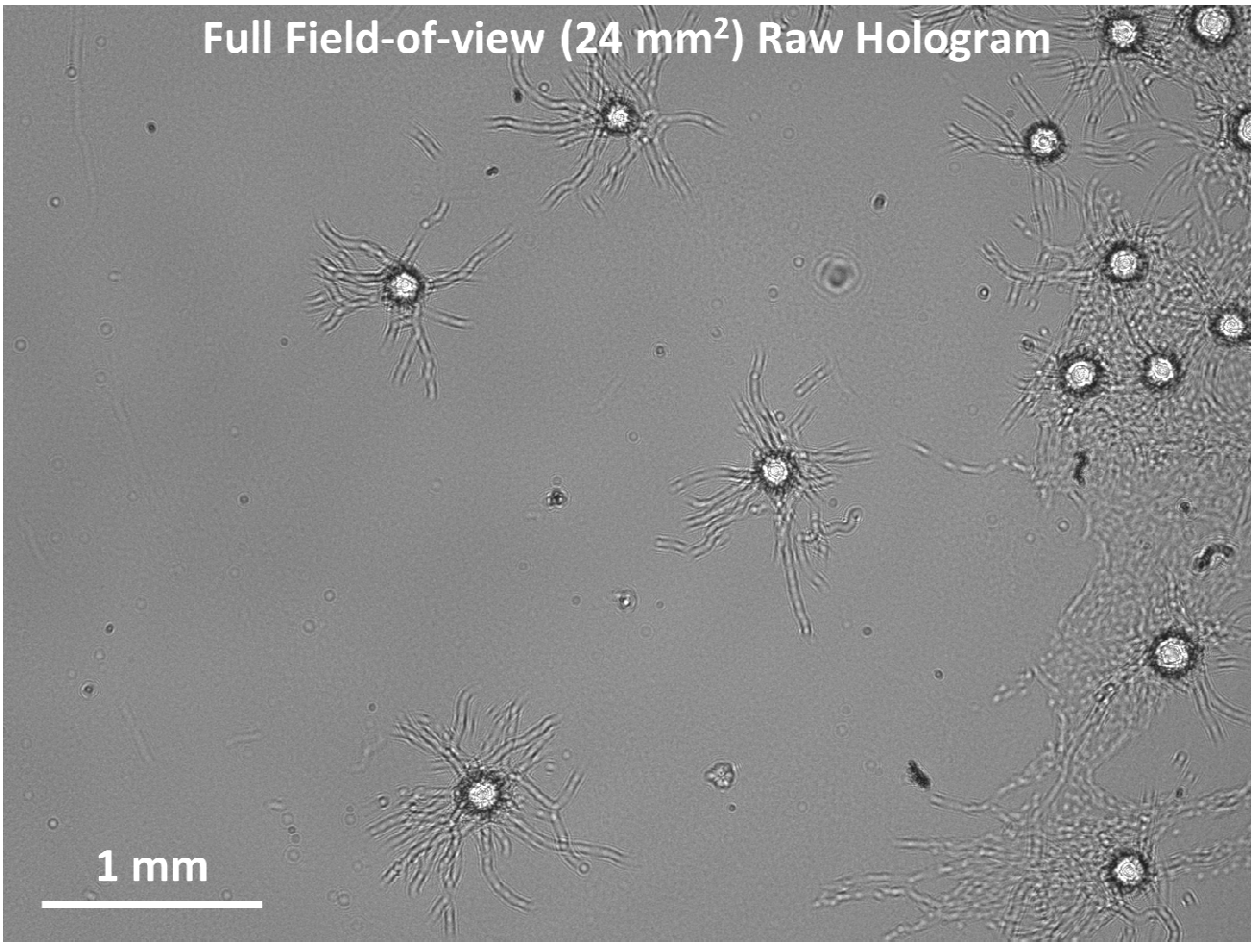

Figure 2: A full FOV hologram of a sample placed on the sensor array. The unit magnification holographic recording scheme permits imaging and monitoring capillaries over a large FOV of 24□□mm2, that equals the active area of the CMOS detector array.

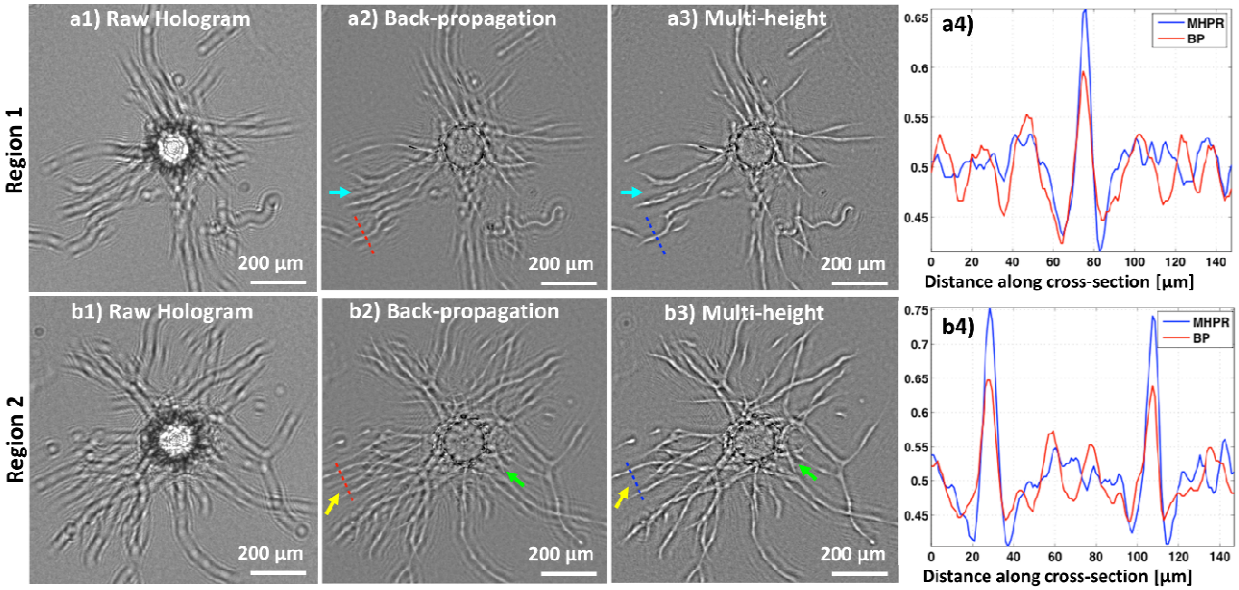

Figure 3: (a1, b1) Cropped raw holograms for region 1 and region 2 of Fig 2. (a2, b2) Reconstructed lens-free images after back-propagation (BP) without MHPR. (a3, b3) Reconstructed images using MHPR. This approach retrieves the phase of the hologram, and therefore effectively removes the twin image noise from the reconstructed images shown in (a2, b2). The arrows point to exemplary regions where removal of the twin-image noise is of particular importance, as it otherwise gives rise to artifacts that could be misinterpreted as capillaries. (a4, b4) Line profiles along the white lines in (a2, a3) and (b2, b3), respectively. These plots reveal that while the modulations due to capillaries get stronger in the line profiles with MHPR, false modulations due to the twin-image artifacts are significantly suppressed, further demonstrating the refinement and contrast enhancement in the lens-free images obtained by MHPR.

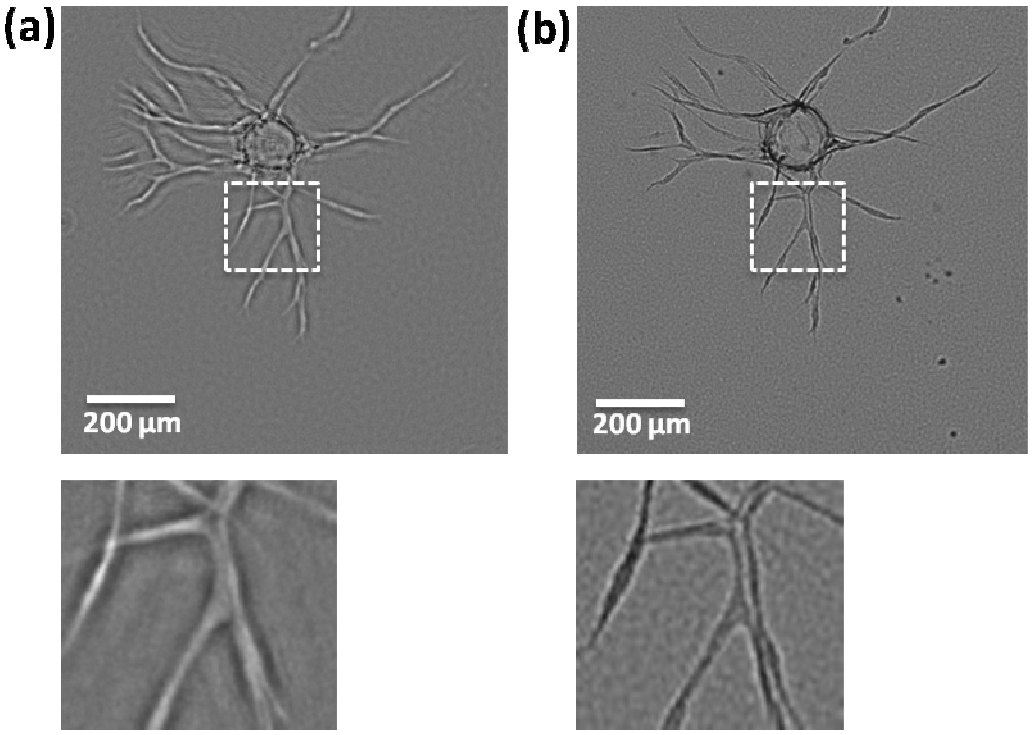

Figure 4: (a) Reconstructed image of a carrier bead and capillaries using MHPR. The zoomed region clearly shows sufficient resolution and contrast to delineate bifurcations highlighting micron-scale resolution. (b) The same carrier bead imaged with an inverted microscope and a 10× objective lens under bright field illumination. While the relative contrasts are reversed, key morphological features can be extracted from either the MHPR or the conventional microscope image.

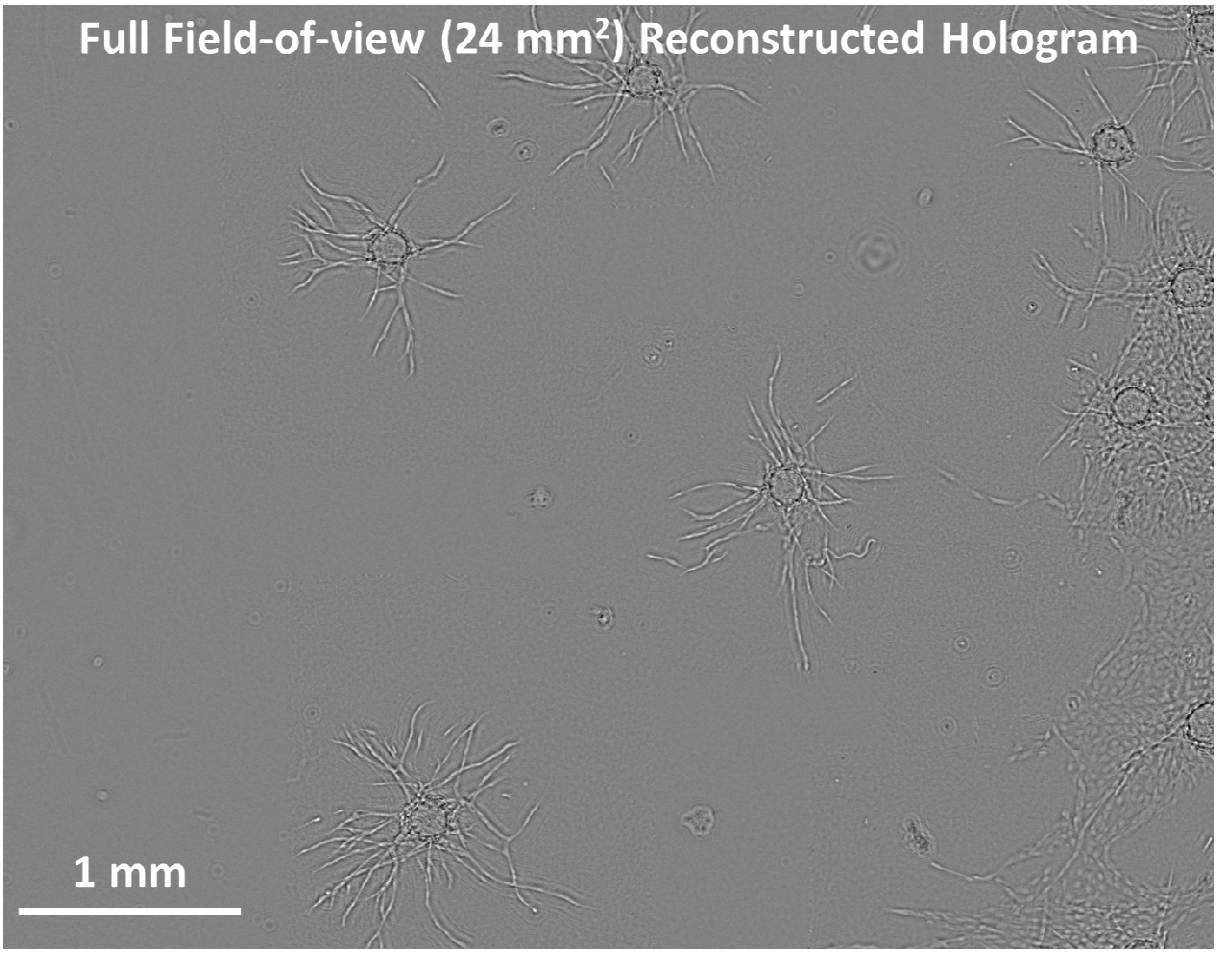

Figure 5: A full FOV lens-free image of the entire sample after applying the MHPR reconstruction algorithm to the raw hologram of Fig. 2.

References

1. Jones S. A., et al. , “Fast, three-dimensional super-resolution imaging of live cells,” Nat. Methods 8(6), 499–508 (2011).http://dx.doi.org/10.1038/nmeth.1605 [PMC free article] [PubMed]

2. Hell S. W., “Toward fluorescence nanoscopy,” Nat. Biotechnol. 21(11), 1347–1355 (2003).http://dx.doi.org/10.1038/nbt895 [PubMed]

3. Gustafsson M. G. L., “Nonlinear structured-illumination microscopy: wide-field fluorescence imaging with theoretically unlimited resolution,” Proc. Natl. Acad. Sci. U. S. A. 102(37), 13081–13086 (2005).http://dx.doi.org/10.1073/pnas.0406877102 [PMC free article] [PubMed]

4. Betzig E., et al. , “Imaging intracellular fluorescent proteins at nanometer resolution,” Science 313(5793), 1642–1645 (2006).http://dx.doi.org/10.1126/science.1127344 [PubMed]

5. Rust M. J., Bates M., Zhuang X., “Sub-diffraction-limit imaging by stochastic optical reconstruction microscopy (STORM),” Nat. Methods 3(10), 793–796 (2006).http://dx.doi.org/10.1038/nmeth929[PMC free article] [PubMed]

6. Hess S. T., Girirajan T. P., Mason M. D., “Ultra-high resolution imaging by fluorescence photoactivation localization microscopy,” Biophys. J. 91(11), 4258–4272 (2006).http://dx.doi.org/10.1529/biophysj.106.091116 [PMC free article] [PubMed]

7. Ma Z., et al. , “Fluorescence near-field microscopy of DNA at sub-10 nm resolution,” Phys. Rev. Lett.97(26), 260801 (2006).http://dx.doi.org/10.1103/PhysRevLett.97.260801 [PubMed]

8. Chung E., et al. , “Two-dimensional standing wave total internal reflection fluorescence microscopy: superresolution imaging of single molecular and biological specimens,” Biophys. J. 93(5), 1747–1757 (2007).http://dx.doi.org/10.1529/biophysj.106.097907 [PMC free article] [PubMed]

9. Zipfel W. R., Williams R. M., Webb W. W., “Nonlinear magic: multiphoton microscopy in the biosciences,” Nat. Biotechnol. 21(11), 1369–1377 (2003).http://dx.doi.org/10.1038/nbt899 [PubMed]

10. Choi W., et al. , “Tomographic phase microscopy,” Nat. Methods 4(9), 717–719 (2007).http://dx.doi.org/10.1038/nmeth1078 [PubMed]

11. Barretto R. P. J., Messerschmidt B., Schnitzer M. J., “*In vivo* fluorescence imaging with high-resolution microlenses,” Nat. Methods 6(7), 511–512 (2009).http://dx.doi.org/10.1038/nmeth.1339 [PMC free article][PubMed]

12. Rosen J., Brooker G., “Non-scanning motionless fluorescence three-dimensional holographic microscopy,” Nat. Photon. 2(3), 190–195 (2008).http://dx.doi.org/10.1038/nphoton.2007.300

13. Oh C., et al. , “On-chip differential interference contrast microscopy using lensless digital holography,”Opt. Express 18(5), 4717–4726 (2010).http://dx.doi.org/10.1364/OE.18.004717 [PMC free article][PubMed]

14. Mudanyali O., et al. , “Compact, light-weight and cost-effective microscope based on lensless incoherent holography for telemedicine applications,” Lab Chip 10(11), 1417–1428 (2010).http://dx.doi.org/10.1039/c000453g [PMC free article] [PubMed]

15. Tseng D., et al. , “Lensfree microscopy on a cell-phone,” Lab Chip 10(14), 1787–1792 (2010).http://dx.doi.org/10.1039/c003477k [PMC free article] [PubMed]

16. Seo S., et al. , “High-throughput lensfree blood analysis on a chip,” Anal. Chem. 82(11), 4621–4627 (2010).http://dx.doi.org/10.1021/ac1007915 [PMC free article] [PubMed]

17. Mudanyali O., et al. , “Detection of waterborne parasites using field-portable and cost-effective lensfree microscopy,” Lab Chip 10(18), 2419–2423 (2010).http://dx.doi.org/10.1039/c004829a [PMC free article][PubMed]
18. Bishara W., et al. , “Lensfree on-chip microscopy over a wide field-of-view using pixel super-resolution,” Opt. Express 18(11), 11181–11191 (2010).http://dx.doi.org/10.1364/OE.18.011181[PMC free article] [PubMed]
19. Bishara W., et al. , “Holographic pixel super-resolution in portable lensless on-chip microscopy using a fiber-optic array,” Lab Chip 11(7), 1276–1279 (2011).http://dx.doi.org/10.1039/c0lc00684j[PMC free article] [PubMed]
20. Su T., et al. , “A compact and light-weight automated semen analysis platform using lensfree on-chip microscopy,” Anal. Chem. 82(19), 8307–8312 (2010).http://dx.doi.org/10.1021/ac101845q[PMC free article] [PubMed]
21. Isikman S. O., et al. , “Field-portable lensfree tomographic microscope,” Lab Chip 11(13), 2222–2230 (2011).http://dx.doi.org/10.1039/c1lc20127a [PMC free article] [PubMed]
22. Isikman S. O., et al. , “Lensfree optical tomographic microscope with a large imaging volume on a chip,”Proc. Nat. Acad. Sci. U. S. A. 108(18), 7296–7301 (2011).http://dx.doi.org/10.1073/pnas.1015638108[PMC free article] [PubMed]
23. Isikman S. O., et al. , “Optofluidic tomography on a chip,” Appl. Phys. Lett. 98(16), 161109 (2011).http://dx.doi.org/10.1063/1.3548564 [PMC free article] [PubMed]
24. Greenbaum A., Ozcan A., “Maskless imaging of dense samples using pixel super-resolution based multi-height lensfree on-chip microscopy,” Opt. Express 20(3), 3129–3143 (2012).http://dx.doi.org/10.1364/OE.20.003129 [PMC free article] [PubMed]
25. Greenbaum A., Sikora U., Ozcan A., “Field-portable wide-field microscopy of dense samples using multi-height pixel super-resolution based lensfree imaging,” Lab Chip 12(7), 1242–1245 (2012).http://dx.doi.org/10.1039/c2lc21072j [PubMed]
26. Sahota P. S., et al. , “Approaches to improve angiogenesis in tissue-engineered skin,” Wound Repair Regen. 12(6), 635–642 (2004).http://dx.doi.org/10.1111/wrr.2004.12.issue-6 [PubMed]
27. Folkman J., “Tumor angiogenesis: therapeutic implications,” N. Engl. J. Med. 285(7), 1182–1186 (1971).http://dx.doi.org/10.1056/NEJM197108122850711 [PubMed]
28. Carmeliet P., “Angiogenesis in health and disease,” Nat. Med. 9(6), 653–660 (2003).http://dx.doi.org/10.1038/nm0603-653 [PubMed]
29. Evensen L., et al. , “A novel imaging-based high-throughput screening approach to anti-angiogenic drug discovery,” Cytom. Part A 77(1), 41–51 (2010).http://dx.doi.org/10.1002/cyto.a.20808 [PubMed]
30. Staton C. A., Reed M. W. R., Brown N. J., “A critical analysis of current *in vitro* and *in vivo*angiogenesis assays,” Int. J. Exp. Pathol. 90(3), 195–221 (2009).http://dx.doi.org/10.1111/j.1365-2613.2008.00633.x [PMC free article] [PubMed]
31. Kniazeva E., Putnam A. J., “Endothelial cell traction and ECM density influence both capillary morphogenesis and maintenance in 3D,” Am. J. Physiol. Cell Physiol. 297(1), 179–187 (2009).http://dx.doi.org/10.1152/ajpcell.00018.2009 [PubMed]
32. Korff T., Augustin H. G., “Tensional forces in fibrillar extracellular matrices control directional capillary sprouting,” J. Cell Sci. 112(19), 3249–3258 (1999). [PubMed]

33. Nakatsu M. N., et al. , “Angiogenic sprouting and capillary lumen formation modeled by human umbilical vein endothelial cells (HUVEC) in fibrin gels: the role of fibroblasts and angiopoietin-1,”Microvasc. Res. 66(2), 102–112 (2003).http://dx.doi.org/10.1016/S0026-2862(03)00045-1 [PubMed]
34. Nehls V., Drenckhahn D., “A novel, microcarrier-based *in vitro* assay for rapid and reliable quantification of three-dimensional cell migration and angiogenesis,” Microvasc. Res. 50(3), 311–322 (1995).http://dx.doi.org/10.1006/mvre.1995.1061 [PubMed]
35. Collen A., et al. , “Influence of fibrin structure on the formation and maintenance of capillary-like tubules by human microvascular endothelial cells,” Angiogenesis 2(2), 153–165 (1998).http://dx.doi.org/10.1023/A:1009240522808 [PubMed]
36. Koblizek T. I., et al. , “Angiopoietin-1 induces sprouting angiogenesis *in vitro*,” Curr. Biol. 8(9), 529–532 (1998).http://dx.doi.org/10.1016/S0960-9822(98)70205-2 [PubMed]
37. Wenger A., et al. , “Modulation of *in vitro* angiogenesis in a three-dimensional spheroidal coculture model for bone tissue engineering,” Tissue Eng. 10(9–10), 1536–1547 (2004).http://dx.doi.org/10.1089/ten.2004.10.1536 [PubMed]
38. Arganda-Carreras I., et al. , “3D reconstruction of histological sections: application to mammary gland tissue,” Microsc. Res. Techniq. 73(11), 1019–1029 (2010).http://dx.doi.org/10.1002/jemt.v73:11 [PubMed]
39. Niemisto A., et al. , “Robust quantification of *in vitro* angiogenesis through image analysis,” IEEE Trans. Med. Imaging 24(4), 549–553 (2005).http://dx.doi.org/10.1109/TMI.2004.837339 [PubMed]
40. Plendl J., et al. , “Primitive endothelial cell lines from the porcine embryonic yolk sac,” In Vitro Cell Dev. Biol. Animal 38(6), 334–342 (2002).http://dx.doi.org/10.1290/1071-2690(2002)038<0334:PECLFT>2.0.CO;2 [PubMed]
41. Nehls V., Drenckhahn D., “A microcarrier-based cocultivation system for the investigation of factors and cells involved in angiogenesis in three-dimensional fibrin matrices *in vitro*,” Histochem. Cell Biol. 104(6), 459–466 (1995). [PubMed]
42. Goodman J. W., Introduction to Fourier Optics, 3rd ed., Roberts & Company Publishers, Greenwood Village, Colo: (2005).
43. Allen L. J., Oxley M. P., “Phase retrieval from series of images obtained by defocus variation,” Opt. Commun. 199(1–4), 65–75 (2001).http://dx.doi.org/10.1016/S0030-4018(01)01556-5
44. Coskun A. F., et al. , “Lensfree fluorescent on-chip imaging of transgenic caenorhabditis elegans over an ultra-wide field-of-view,” PLoS One 6(1), e15955 (2011).http://dx.doi.org/10.1371/journal.pone.0015955[PMC free article] [PubMed]

Chapter 3

Development of a Transdermal Micro-Implantable Metabolite Sensor with Optical Communication

3.1 Metabolite Sensing Background

Change of Direction

After completing the capillary experiments at the end of my first year, Dr. Botvinick and I discussed a change of direction for my thesis work. I had experience in medical device design through my undergraduate studies and wanted to expand on that skill. Dr. Botvinick and I came up with a plan to pursue a continuous metabolite sensor that could be implanted shallowly under the skin surface and be measured by passing light through the skin. This would end up becoming the focus of my thesis, and led to the design and validation of a continuous implantable lactate sensor. The process I took to get from concept to prototype validation of that lactate sensor will be described in the following sections. The outline of this plan is as follows:

- Gain skills and knowledge of optical bio-sensing through an externship with a company
- Innovate a new means for continuous sensing of metabolites that will fill an unmet need in medical diagnosis and treatment
- Validate the use and accuracy of the new technology for bio-sensing *in vivo* in animal models

Externship in Optical Sensing of Metabolites

I first needed to obtain some background knowledge and skills related to bio-sensing, and specifically, bio-sensing through optical means. The perfect opportunity to gain these skills and knowledge came in the form of an externship with a local company (founded in part by Dr. Botvinick) that was working on developing an optical based bio-sensing technology. With this opportunity I would gain skills in biosensor principles of operation and calibration, optical interrogation of enzymatic reactions, signal processing and analysis of optical information, and manufacturing of micro-medical devices.

The Need for Continuous Metabolite Sensing

There are two metabolites of particular interest, where an unmet need for accurate continuous monitoring is apparent. The first of these metabolites is glucose, whose need for continuous monitoring is readily apparent in Type I diabetics. Continuous glucose monitors (CGMs) are already commercially available, but the current technology falls short of providing diabetics with glucose tracking that is accurate enough to base clinical decisions off of, which will be discussed later. The other metabolite of widespread interest is lactate, for its implications in the progression of injury and disease. There are currently no commercially available continuous lactate monitors, and I will present data that suggests that the need is great. This thesis will focus on continuous sensing of lactate, but will make comparisons to continuous glucose sensing in some cases because much more clinical data on continuous glucose sensing has been collected.

Glucose Sensing Significance:

Diabetes mellitus is a metabolic disorder that affects over 350 million people worldwide and the prevalence of diabetes in the world population is increasing at an alarming rate (Danaei et al., 2011). Keeping blood glucose levels under tight control represents the most effective way to either prevent the onset or reduce the progression of chronic complications in patients suffering from diabetes. Glycemic control impacts the two most prominent consequences of diabetes: health care costs and risk of severe micro- and macro vascular complications associated with the progression of the disease (ADA, 2008; Brown, Reynolds, & Bruemmer, 2010; Deshpande, Harris-Hayes, & Schootman, 2008; Hill & Fisher, 2010). Importantly, studies have demonstrated the attainment of tight glucose control can reduce the occurrence of deleterious long-term complications of diabetes (Control & Group, 1994; Trial, 2005). However, with increasing intensive insulin therapy, the risks of hypoglycemic episodes increases (CARE, 2003). Self-monitoring of blood glucose (SMBG) is a required component of recommended treatment regimens, required to prevent episodic hypoglycemia and crucial for the effective treatment and reduction of morbidity and mortality in type 1 diabetes (Blevins et al., 2010). However, studies show that patients do not follow recommended treatment guidelines when they require SMBG (Heinemann, 2008; Patton, Eder, Schwab, & Sisson, 2010). This failure to comply is not surprising given that current blood glucose tests (fingersticks) are painful, inconvenient, inaccurate and complicated by the formation of calluses on the fingers, which develop poor circulation. Fingerstick devices are widely insufficient for the management of diabetes because they do not provide a continuous measurement of glucose levels, and in fact are periodic at best (Blevins et al., 2010; Deshpande et al., 2008). In contrast, commercial continuous glucose

monitors (CGMs) hold promise to replace finger-stick devices, but currently are only intended to supplement SMBG and are not indicated for making treatment decisions due to their limited accuracy. These devices lack the reliability and accuracy to guide treatment decisions, particularly at low glucose concentrations, or hypoglycemia.

Lactate Sensing Significance:

10,000 foot view: Dr.'s Tim Jansen and Jan Bakker, leaders in the field of lactate guided therapy, state that *"A limitation of pre-hospital monitoring is that vital signs often do not change until a patient is in a critical stage. Blood lactate levels are suggested as a more sensitive parameter to evaluate a patient's condition."(Levy, 2003)*. A continuous lactate monitor (CLM) would be transformative in the treatment of critically ill patients. Such a device would enable goal-directed treatment based on real time lactate concentrations. Importantly, such treatment has already been shown to significantly improve outcomes in critically ill patients. However, lactate guided treatment is rarely practiced due to the logistical burden of taking serial measurements using point-of-care devices or as part of a lab panel.

Blood lactate levels change during life-threatening situations such as hemorrhagic shock and sepsis as well as in many other health conditions including pulmonary embolism(Vanni, 2013), cardiogenic shock(Vitek, 1971), aortic aneurism(Hashimoto, 2013), carotid artery disease(van Everdinge, 1998), heart failure(Gonzalez, 2013), sudden cardiac arrest(Adrie et al., 2002), acute respiratory distress syndrome(Mikkelsen et al., 2013), idiopathic pulmonary fibrosis(Kottmann et al., 2012) and respiratory failure(Manikis, Jankowski, Zhang, Kahn, & Vincent, 1995). During injury blood lactate

levels greater than 7-8 mM (healthy range: 0.5-2.2 mM) are associated with fatal outcomes(VINCENT et al., 1983). It has been shown that blood lactate levels have a role in diagnosis, risk-stratification, and goal-directed therapy both in the in the emergency department (ED)(Jansen, van Bommel, & Bakker, 2009) and the intensive care unit (ICU).(Bakker, Nijsten, & Jansen, 2013; Jansen et al., 2008; Jansen et al., 2010; Levy, 2003; Nguyen et al., 2004; Sciences, 2014; Shapiro et al., 2005; Smith et al., 2001; System, 2012). Rising lactate levels are strongly related to the Sequential Organ Failure Assessment (SOFA) score,(Bakker et al., 2013) while stabilized or decreasing blood lactate concentrations are predictive of patient survival(Cowan, Burns, Boyle, & Ledingham, 1984; VINCENT et al., 1983). This creates a need for a continuous lactate monitor, as decreasing or increasing lactate levels can only be determined with multiple samples over time, which are best acquired by a hands-free continuous monitor.

A closer look at two of the conditions where lactate measurement is important, provide a clear picture of the need for a CLM. These two patient populations account for 30 million hospital admission per year in the U.S.:

- **Sepsis:** There are over 750,000 patients affected each year resulting in 215,000 deaths annually in the United States(Angus et al., 2001). The number of sepsis cases is projected to rise to over one million by 2020 and the cost associated with treating these conditions is in excess of $16 billion each year(Angus et al., 2001). An aging population that is disproportionately affected by these conditions contributes to an incidence rate that is rising more rapidly than population growth.
- **Trauma:** Trauma is the leading cause of death in the US for people under the age of 45. It leads to 2.3 million hospital admissions and $406 billion of healthcare spending in the

US per year(Finkelstein, Corso, & Miller, 2006). Substantial clinical evidence supports the utility of using absolute lactate levels to triage trauma patients to appropriately direct resources among patients in the emergency department and improve outcomes(WO et al., 1993), (Andersen et al., 2013), (Aslar, Kuzu, Elhan, Tanik, & Hengirmen, 2004). Serial (i.e. continuous) lactate measurements have shown to provide further prognostic utility and improved outcomes(Manikis et al., 1995; Odom et al., 2013).

There is a comprehensive literature supporting the value of lactate in improving outcome and reducing mortality rates. The following is a representative snapshot.

Single Point Lactate Is Currently Used to Identify At-Risk Patients

- Serum Lactate is a risk-stratification biomarker for mortality(Shapiro et al., 2005). In a study of **1278** patients in the ED mortality rates increased with lactate. Patients with infection-related diagnosis and lactate levels of (0-2.5), (2.5-4) and (>4) 2.5mM had mortality rates of 5%, 9% and 38% respectively.
- Serum lactate can identify at-risk sepsis patients not presenting symptoms of shock(Mikkelsen et al., 2013). In a study of **830** patients (569 not in shock) with severe sepsis, elevated lactate was associated with mortality independent of clinically apparent organ dysfunction or refractory hypotension (shock).

Serial Lactate Measurements Track Improving or Worsening Medical Condition

- Serial lactate measurements can alert for impending organ failure and death(Manikis et al., 1995). In a study of **129** trauma patients initial and maximum lactate and duration of hyperlactatemia, calculated from serial lactate measurements, were reliable indicators of organ failure, morbidly and mortality ($p < 0.01$).

- Lactate clearance rate is a positive indicator of survivability(Nguyen et al., 2004). The rate of lactate clearance from the blood over the first 6 hours in hospital predicted mortality in an observational study of **111** patients with sepsis and septic shock (p = 0.007). Lactate clearance rate was inversely related to mortality (p = 0.04).

Serial Lactate Guides Improved Therapy

- Goal-directed therapy to reduce lactate reduces mortality in the ICU(Jansen et al., 2008). In a study of **348** patients with initial lactate ≥ 3.0 mEq/L, goal-oriented treatment targeting 10% decrease in lactate per hour increased patient survivability by 10% as compared to control (standard treatment, p = 0.067). Importantly, patients were discharged from the ICU earlier as compared to those in the control group.

These studies validate the utility of lactate as both a prognostic metric for inpatients as well as a real-time metric to be used by attending physicians to modify treatment for improved outcome. Serial measurements were shown to improve predictions and therapy. Our technology provides continuous and hand-free serial measurement of lactate not currently available in the emergency room (ER) or intensive care unit (ICU).

Continuous Metabolite Sensing State of the Art

Continuous Glucose Monitoring:

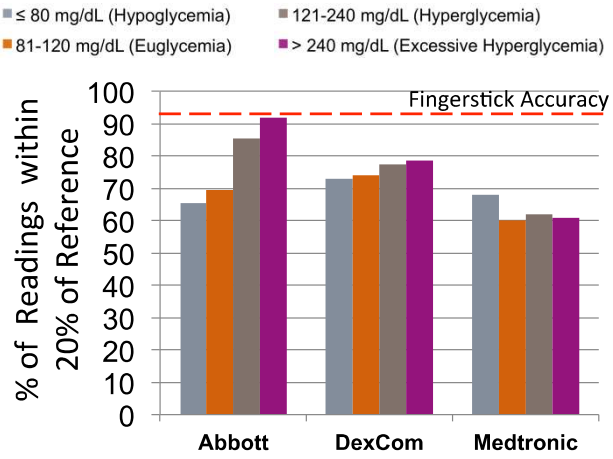

Figure 3.1. Current CGM Accuracy. Commercial continuous glucose monitors are unreliable, while patients long for live-saving technologies. Data is for best case with frequent finger stick calibration.

In the last few decades several subcutaneous (under the skin) continuous glucose monitors (CGMs) have become commercially available(Brauker, 2009; Hoeks, Greven, & de Valk, 2011; Oliver, Toumazou, Cass, & Johnston, 2009), however none of these CGMs are approved by the FDA for making clinical decisions such as insulin injection due to unreliable performance(Brauker, 2009) (Fig. 3.1). The best of them, sold by Abbott Laboratories was recently pulled from the market due to manufacturing inconsistencies. Improved accuracy is required for CGMs to close the loop with an insulin pump, and to fulfill the potential for tight diabetes management (Henry, 1998; Hirsch, 2009; Vadgama & Desai, 1991; Wang, 2008; Wilson & Gifford, 2005; Wilson et al., 1992). On average 70% of euglycemic (normal glucose) readings from commercial CGMs are within 20% of a reference (based on data in device user manuals, Fig. 1). Without exception, these CGMs exhibit unreliable and drifting responses over time due to *(i)* low and varying tissue [O_2], *(ii)* tissue interferents that affect the electrode, *(iii)* an inflammatory tissue response resulting in encapsulation and *(iv)* a fibrotic wound response (Peter Helding Kvist et al., 2006; Pickup, 2004; Pickup, Hussain, Evans, & Sachedina, 2005).

How Current CGMs Work:

A biosensor needs to have: high specificity for the analyte to be measured, good sensitivity across the clinical concentration range, accuracy and precision.

Enzymes Provide Specificity: Nature has provided a class of oxidase enzymes with incredible specificity to key metabolites such as glucose and lactate (lactic acid). Many of these analytes are found in the tissue and are indicators of real-time physiological and pathological conditions. Glucose Oxidase (GOX) catalyzes the oxidation of glucose into the metabolite gluconic acid (GA). It also produces hydrogen peroxide (H_2O_2), which can be measured electrochemically. One can easily relate bulk glucose to the electrical current of the H_2O_2 electrode in a well-mixed, oxygen-abundant container. Commercial CGM's use the signal produced by this redox reaction (transfer of electrons) at an electrode (usually made of Pt or Au). However, the commercial designs using peroxide detection are inaccurate.

Enzyme	Reaction
Glucose Oxidase (GOX):	glucose + O_2 $\rightarrow$ gluconic acid(GA) + H_2O_2

Sensor design determines sensitivity, accuracy, and precision:

Hydrogen Peroxide Based Sensors:

Medtronic and Dexcom CGMs both rely on GOX and electrochemical H_2O_2 detection as illustrated in Fig. 3.2. In these devices, a chamber is filled with a GOX-loaded hydrogel. The chamber has no-flux boundaries on three surfaces, one of which is an amperometric H_2O_2 electrode. The fourth surface is open to the tissue, allowing the flux of both glucose and

oxygen. In this mode of sensing, the electrode surface acts as a H_2O_2 sink, creating a zero H_2O_2 concentration at the electrode surface, where electrode current is proportional to the production rate of H_2O_2. The electrode current is calibrated as a measure of bulk glucose under the assumption that there is always excess O_2 compared to glucose. This assumption often fails in the tissue (Dixon, Lowry, & O'Neill, 2002; Wang, 2008), as illustrated in Fig 3.2A, where O_2 is sparse compared to glucose, and the GOX-mediated reaction becomes O_2-limited. As a result, the electrode current becomes more sensitive to changing O_2 than changing glucose, resulting in erroneous estimates of glucose. *In summary, the sensor of Fig 3.2A will have drifting calibration in euglycemia and hyperglycemia (blood glucose levels > 120 mg/ml) and poor signal strength in hypoglycemia.*

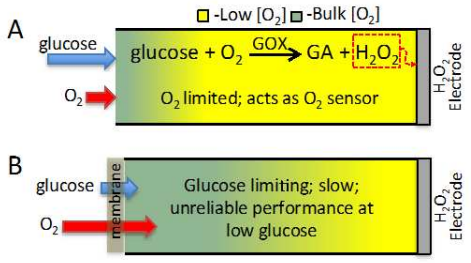

Figure 3.2. CGM Operating Scheme 1. Unreliable commercial glucose monitors utilize glucose oxidase (GOX) and **peroxide sensing**. (A) This design is oxygen limited and sensitive to changing oxygen. (B) A glucose limiting membrane ensures excess oxygen but is sluggish and unreliable.

The two commercial CGM technologies currently on the US market use a glucose-limiting membrane (Satish Garg & Lois Jovanovic, 2006; S. Garg & L. Jovanovic, 2006; Mastrototaro, Shin, Marcus, & Sulur, 2008; Weinstein et al., 2007)(Satish Garg & Lois Jovanovic, 2006; S. Garg & L. Jovanovic, 2006; Mastrototaro, Shin, Marcus, & Sulur, 2008; Weinstein et al., 2007) to ensure an excess of oxygen as compared to glucose within the chamber, as illustrated in Fig. 3.2B. *In this design the sensor has poor accuracy to low glucose, when diabetic patients most urgently need reliable measurements.* By severely limiting glucose permeability, the reaction rate, and thus electrode currents are very low during hypoglycemia, leading to a breakdown in electrode signal/noise, and device reliability. This results in the reported 70% or fewer of their measurements falling within 20% of the blood

reference. To make matters worse, the sensors do not account for tissue oxygen variability or availability and cannot alert the patient when the sensor is operating in an O_2-sensitive mode. In other words, the sensor cannot self-monitor to determine if its data is reliable. These electrochemical sensors are sensitive to electroactive species like urea and acetaminophen leading to glucose-independent measurement errors (P. H. Kvist & Jensen, 2007; Pasic, Koehler, Klimant, & Schaupp, 2007; Pasic, Koehler, Schaupp, Pieber, & Klimant, 2006). Lastly, a major source of error is inactivation of GOX by H_2O_2, which occurs continuously during implantation and can only be compensated for by serial fingerstick calibrations.

From this it is seen that commercial CGM's suffer from reduced specificity due to electrode interferents, and reduced sensitivity, accuracy and precision due to oxygen variability and availability, electrode drift (from H_2O_2 inactivation of GOX), and glucose limiting membranes.

Oxygen Based Sensors:

Another way to make measurements based on the enzyme redox reaction is to measure the amount of oxygen consumed rather than hydrogen peroxide. Oxygen-detecting sensors have improved sensitivity but require an evasive oxygen reference. In contrast to H_2O_2 sensors, O_2-based glucose sensors combine GOX with excess CAT to convert H_2O_2 to ½ O_2 under the next reaction. By making all surfaces O_2 permeable, such sensors can increase the flux of oxygen into the chamber as in Fig. 3.3A to possibly prevent O_2-limited reactions, and to bring O_2 levels into the sensitive range of the electrode. In fact, O_2 levels are highest during hypoglycemia, so that

Enzyme	Reaction
Glucose Oxidase (GOX):	glucose + O_2 → gluconic acid(GA) + H_2O_2
Catalase (CAT):	H_2O_2 → ½O_2 + H_2O

electrode signal/noise is greatest during dangerous episodes of low blood glucose. However, stable calibration absolutely requires an O_2 reference measurement. In other words, the reduction in O_2 can only be assessed if bulk O_2 levels are known. In Fig. 3.3A, the glucose sensor is implanted within a major blood vessel, and thus the oxygen flux is spatially uniform. In such a system, a reference O_2 electrode (not shown) enables stable calibration of blood glucose for over one year (Armour, Lucisano, McKean, & Gough, 1990). Unfortunately, this approach to glucose sensing fails in the subcutaneous tissue for two fundamental reasons. First, as is the case for H_2O_2 sensing, the GOX reaction can become O_2-limited and thus O_2 sensitive. Particularly since both the O_2 electrode and the GOX-reaction consume O_2. Therefore one must place a glucose-limiting membrane at the entrance of the chamber, as illustrated in Fig. 3.3B, which limits sensitivity to hypoglycemia. Second, tissue O_2 levels are spatially heterogeneous at the scale of the sensor, as illustrated in Fig. 3.3B. Consequently, there is no meaningful O_2 reference, and electrode currents cannot be reliably related to bulk glucose.

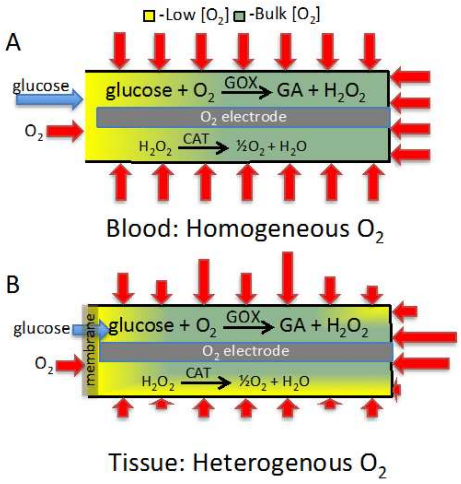

Figure 3.3. CGM Operating Scheme 2. Oxygen-based glucose monitors utilize GOX, CAT and electrochemical oxygen detection. A good schema for intravascular sensing (A) fails in the tissue (B).

Lactate Sensors:

Currently, there are no commercial Continuous Lactate Monitors available in the U.S., but there are fingerstick devices similar to blood glucose fingerstick monitors for measuring blood lactate levels. The challenges involved in making robust continuous lactate monitors are the same as those faced by current CGMs because they will both operate under the

same enzyme redox reaction principles. Also, it has been previously shown that an enzymatic glucose sensor can reliably be converted to a lactate sensor (Baker & Gough, 1995). The enzyme used will be Lactate Oxidase (LOX).

Enzyme	**Reaction**
Lactate oxidase (LOX):	lactate + $O_2 \rightarrow$ pyruvate + H_2O_2
Catalase (CAT):	$H_2O_2 \rightarrow ½O_2 + H_2O$

The current landscape of lactate monitoring devices consists of approved point of care (POC) 'finger stick' based lactate measurement devices and bench top analyzers. These include the Abbott i-Stat, Roche Accutrend Lactate and Lactate Pro. Maquet is developing an IV catheter-based continuous lactate monitor and has a prototype called the EIRUS. The EIRUS product profile is an invasive microdialysis catheter placed into a major vessel (i.e. central venous catheter). Dialysate is then pumped into an external sensing unit where lactate concentration is measured. No IV catheter based lactate sensor is currently being marketed. Additionally, catheter-based lactate monitors are targeted for use in the surgical market and would be impractical for use in the larger critical care and sepsis markets, which are opened up by a smaller, less invasive technology. There have also been attempts to make a non-invasive CLM, including a 'sticker' to measure lactate in sweat(Jia et al., 2013). The sweat lactate measuring device is not far out of its concept phase and has not been shown to track blood lactate across the clinical range. It is unlikely that a device measuring lactate in sweat will ever work in a situation where blood lactate level is needed

because lactate in the sweat is known to be uncorrelated to the blood (Green, Bishop, Muir, McLester Jr, & Heath, 2000).

Lactate is typically measured infrequently in a lab panel or POC device run approximately every few hours, as evidenced by the literature (Manikis et al., 1995; Nguyen et al., 2004; Smith et al., 2001). There is no commercial continuous monitor. The state of the art for assessing blood lactate is the gold standard benchtop *YSI Lifesciences 2300 STAT Plus* analyzer, and hand-held, single measurement, point of care devices such as the iSTAT (Abbot Labs). These devices are similar to those used by diabetics to test blood glucose levels and can only measure one time point as directed by the patient or treating staff.

Continuous measurement of lactate provides a number of advantages compared to current discrete measurement techniques. The availability to track trends in lactate levels improves risk stratification in the early hours after admission to the hospital and is a reliable metric for the real-time adjustment of therapies based on a patient's physiological response. This 'live' stream of information facilitates incorporation of the data into central patient monitoring systems.

3.2 Innovation of a New CLM

After reviewing the literature and the state of the art in technology for continuous sensing of metabolites a few conclusions were clear:

1. There is an immediate need for continuous lactate monitoring in EDs and ICUs that is not being met.

2. Commercially available electrode sensors for monitoring glucose are not accurate enough to use for making treatment decisions, and the electrodes are partially to blame.
3. The technology to produce a completely non-invasive CLM that tracks blood lactate *in vivo* is not available at present, but a *minimally invasive* device capable of accurate continuous lactate measurement could fill the unmet need using a combination of proven technologies and advancements in sensor design.

I started to think of ways to design an accurate, minimally invasive CLM. Materials and methods for building the sensors and measuring lactate with them were chosen based on either proven concepts reported in peer-reviewed scientific literature, or my own experiments designed to validate each engineering design decision.

During my externship I was exposed to a technology for measuring oxygen concentration that used an oxygen sensitive dye that could be measured with light excitation and phosphorescent emission detection. I learned how to make oxygen measurements using a dye that was one of a class of metallo-porphyrins, which are known for providing stable, reliable measurements of oxygen concentration with high quantum yield. I would end up testing many different metallo-porphyrin dyes to determine the best dye to measure light through tissue (skin). I started to determine the practicality of measuring dye through skin using the dye I had previously used during my externship, platinum (II) meso-tetra(pentafluorophenyl) porphine (PtTFPP, Frontier Scientific, Logan, Utah). PtTFPP or similar compounds are commonly used in commercial optical oxygen probes (e.g. Presens OXY-4, Ocean Optics Neofox).

Optical Oxygen Measurement:

The fluorescence and phosphorescence of certain luminophores can be quenched by substances such as oxygen by the mechanisms of FRET, Dexter Electron Transfer, or Exciplex. This means that in the presence of oxygen these luminophores will have a decreased intensity and lifetime decay of their excited emission. During my externship I used an oxygen sensitive metallo-porphyrin dye containing Platinum(II) as the central atom (PtTFPP). This dye can be excited by green light (or blue light) and its emission of red light can be detected by measuring the emission intensity or lifetime decay. In the presence of high oxygen concentration (~20%, room air) the phosphorescence of the Pt-Porphyrin dye is quenched and the measured lifetime is low (~25µs), but when oxygen is removed (0%, Nitrogen) the emission signal intensity increases and the lifetime decay increases as well (~100µs) (Fig. 3.4A). The phosphorescent lifetime decay of the Pt-Porphyrin dye increases monotonically with decreasing oxygen concentration and the inverse of lifetime normalized to 1 by the measured lifetime at 0% O_2 is plotted following the Stern Volmer Relationship (Eq. 1) in Fig. 3.4B, creating a calibration curve.

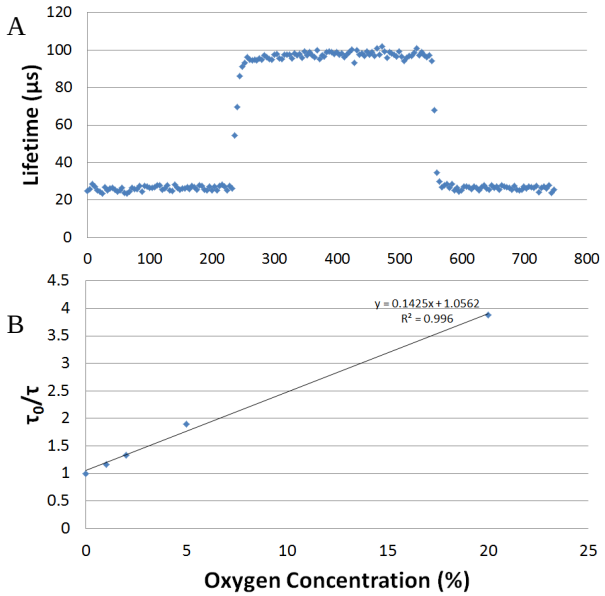

Fig. 3.4 Optical Oxygen Measurement and Calibration. A) Lifetime decay measurements of the Pt-Porphyrin dye. At time 0 the dye is in room air (~20% O_2), after about 4 minutes pure Nitrogen is blown in over the dye (0% O_2), after another 4 minutes the Nitrogen is purged by blowing room air back over the dye. B) Stern Volmer plot of dye emission lifetimes (τ) for oxygen concentrations between 0 and 20%.

$$\frac{\tau_0}{\tau} = K_{SV}[O_2] + 1 \qquad \text{Eq. 1}$$

Where τ_0 is the zero oxygen lifetime, τ is the measured lifetime decay, K_{SV} is the Stern Volmer constant, and $[O_2]$ is the concentration of oxygen.

Measurement of PtTFPP Emission Through Tissue:

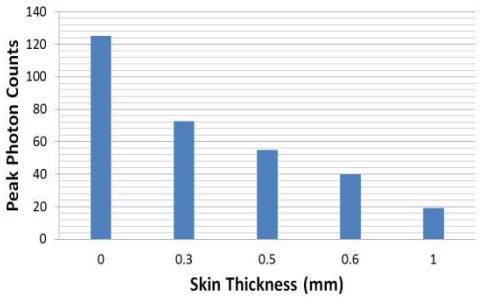

Fig. 3.5 Return Signal Through Tissue. Peak photon count from fluorescent emission of PtTFPP dye excited through fixed pig tissue (belly skin) of varying thickness.

The PtTFPP dye was interrogated through dissected pig skin of varying thickness to determine peak photon count return from phosphorescent emission (Fig. 3.5). Pork belly skin was obtained from a local supermarket, fixed in a formalin solution, and dissected into sections of varying thickness from 0.3 to 1 mm thick. PtTFPP dye dissolved along with Polystyrene in chloroform (2 mg PtTFPP, 30 mg polystyrene, in 450 µl chloroform) was dotted onto a glass slide with an area of approximately 154 mm^2 leaving a dried matrix of PtTFPP imbedded in a thin layer of polystyrene. The skin sections were placed over the dye and a multi-fiber probe with one 50 µm emission fiber and four 100 µm detection fibers was placed above the skin, aimed at the dye spot. Pulsed green laser excitation light was sent through the tissue onto the dye exciting a red fluorescent photon emission. The peak returning photon count from the averaged pulses was recorded for each section of tissue over the same dye spot. With no tissue present the system returns about 125 peak photon counts and as tissue thickness increases the return photons captured decreases due to absorption and scattering of the light in the tissue. Lifetime fitting can still be achieved at a thickness of 1 mm although the noise level is higher. The results indicated that measurement of oxygen levels through thin tissue may be possible with PtTFPP dye covering an area of ~150 mm^2 and a fiber launched

laser/detection system. However, measurements through tissue of thickness greater than 1mm would require a different setup and the size of the dye spot would ideally be much smaller to enable minimally invasive insertion of a sensor coated in dye into tissue.

Measurement of Oxygen concentration range through pig skin:

In a similar setup, a glass slide with dye spotted on top (~150 mm^2 in area) was placed

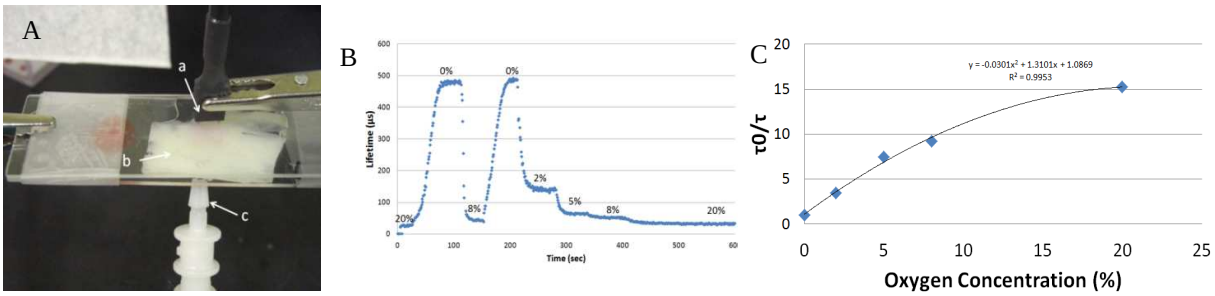

Fig. 3.6 Oxygen Calibration Through Pig Skin. A) Setup: A multi-fiber probe (a) excites the dye beneath the skin (b) with green laser light, the fluorescent emission from the dye is collected and the lifetime decay is calculated. In order to calibrate the dye for oxygen concentrations between 0 and 20% mixed oxygen gasses are flowed over the dye from a pressurized nozzle (c) and the lifetime for each concentration is calculated. B) Continuous lifetime decay readings from the dye as gasses of varying oxygen concentration are flowed over it. C) A Stern-Volmer plot for calibrating the dye to known oxygen levels.

under fixed pig skin of 0.53 mm thickness and calibrated gasses with varying oxygen concentrations from 0 to 20% were blown over the dye spot (Fig. 3.6A). Lifetime measurements were made in the same way as before and plotted over time in Fig. 3.6B. The average measured lifetime at steady state for each concentration was calculated and plotted in a Stern Volmer calibration curve with a second order polynomial fit (Fig. 3.6C). The fitted equation to the data plotted in this way becomes a calibration curve for determining any oxygen concentration within that range given a measured lifetime decay.

The oxygen measurements through tissue proved to us that it was feasible to perform measurements *in vivo* using metallo-porphyrin dye. Using my current setup however, would require making large sensors that could be coated with a large volume of dye to get

signal through tissue. I would later find a metallo-porphyrin dye that produced much higher return signal through tissue, enabling smaller sensors and a less complex measurement apparatus.

New Dye for Improved Transmission Through Tissue

PtTFPP has been a widely used dye for oxygen sensing, but it doesn't meet all of the desired requirements for measuring oxygen through tissue. The main drawback of PtTFPP is that it must be excited with blue or green light which is more highly absorbed and scattered in tissue than red or near infrared (NIR) light for instance. I searched for other dyes that could be used to measure oxygen that would have the following characteristics: strong absorption band in the red or NIR wavelengths, emission band in the red or NIR wavelengths, high quantum yield (Q.Y.), lifetime decay in the tens or hundreds of microseconds. One dye meets all these requirements, and even has higher Q.Y. than PtTFPP. That dye is Platinum Tetraphenyl Tetrabenzoporphyrin (PtTPTBP, Frontier Scientific). It is excitable with red light as it contains a high absorption band with a peak of 615nm, its Q.Y. is about 50%, and its zero oxygen lifetime decay is approximately 47 microseconds putting it within the range of our detection system.

A New Excitation and Detection System for Measuring Oxygen

When I switched to the use of red-excitable PtTPTBP dye the signal through tissue was so much higher than my previous setup using PtTFPP that I thought I may be able to use a less sensitive detector than the photon counting APD unit I previously used in my fiber-coupled system. I wanted to make a measurement system that was less complex than the fiber

system I had previously used. I thought that LEDs would be a simpler excitation source to control and found through some initial testing that LEDs placed near the tissue above an implanted sensor provided better excitation through tissue than fiber coupled LEDs, so I designed an apparatus that would place LEDs close to the tissue surface and aim the center of their emitted light at a sensor implanted 1-2 mm deep in tissue (fig. 3.7A). I also found that more of the emitted light from the sensor could be collected using a large area photodetector close to the tissue surface than could be from a smaller area fiber collecting light on the skin surface. These observations led me to abandon fiber optics altogether and combine the bare LED excitation source and the large area photodiode into one piece that could be placed on the skin surface in alignment above an implanted sensor (fig. 3.7B).

A

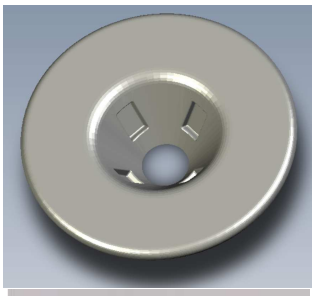

B

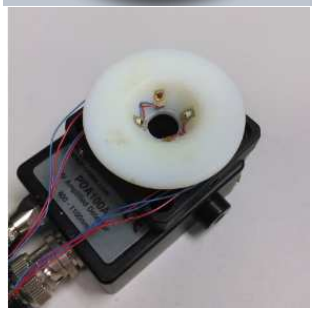

Fig. 3.7 Probe Design. A. A 3D model of a fixture designed to hold LEDs at an angle for aiming their emission through tissue. B. The LED holding fixture is attached to a commercial amplified large area photodetector to complete our measurement probe.

New software was also written for analysis of the return dye signals as measured by our probe (written in part by a biomedical engineering undergraduate in our lab, Princeton Saroha). Armed with a higher output dye, a simpler data analysis software, and a newly designed probe I performed *in vivo* testing. To complete this testing of the system and accomplish a research aim of our lab I used the new system to measure the oxygen level within implanted alginate beads in rat subcutaneous tissue.

Our lab collaborates with the lab of Dr. Jonathan Lakey in a project to immunoprotect pancreatic islet cells for transplantation. Often the transplantation of islet cells fails over time due to death of the transplanted cells. One mechanism thought to contribute to this cell death is hypoxia due to an immunoprotective barrier that also limits oxygen diffusion. A popular way to provide this barrier is by encapsulating islets in small alginate beads. Though other research groups have proposed that hypoxia is killing islets in these encapsulations, no one had previously measured the oxygen level *within* the beads, where the cells reside. We figured out a way to break up our oxygen-sensitive dye into particles small enough to be dispersed throughout 400 micron diameter alginate beads. We could then implant the beads in the subcutaneous space and measure the oxygen level inside the beads from outside the body with our measurement probe. The results of these experiments were published in the Journal of Biomedical Optics, July 2014, and is reprinted with permission as follows (Weidling, Sameni, Lakey, & Botvinick, 2014):

3.3

Method Measuring Oxygen Tension and Transport Within Subcutaneous Devices

John Weidling ; Sara Sameni ; Jonathan R. T. Lakey ; Elliot Botvinick
J. Biomed. Opt. 19(8), 087006 (Aug 27, 2014). doi:10.1117/1.JBO.19.8.087006
History: Received June 3, 2014; Revised July 27, 2014; Accepted July 28, 2014

Abstract

Cellular therapies hold promise to replace the implantation of whole organs in the treatment of disease. For most cell types, *in vivo* viability depends on oxygen delivery to avoid the toxic effects of hypoxia. A promising approach is the *in situ* vascularization of implantable devices which can mediate hypoxia and improve both the lifetime and utility of implanted cells and tissues. Although mathematical models and bulk measurements of oxygenation in surrounding tissue have been used to estimate oxygenation within devices, such estimates are insufficient in determining if supplied oxygen is sufficient for the entire thickness of the implanted cells and tissues. We have developed a technique in which oxygen-sensitive microparticles (OSMs) are incorporated into the volume of subcutaneously implantable devices. Oxygen partial pressure within these devices can be measured directly *in vivo* by an optical probe placed on the skin surface. As validation, OSMs have been incorporated into alginate beads, commonly used as immunoisolation devices to encapsulate pancreatic islet cells. Alginate beads were implanted into the subcutaneous space of Sprague–Dawley rats. Oxygen transport through beads was characterized from dynamic OSM signals in response to changes in inhaled oxygen. Changes in oxygen dynamics over days demonstrate the utility of our technology.

Introduction

Nonautologous tissue transplantation is a promising approach to overcome the scarcity of human pancreas donor tissue in the treatment of type 1 diabetes.[1–5] To this end, we have developed a scalable islet of Langerhans (islet) isolation method wherein partially digested piglet pancreatic tissue is matured *in vitro* over 8 days by incubation in a novel cell culture media.[6,7] During this period, exocrine tissue dies and isolated islets remain, which we have shown to be responsive to glucose challenges. Isolated islets can be encapsulated within permeable hydrogels such as alginate to provide an immunoprotective barrier that may preclude pharmacological immunosuppression.[8,9] However, encapsulation devices introduce a transport barrier between the host and graft tissues and inherently limit oxygen supply, compromising graft function and cell viability,[10] problems that scale with device wall thickness.[11,12]

Typically grafts are implanted in subcutaneous[13] or intraperitoneal[14] sites where partial pressures of oxygen (pO_2) are approximately 60 and 40 mm Hg, respectively, which is lower than that of arterial blood (>80 mm Hg). It is commonly asserted that low cell viability within devices[15,16] results from low tissue oxygen taken together with device diffusional barriers to create hypoxic and anoxic conditions, where these conditions are known to promote cell death through necrosis and apoptosis.[17] However, direct measurement of oxygen levels within microencapsulated devices *in vivo* has not been previously reported, where such measurements are ultimately required to assay the efficacy of implant technologies that claim to promote oxygen delivery. In a study of relatively large alginate disc implants (1 to 1.5 cm^2 surface area at 3- to 6-mm thick) by Veriter et al.,[18] oxygen within implanted devices was directly measured through the use of electronic paramagnetic resonance oximetry in rats. However, current research shows that such thick devices cannot retain islet function, likely due to diffusional limitations, thus promoting microencapsulation technologies such as thin sheets or microbeads of permeable materials. We have developed a technology for the direct measurement of oxygen partial pressures within such implanted devices. Our technology comprises oxygen-sensitive microparticles (OSMs) and an electro-optical probe to noninvasively excite OSMs and record emitted light from which pO_2 is determined. Additionally, we have developed a protocol to measure both the steady state pO_2 within devices as well as transport dynamics between the device and the local vasculature. This is especially important for pancreatic islets transplantation because islets are metabolically demanding and are sensitive to decreases in tissue oxygenation. Although native islets contain an extensive capillary network,[19]implanted devices typically do not, and are limited in their ability to supply oxygen to encapsulated

pancreatic islets.[10] Consequently, these islets are subject to hypoxic or anoxic conditions,[15,16] contributing to the death of 40% of pancreatic islets in implants after just 4 weeks.[20] Strategies aimed at improving oxygenation within biomaterial-encapsulated islets should significantly improve the chances of a successful transplant.[21]These strategies can be tested with our technology to rule out approaches that do not mitigate a period of hypoxia post transplantation.

Method for Preparing Alginate Beads Containing Oxygen Sensing Microparticles

Preparation of OSMs

OSMs are made from an oxygen-sensitive dye embedded within a polystyrene matrix. Two types of OSMs were fabricated, each comprising a unique oxygen-sensing metalloporphyrin dye. The first is platinum(II) meso-tetraphenyl tetrabenzoporphine (PtTPTBP, Frontier Scientific, Logan) and the second is platinum(II) meso-tetra(pentafluorophenyl)porphine (PtTFPP, Frontier Scientific, Logan). OSMs are fabricated by first mixing 2 mg of dye with 30 mg of polystyrene (M_w 2500, Sigma, St. Louis) and then dissolving the mixture in 450µl of chloroform (Sigma). The solution is pipetted and spread onto a glass slide to polymerize overnight in room air at 23℃. The resul ting thin film is scraped off with a razor blade and crushed into small micron-sized particles using a glass mortar and pestle.

Encapsulation of OSMs Within Alginate Beads

Clinical grade ultrapure low viscosity alginate (UPLVM, Novamatrix, Sandvika, Norway) is dissolved in deionized water at 3 wt. % and sterile filtered using a 0.22µm syringe filter. OSMs are suspended in 1.5 mL of the UPLVM solution and loaded into an encapsulator (Nisco, Zurich, Switzerland) for the fabrication of alginate beads. Specifically, the solution is first loaded into a syringe and then driven through a 25 G needle under positive gas pressure (4 PSI, N_2). The needle is held at 9 V relative to a 120 mM $CaCl_2$ solution within a Petri dish placed below the tip of the needle. Alginate beads form at the tip of the needle and fall into the $CaCl_2$ solution for alginate polymerization. A typical OSM alginate bead is shown in Fig. 1. Bead size is dependent on gas pressure, voltage, and the distance between the needle and media in the dish. For these experiments, the average diameter of alginate beads was found to be 415±47.68µm.

Probing pO2 Within Alginate Beads

Optical Probe for In Vitro Experiments

An optical probe was constructed to simultaneously measure both OSM types (Fig. 2). The two OSM types are spectrally separated. PtTFPP OSMs have multiple absorption peaks at 390, 504, and 538 nm and emission peaks at 647 and 710 nm.[22] PtTPTBP OSMs have multiple absorption peaks at 430 and 614 nm and an emission peak at 770 nm.[22] The

optical probe can selectively excite either type of OSM with two pairs of light emitting diode (LEDs) (Rebel LED, Luxeon Star, Brantford, Canada) centered at 530 nm (green) and 617 nm (red) for PtTFPP and PtTPTBP, respectively. The LEDs are mounted onto a custom three-dimensional printed conical mount designed to pitch the LEDs such that emitted light converges onto samples placed just above the surface of the cone. The conical mount is glued onto the distal surface of a 2-in. long lens tube (Thorlabs, Newton) containing a 6.4-mm diameter image conduit (Edmund Optics, Barrington) and a focusing lens ($f=25mm$). The distal end of the lens tube is mounted onto a filter cube holder (Thorlabs) containing a long-pass dichroic beam splitter (FF740-Di01, Semrock, Rochester) to reflect PtTFPP and transmit PtTPTBP emissions, respectively. Two amplified photodiode detectors (PDA100A, 9.8-mm diameter, $Gain=30$, Thorlabs) are mounted onto the cube to detect emissions from each OSM type. LED emission and digitalization of photodiode signals are conducted by a National Instruments data acquisition device (USB6361 DAQ, National Instruments, Austin) controlled by LabView (National Instruments).

Determining Oxygen Partial Pressure From OSM Emission

OSMs were calibrated from measurements acquired at different pO_2 levels, as provided by four gas tanks containing different oxygen mixtures. OSM emission was analyzed using the method of luminescence lifetime. OSMs were optically excited by pulsing LEDs in a 100 Hz square-wave with a 50% duty cycle. Optical signals were sampled at 1 MHz. OSMs were probed every 20 s, where at each time point, 25 measurements were acquired at 100 Hz and averaged. The metalloporphyrin dye within OSMs continues to emit light after the cessation of each LED light pulse. This emission is modeled as an exponential decay as

$$V(t)=V_0e^{(-t/Tau)},(1)$$

where V is the detector voltage, V_0 is the voltage at the start of the decay, t is the time, and Tau is the lifetime decay time constant. Dye emission is quenched by oxygen and consequently, Tau decreases with increasing pO_2. The relationship between pO_2 and Tau is described by a modified Stern–Volmer relationship[23]

$$Tau/Tau_0=f1+K_{SV}[O_2]+1-f,(2)$$

where Tau is the oxygen-dependent lifetime decay time constant, Tau_0 is the zero oxygen lifetime decay constant, f is the fraction of emission of one site of a two-site model,[24] and K_{SV} is the Stern Volmer constant. K_{SV} and f were estimated by optimization.

In Vitro Measurement of Oxygen Partial Pressure Within Alginate Beads

Alginate beads containing PtTPTBP OSMs and unencapsulated PtTFPP OSMs were suspended in 1 mL of media phosphate buffered saline (PBS) within a single well of a 24-well dish (Corning Inc., Corning) in which gas was bubbled (Fig. 3) with either compressed

air (21% oxygen), or precalibrated mixtures of 10% oxygen/90% nitrogen, 5% oxygen/95% nitrogen, or argon gas (0% oxygen).

Figure 4 plots pO_2 as reported by both the encapsulated and nonencapsulated OSMs versus time for a series of gas exchanges. The pO_2 levels were calculated by first computing the mean steady state lifetime values for each gas concentration using Eq. (1). Regression of lifetime against gas concentration as computed by Eq. (2) ($R^2>0.99$) provides a calibration equation mapping lifetime to pO_2. Data confirms oxygen sensitivity within the alginate bead and no significant dynamic delay between the PBS and the volume of the bead (Fig. 4).

Measuring pO2 and Transport Dynamics In Vivo

In Vivo Probe

A compact *in vivo* optical probe was constructed for PtTPTBP OSMs alone [Fig. 5(a)]. Since only one dye is being measured *in vivo* there is no need for the more complex optical setup used in the *in vitro* experiment. Two of the 617-nm centered LEDs were mounted on the conical mount, as described above. The conical mount was then placed directly on the photodiode module and aligned with the active area of the photodiode. A 715 nm high-pass optical filter (Semrock) is mounted above the surface of the photodiode. The conical mount is placed directly onto the skin during measurements.

In Vivo pO2

In vivo testing was performed to determine if PtTPTBP OSM signals can be related to pO_2within subcutaneously implanted alginate beads. A small incision was made on the anterior side of an anesthetized rat (Sprague–Dawley, Charles River Laboratories, Wilmington). Anesthesia was maintained with a gas mixture of 100% oxygen and vaporized isoflurane delivered to a nose cone placed over the snout. OSM-containing beads were then implanted subcutaneously via pipette injection in a small pocket formed in the subcutaneous space by blunt dissection. The incision was closed using a wound sealing adhesive (Gluture, Abbott, Abbott Park). pO_2 within beads was then optically probed on demand through the skin. Rats were fixed with a rodent pulse oximeter (Kent Scientific, Torrington) placed on the front paw to simultaneously measure oxygen saturation of blood hemoglobin (SpO_2) and heart rate.

Figure 5(b) shows pO_2 data acquired on day 5 post implantation during anesthesia. As expected, SpO_2 was constant at normal physiological levels (95% to 100%) and pO_2within the beads was $\sim 100 mm Hg$, indicating gas exchange both through the vasculature and skin.

The data collected *in vivo* was analyzed for its accuracy. Decay curves were collected as described above (measurements taken every 10 s with 25 curves for each measurement).

After averaging the 25 curves, the variance at each point was found to be <0.5% of the mean value [Eq. (1)]. In the absence of OSMs, the detector returns an exponential decay of Tau ~15μs. To determine the weight of this effect on OSM-mediated signals, the mean signal value between 0 and 50μs of OSM-mediated signals was divided by that for the OSM-free signals. The ratio was >7, which we found was insignificant for fitting OSM lifetimes.

Variable Inhaled Gas Experiment

We developed an assay to measure transport dynamics between the microbeads and local vasculature. Such an assay is important since it captures effects of both increase/decrease of local vasculature resulting from the implantation wound and subsequent healing as well as the deposition of new collagenous tissue, which forms an additional diffusional barrier. Inhaled gas is rapidly changed as pO_2 and SpO_2 are monitored. Oxygen dynamics after each gas change are governed by tissue architecture, with rise/fall times increasing or decreasing as the local tissue rejects or perfuses the implant, respectively.

For these tests, the 100% oxygen + isoflurane inhaled gas was transiently exchanged with room air (21% oxygen) + isoflurane and then returned to 100% oxygen + isoflurane. OSMs were probed every 10 s. Measurements were recorded on days 5 and 9 post implantation.

Figure 6(a) shows a typical variable inhaled gas experiment at day 5. pO_2 and SpO_2 exhibited dynamics in the early stages of anesthesia (first 30 min) and eventually reached a steady state when breathing the 100% gas mixture. This phenomenon was common to most of our experiments and is likely due to the physiological effects of isoflurane. The gas was changed to the room air mixture for ~10 min and then returned to the 100% O_2mixture for ~25 min. pO_2 within beads did not reach a steady state within the 10 min of room air, but did within the 25 min of 100% O_2. Similar results were observed for the second room air challenge beginning at ~72 min.

The variable inhaled gas experiment was repeated for the same rat on day 9 [Fig. 6(b)]. Here, pO_2 reaches a steady state within the ~10 min of room air gas indicating rapid O_2 exchange between the beads and tissues as compared to day 5, an effect most likely mediated by tissue remodeling.

Conclusions and Future Directions

One of the great challenges for creating a successful nonautologous cellular therapy is to provide the new cells in the body with sufficient oxygen and nutrient transfer to survive while protecting them from the immune system. An array of techniques for encapsulating islet cells in alginate has been studied and tested extensively, but ultimately fail within weeks due to, in part, hypoxic conditions. We have developed a technique for measuring the

oxygen concentration continuously inside an implanted object, such as an alginate bead, and verified its operation *in vivo* in rats by measuring its response to changing inhaled oxygen concentrations and comparing that response at two time points within the first week of implantation, during which wound healing is most active. The results showed that our technique tracks changes in oxygen in implanted alginate beads and that the rate of oxygen transfer to the implanted beads increased during the wound healing process. This link between wound healing and oxygen transport dynamics within the implanted microbeads could have implications for identifying designs that lead to either cell survival or cell death. By knowing the amount of oxygen inside the implants, one may be able to correlate that level with critical points in the wound healing process, such as new vessel formation or the identification of areas that have become “walled-off” from the body.

Optical oxygen sensing using luminescent dyes has gained popularity and is used in some commercial fiber-based optical oxygen probes, such as the Ocean Optics NeoFox system, and the PreSens oxygen probes (which can be used in biological applications). These devices show that the luminescence-based sensing of oxygen is reliable, but they fall short of being able to measure within implanted materials on small scales and would require a tethered component crossing the skin surface. Other technologies exist to noninvasively measure oxygen levels proximal to an implant, but these technologies do not measure oxygen within the device and thus cannot report on the microenvironment of encapsulated tissues. Such technologies include oxygen electrodes either implanted or in contact with skin,[25,26] or scattered light methods such as diffuse optical spectroscopy (SpO_2 measurement). Our technology has been demonstrated to continuously measure pO_2 within implanted alginate microbeads using inexpensive optical components coupled to a standard data acquisition device. Microbead pO_2 values measured subcutaneously in our study ($\sim$45 to 120 mm Hg) were higher than those reported by Veriter et al. ($\sim$5 to 40 mm Hg) where larger alginate devices were implanted in a similar manner. This difference can be attributed to differential tissue responses or the accuracy of the sensor. Our calibration against known gases had a regression coefficient of $R^2>0.99$ indicating the accuracy of our system, and we have found that alginate microbeads elicit a moderate tissue response as compared to a slab (unpublished data). Future studies are planned to encapsulate islets along with OSMs and correlate pO_2 with implant functionality and cell survival. This will provide quantitative evidence concerning the role of oxygen transport in reported failed approaches to islet encapsulation for reversal of type 1 diabetes. Additionally, our technique can evaluate new encapsulation technologies for their oxygen transport characteristics.

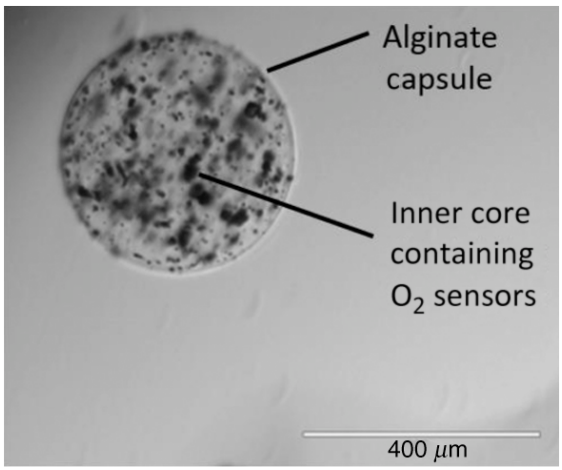

F1 :
An alginate capsule containing oxygen-sensitive microparticle (OSM) sensors.

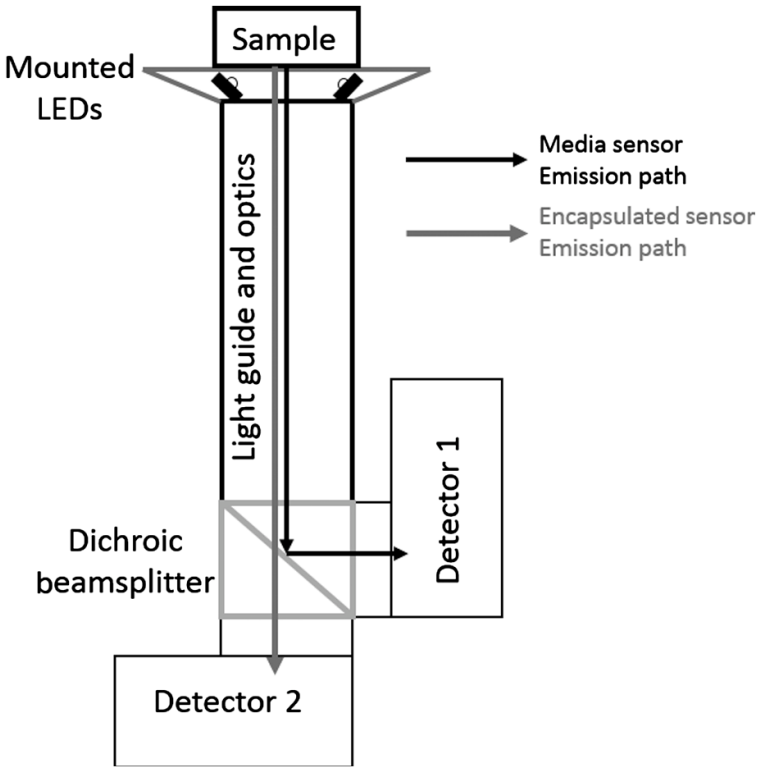

F2 :

Illustration of optical probe used for *in vitro* measurement. Emitted light from the two OSM types is separated spectrally onto two separate detectors.

(a) Mixed gas

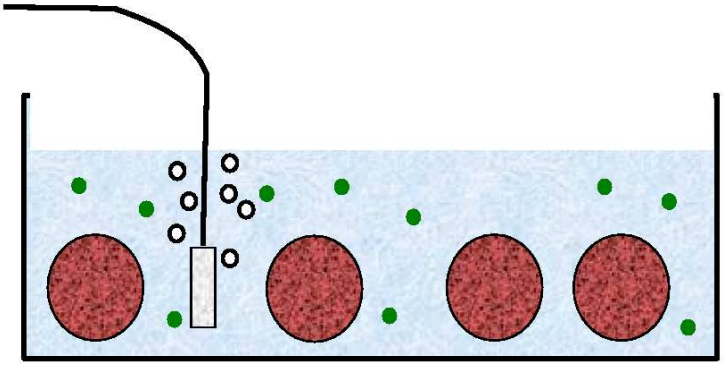

(b)

F3 :

(a) *In vitro* test system. Two spectrally distinct OSM types are suspended in a PBS bath within a well: one to monitor the PBS (green circles) and one to monitor the alginate capsules (red circles). (b) Close up view showing PBS and encapsulated OSMs within a well.

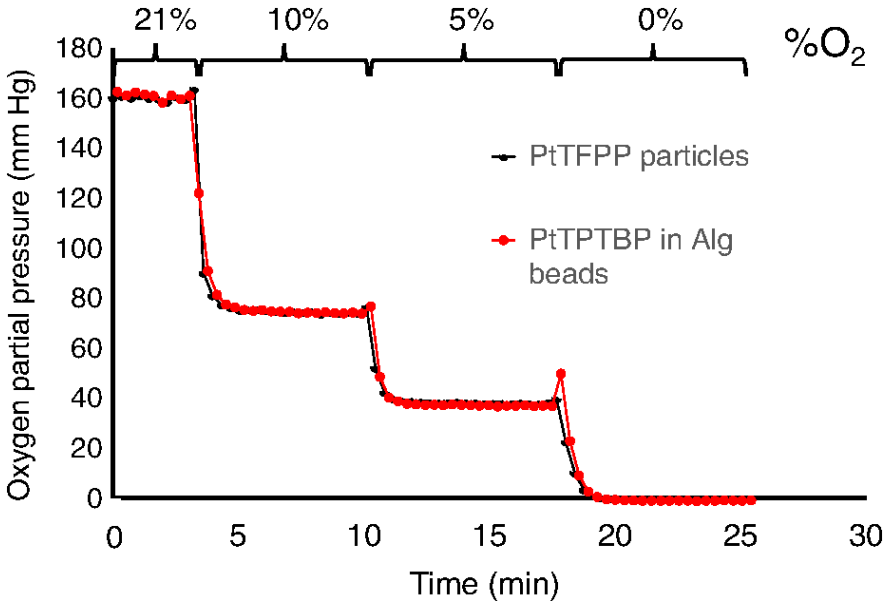

F4 :

In vitro measurements. pO_2 for a set of gases containing oxygen at 21%, 10%, 5%, and 0%. Black line: pO_2 in PBS and red line: pO_2 in alginate capsules.

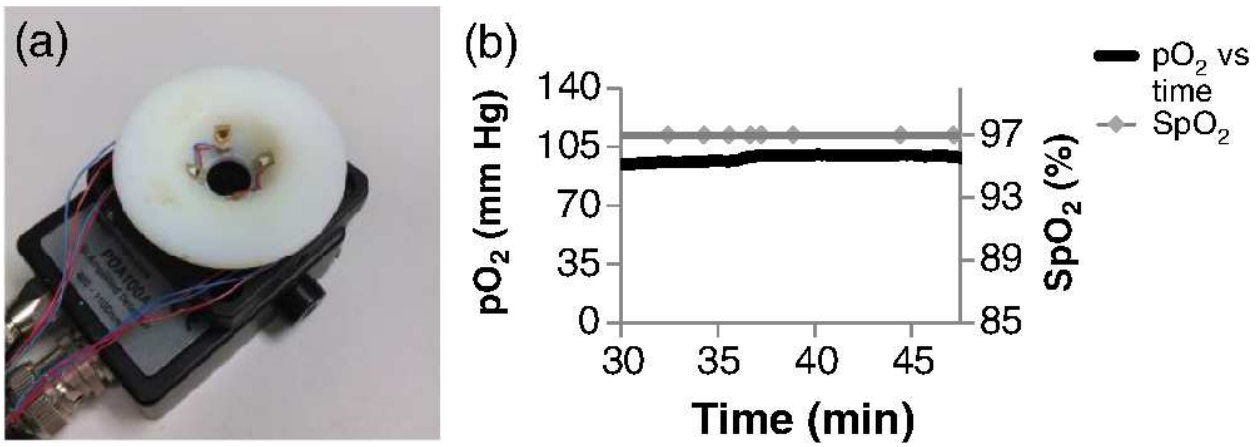

F5 :

In vivo measurements. (a) Optical probe used for *in vivo* measurements. (b) Day 5 $pO_2$and SpO_2. Animals were anesthetized during measurements with a mixture of isoflurane and 100% oxygen.

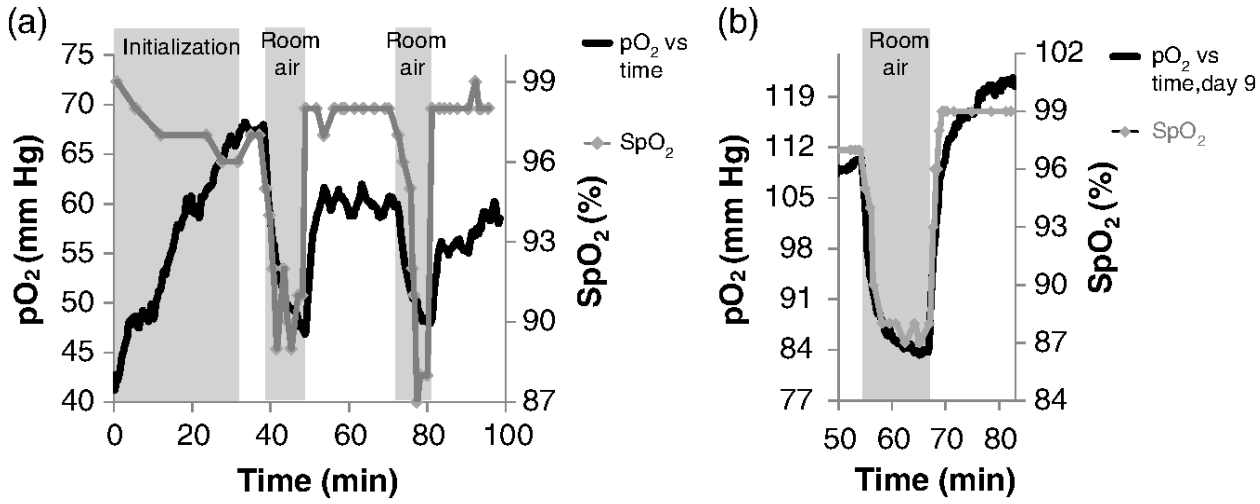

F6 :

(a) Variable inhaled gas experiment. On day 5, SpO_2 and pO_2 within capsules consistently exhibit dynamics after the initiation of anesthesia, stabilizing after approximately 30 min. At 37 min, the percent oxygen mixed with isoflurane was changed from 100% to 21% for 11 min and then switched back. The same exchange in inhaled gas is repeated 26 min later. (b) On day 9, pO_2 within capsules exhibits faster dynamics following a gas exchange as compared to day 5.

Acknowledgments

The authors would like to acknowledge Michael Alexander for providing training on animal procedures and providing technical support during animal procedures. E. Botvinick acknowledges the Air Force Office of Scientific Research (FA9550-10-1-0538) and the National Institutes of Health (P41EB015890). J. Lakey acknowledges financial and institutional support from Department of Surgery, University of California Irvine.

References

1

Ching C. D. et al., “A reliable method for isolation of viable porcine islets,” Arch. Surg.. 136, (3), 276 –279 (2001). 0004-0010 **CrossRef**

2

Thanos C. G., Elliot R. B., “Encapsulated porcine islet transplantation: an evolving therapy for the treatment of type I diabetes,” Expert Opin. Biol. Ther.. 9, (1), 29 –44 (2009). 1471-2598 **CrossRef**

3

Sutherland D. et al., “Isolation of human and porcine islets of Langerhans and islet transplantation in pigs,” J. Surg. Res.. 16, (2), 102 –111 (1974). 0022-4804 **CrossRef**

4

Larsen M., Rolin B., “Use of the Gottingen Minipig as a model of diabetes, with special focus on type 1 diabetes research,” ILAR J.. 45, (3), 903 –313 (2004).**CrossRef**

5

Korbutt G. S. et al., “Neonatal porcine islets as a possible source of tissue for humans and microencapsulation improves the metabolic response of islet graft post transplantation,” Ann. N. Y. Acad. Sci.. 831, (1), 294 –903 (1997). 0077-8923 **CrossRef**

6

Lamb M. et al., “In vitro maturation of viable islets from partially digested young pig pancreas,” Cell Transplant.. 23, (3), 263 –272 (2013). 0963-6897 **CrossRef**

7

Kuehn C. et al., “Young porcine endocrine pancreatic islets cultured in fibrin show improved resistance toward hydrogen peroxide,” Islets. 5, (5), 0 –7 (2013). 1938-2014 **CrossRef**

8

Darrabie M. D. et al., “Characteristics of poly-l-ornithine-coated alginate microcapsules,” Biomaterials. 26, (34), 6846 –6852 (2005). 0142-9612 **CrossRef**

9

de Vos P. et al., “Multi scale requirements for bioencapsulation in medicine and biotechnology,” Biomaterials. 30, (13), 2559 –2570 (2009). 0142-9612 **CrossRef**

10

Schrezenmeir J. et al., “Long-term function of porcine islets and single cells embedded in barium-alginate matrix,” Horm. Metab. Res.. 25, (4), 204 –209 (1993). 0018-5043 **CrossRef**

11

Chowdary K., Mohapatra K. P., Krishna M., “Evaluation of olibanum resin as a new microencapsulating agent for aceclofenac controlled release microcapsules,” Indian J. Pharm. Sci.. 68, (4), 461 –464 (2006).**CrossRef**

12

Fehsel K. et al., “Necrosis is the predominant type of islet cell death during development of insulin-dependent diabetes mellitus in BB rats,” Lab. Invest.. 83, (4), 549 –559 (2003).**CrossRef**

13

Chang N. et al., “Direct measurement of wound and tissue oxygen tension in postoperative patients,” Ann. Surg.. 197, (4), 470 –478 (1983). 0003-4932 **CrossRef**

14

Spokane R. B. et al., “An implanted peritoneal oxygen tonometer that can be calibrated in situ,” ASAIO Trans.. 36, (3), M719 –M722 (1990). 0889-7190

15

Schrenzenmeir J. et al., “Effect of microencapsulation on oxygen distribution in islet organs,” Transplantation. 57, (9), 1308 –1314 (1994). 0041-1337

16

Schrezenmeir J. et al., “The role of oxygen supply in islet transplantation,” Transplant. Proc.. 24, (6), 2925 –2929 (1992). 0041-1345

17

Michiels C., “Physiological and pathological responses to hypoxia,” Am. J. Pathol.. 64, (6), 1875 –1882 (2004).**CrossRef**

18

Veriter S. et al., “In vivo selection of biocompatible alginates for islet encapsulation and subcutaneous transplantation,” Tissue Eng. Part A. 16, (5), 1503 –1513 (2010). 1937-3341 **CrossRef**

19

Bonner-Weir S., “Morphological evidence for pancreatic polarity of β-cell within islets of Langerhans,” Diabetes. 37, (5), 616 –621 (1988). 0012-1797 **CrossRef**

20

De Vos P. et al, “Why do microencapsulated islet grafts fail in the absence of fibrotic overgrowth?,” Diabetes. 48, (7), 1381 –1388 (1999). 0012-1797 **CrossRef**

21

Schrezenmeir J. et al., “Immobilized hemoglobin improves islet function and viability in the bioartificial pancreas in vitro and in vivo,” Transplant. Proc.. 26, (2), 792 –800 (1994). 0041-1345

22

Quaranta M., Borisov S. M., Klimant I., “Indicators for optical oxygen sensors,” Bioanal. Rev.. 4, (2–4), 115 –157 (2012).**CrossRef**

23

Borisov S. M. et al., “Phosphorescent platinum (II) and palladium (II) complexes with azatetrabenzoporphyrins—new red laser diode-compatible indicators for optical oxygen sensing,” ACS Appl. Mater. Interfaces. 2, (2), 366 –374 (2010). 1944-8244 **CrossRef**

24

Carraway E. R. et al., “Photophysics and photochemistry of oxygen sensors based on luminescent transition-metal complexes,” Anal. Chem.. 63, , 337 –342 (1991). 0003-2700 **CrossRef**

25

Ladurner R. et al., “Predictive value of routine transcutaneous tissue oxygen tension (tcpO2) measurement for the risk of non-healing and amputation in diabetic foot ulcer patients with non-palpable pedal pulses,” Med. Sci. Monit.. 16, (6), 273 –277 (2010). 1234-1010

26

De Backer D. et al., “Monitoring the microcirculation in the critically ill patient: current methods and future approaches,” Appl. Physiol. Intensive Care Med.. 2, , 263 –275 (2012).**CrossRef**

3.4 Analyte Sensor Design Process

Large Scale Sensor *In Vitro*:

A glucose sensor of aspect ratio 1:3 (width to length) was made by hand on a large scale (~20x, compared to the planned final size). First, a piece of Scotch™ Tape was coated with a thin layer of Pt/Pd-Porphyrin dye (~5μm thick) and it was cut into a strip with a razor under a stereomicroscope to a size of ~3x9mm. Then a pHEMA GOX/CAT hydrogel was formed on top of the dye (~50μm thick). A glucose impermeable barrier layer (implant grade RTV silicone, NuSil MED 1000) was coated over 3/5's of the strip leaving ~3 mm of enzyme exposed (the entrance region) and the rest covered (Fig. 3.8A). Lifetime measurements were taken of the dye as the sensor was exposed to different glucose concentrations. The laser beam interrogating the dye was moved longitudinally using a micrometer stage in order to interrogate different spots of dye along the sensor and observe the oxygen gradient that is set up by the GOX reaction and the no flux boundaries created by the NuSil layer (Fig 3.8B). The sensor was put into a chamber between two glass slides and PBS, 40 mg/dl glucose solution, 130 mg/dl glucose solution, and 450 mg/dl glucose solution were injected into the chamber individually surrounding the sensor with fluid. Lifetime measurements were taken at 6 different spatial areas along the sensor for each solution with a laser spot size of approximately 3 mm diameter. Spot 0 was completely over the entrance region and the center of the laser spot was moved 1 mm towards the NuSil coated end for each separate spot. Examples of spot 0 (entrance region), spot 3 (3 mm from spot 0, half over entrance/half over NuSil), and spot 5 (5 mm from spot 0, over Nusil) are shown in Fig. 3.8B. The fitted continuous lifetime measurements of the Pd-Porphyrin dye for the sensor starting in glucose free PBS and then covered with 130

mg/dl glucose solution are shown in Fig. 3.8C. As the glucose begins reacting with the GOX hydrogel oxygen is consumed and the lifetime rises as the dye is interrogated over the entrance region. Once the reaction has peaked the laser spot is moved 3 mm to spot 3 and the lifetime is recorded there where the lifetime is lower because the reaction is partially restricted by the NuSil coating. The center of the laser spot is then moved 2 mm further so it is fully over the NuSil and the recorded lifetime is only slightly elevated compared to no glucose due to the restriction of the no flux boundaries on all sides except the entrance. The diffusional distance for glucose from the entrance at the NuSil interface to the center of the laser spot at spot 5 is about 1 mm. The GOX reaction has started to consume glucose at a higher rate than it can diffuse though setting up a gradient in glucose and oxygen concentration in this area. The laser spot is interrogating a large area and the fitted lifetime that is returned is the average lifetime over that 2 mm area. Hence, most of the area interrogated by spot 5 is still in room air oxygen but a small portion near the entrance has less oxygen due to the diffusion of glucose through the GOX hydrogel under the NuSil causing the reported lifetime to be slightly elevated from room air. As the glucose concentration increases more glucose will diffuse farther into the gel before it is consumed, and vice versa for lower glucose concentrations. Fig. 3.8D shows the lifetime data acquired at each spatial location at 40, 130 and 450 mg/dl glucose. A curve is developing for each of these interrogation spots that will allow us to calibrate for glucose concentrations between 40 and 450 mg/dl by using multiple spatial sights. The three measured glucose concentrations over the entrance form the three point calibration curve in Fig. 3.8E, showing high sensitivity in the **Hypoglycemic range** (<70mg/dl). The same three point calibration curve was plotted in Fig. 8F, showing high sensitivity in the **Euglycemic range**

(70-120mg/dl), and at spot 5, (Fig. 3.8G), showing high sensitivity in the **Hyperglycemic range** (>120mg/dl).

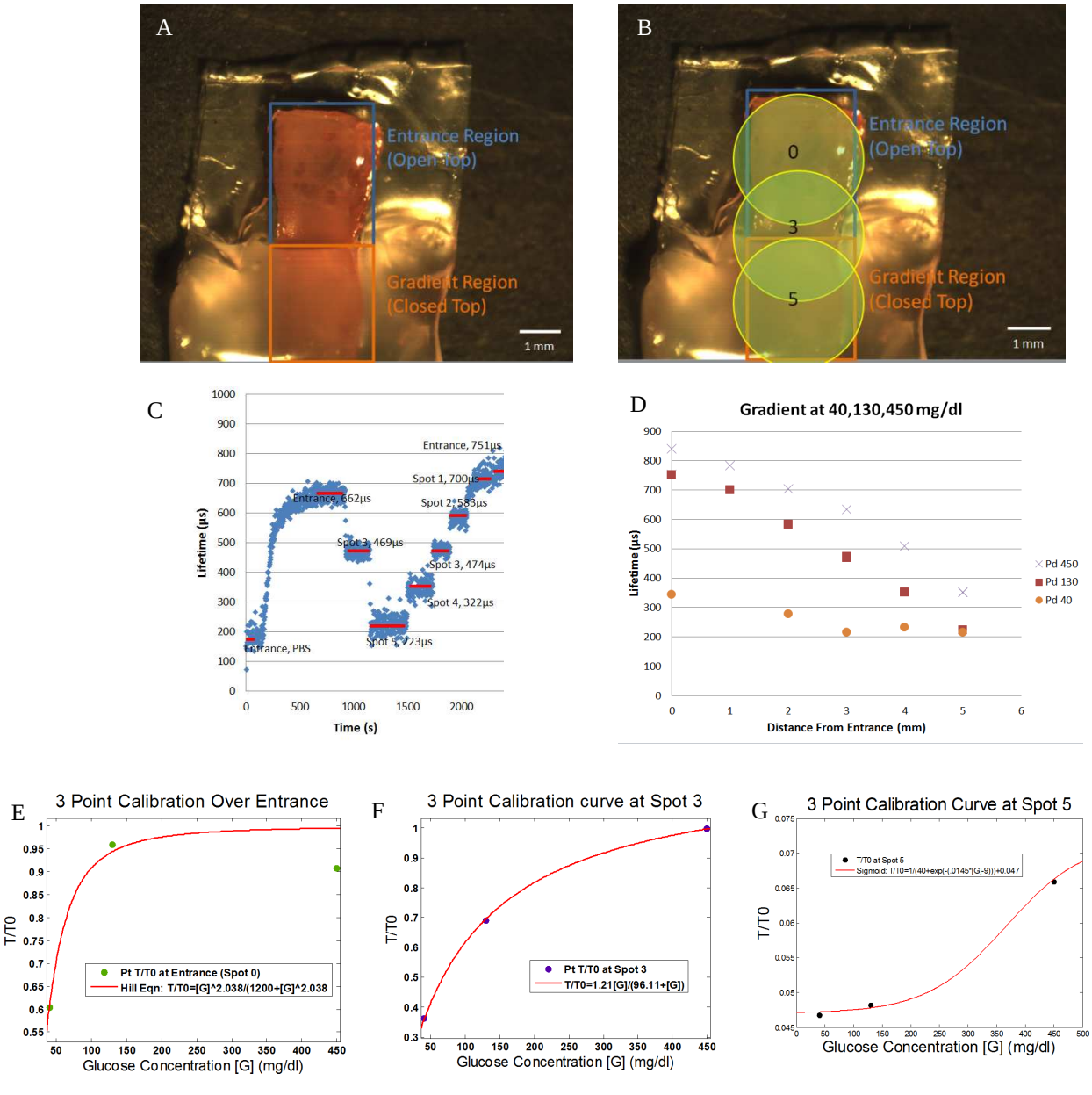

Fig. 3.8 Large Scale Sensor A) Image of large scale sensor showing exposed entrance region and closed Nusil region. B) A laser spot of 3 mm diameter interrogates the dye in different areas of the sensor to gain sensitivity across the physiological range of glucose concentration. C) Continuous lifetime measurements of the sensor starting with PBS and then injecting 130 mg/dl glucose solution and moving the laser spot spatially. D) Lifetime decreases as I interrogate the sensor further from the entrance because of the NuSil restriction, giving different curves for each concentration. E,F,G) 3 Point calibration curves for 3 different spatial interrogation points on the sensor; the entrance is sensitive to hypoglycemia, Spot 3 is sensitive to euglycemia, and Spot 5 is sensitive to hyperglycemia.

After measuring the sensitivity curve at different spots along a large sensor (3x9mm) partially coated with silicone (which is impermeable to glucose or lactate), we realized that it might be possible to excite an entire sensor made exactly like the portion of sensor that was excited at spot 3 and have sufficient sensitivity across the clinical range. This was an important realization because we had previously thought that we would need to interrogate the sensor at different spatial locations along the length of the reaction to get enough sensitivity. To achieve this we had planned to pattern different dyes that could be spectrally separated along the length of the reaction chamber (Fig. 3.9).

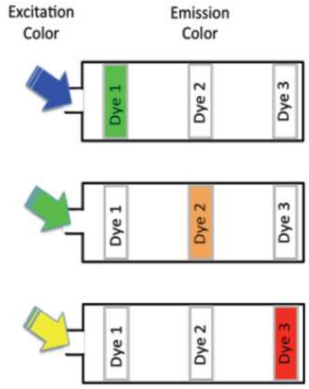

Fig. 3.9 Initial Sensitivity Improvement Scheme. Initial plan to improve sensitivity by interrogating a rectangular reaction chamber at different spatial locations with spectrally separable dyes.

Before attempting the complicated manufacture of a device with multiple dyes, I tried the simplest approach which was to make a sensor by hand, similar to, but smaller than the sensor used in figure 7 (shown in fig. 3.9). I made a set of sensors using this technique (fig. 3.10a) and found that about 5% of the sensors had sufficient sensitivity range and response time (fig 3.10b), while the majority of sensors made by hand exhibited long, drifting response with saturation at low concentrations (fig 3.10c).

The relatively large sensors I was making by hand were not reproducible, even though every once in a while one would work well. I organized a list of the factors that may be

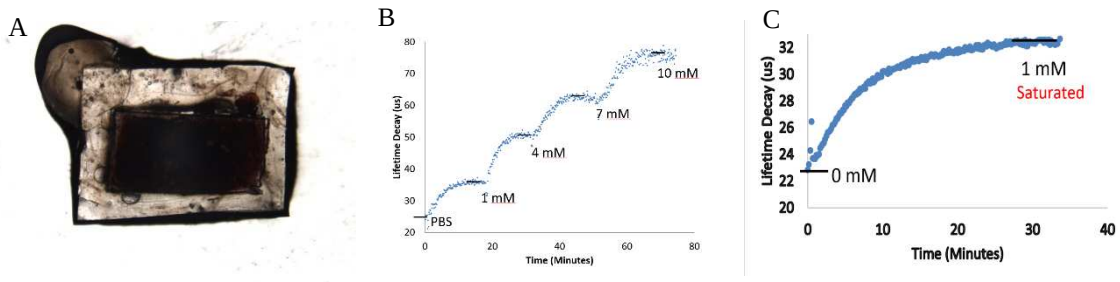

Fig. 3.10 Hand-Made Sensor Performance. A. Hand-made sensor partially coated in silicone. The dark rectangle in the middle contains the dye and enzyme with an entrance region exposed for glucose or lactate in solution to enter the reaction chamber. B. Few sensors made in this way respond well to increasing lactate concentration. C. Most sensors built in this way have drifting response and low sensititvity range. This plot is an example of a sensor made in this way whose response over 30 minutes drifted upwards until saturating even at low concentration (1 mM lactate). The sensor does not respond to further increases in lactate.

contributing to the lack of reproducibility. The factors included: size of sensor, amount of dye added, amount of enzyme added, thickness of dye and enzyme layer, amount of NuSil added, thickness of NuSil layer, and the amount of reaction chamber covered by NuSil. A new manufacturing method was needed due to the inaccuracies of production by hand.

Dr. Botvinick and I had previously come up with a plan to create very small reaction chambers using photolithographically produced molds. The small chambers (~100x350x 100 microns) would theoretically be loadable with very precise amounts of reagent (dye and enzyme) that would fill the highly reproducible area created via photolithography with accuracy down to at least less than 5 microns. A rectangular reaction chamber shape was chosen and various parameters were identified that may affect the response of the sensor (shown in fig. 3.11). Rather than patterning dye spots along the bottom as drawn in fig. 3.11, I now planned to coat the entire bottom of the reaction chamber with dye and excite the entire volume at one time, effectively averaging the gradient of lifetimes that would exist throughout the length of the chamber during use. I was able to get a mold made with various sizes of reaction chambers to test the effects of changes in size on response to analyte concentration when loaded with reagents by collaborating with Dr. Elliot Hui's lab. I drew a two dimensional figure containing the various reaction chamber outlines and it was made into a mask to be used for photolithography. Graduate student Phil Thomas used that mask to make a mold out of SU-8 (photopolymerizable epoxy) in a clean room environment (fig. 3.12). I then took the SU-8 mold and molded polydimethylsiloxane (PDMS) so that it now contained the highly reproducible reaction chambers with tight tolerances ready to be filled with reagents. Unfortunately, it was very difficult to load the reagents into the highly

Fig. 3.12: Single Reaction Chamber. One reaction chamber formed by photolithography in SU-8 on a silica wafer

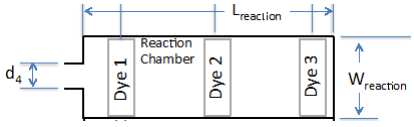

Figure 3.11 Sensor Parameters. Top-view dimensional drawing of a single reaction chamber and oxygen conduit. The four dye regions sit within the floor of the device, all other lines are vertical walls made of elastomer.

hydrophobic PDMS, though I was able to get a couple of the chambers loaded. In addition to the loading issues, the reaction chambers were so small that it was difficult to measure the signal return from the small volume of dye that filled the chamber. I tried to measure the chambers that I was able to load with reagents, but was unable to obtain sufficient intensity of return signal (dye emission) using my current fiber-based probe setup. This made it impossible to test the changes in reaction chamber size without assembling a completely different excitation and detection system. At this point we had to choose whether to make a more expensive, highly sensitive detection system, or change the sensor design to improve signal intensity while maintaining the reproducibility of the accurate, small reaction chambers formed by photolithography. This need sparked an idea for a new design of a biosensor using optical means of interrogation. Dr. Botvinick and I realized that we could increase the intensity of signal return by simply creating multiple small reaction chambers patterned onto one 'chip' that could be excited by light all at the same time. The multiplexed reaction chambers' intensity would multiply according to the number of added reaction chambers, and the response of each individual reaction chamber would remain the same! An early drawing of this concept is depicted in fig. 3.13.

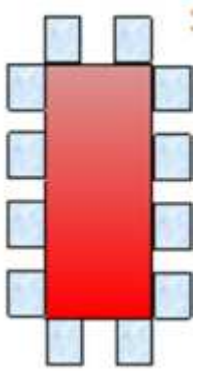

Fig. 3.13 Multiplexed Reaction Chambers. An early concept of the multiplexing of small reaction chambers for signal multiplication. Reaction chambers (in blue) are placed around a structure to hold them together (in red).

We came up with a few different designs for manufacturing multiplexed small reaction chambers that involved laser cutting of materials to be loaded with reagents. All of these initial designs failed due to either difficulty loading reagents consistently or inconsistent

manufacture. Dr. Botvinick, and a post-doctoral scholar who recently joined our group (Dr. Sean White), and I met to redesign the sensor to increase reproducibility. Dr. White mentioned a technique for loading small channels with liquids that he had used in microfluidic studies which led to the use of a loading technique inspired by microfluidics for our sensors. I drew a new outline of a thin channel that was folded repeatedly to increase the surface area while allowing reagents to flow through its entire length (fig. 3.14). I also included regions to load the liquid reagents so that they would travel through the channel via capillary action.

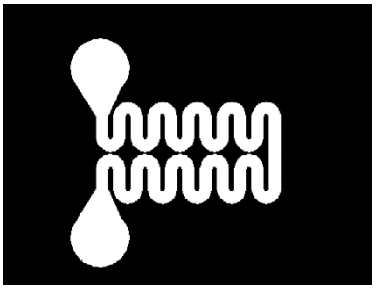

Fig. 3.14 Channel Sensor. Drawing of a 'channel sensor' design consisting of one connected channel with loading zones (large circular areas). The channels will be separated later in the manufacturing process.

These 'channel sensors' can be formed via photolithography with tight tolerances (<5 micron). An SU-8 mold with multiple sensors employing different channel width and total sensor length was made, where the white portion in fig. 3.15 is a negative feature. Then PDMS can be molded off of the SU-8 to form a new mold with positive features. An implant grade epoxy can then be molded off of the PDMS to form the negative features of the channels, ready for loading in a material that is less hydrophobic than PDMS, and stiffer, to provide less bending which can delaminate the dye layer from the enzyme layer. The newly formed epoxy sensor bodies can be filled with dye by placing a drop into each of

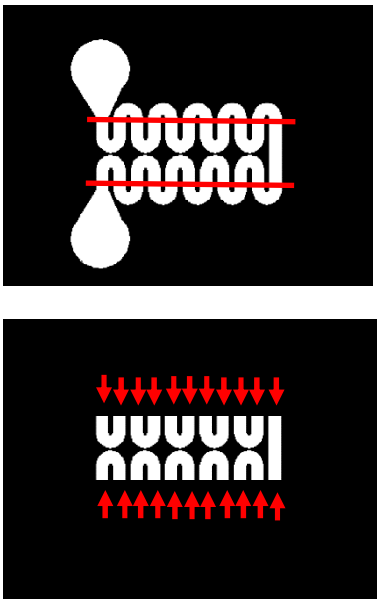

Fig. 3.15 Channel Sensor Chopping. The 'channel sensor' is chopped with a razor along the lines drawn in red, individuating small chambers and exposing an entrance for analyte to diffuse into on the side (direction of analyte diffusion indicated by red arrows).

the loading zones on either side. After the dye is dry, a photopolymerizable liquid mixture of hydrogel components and enzyme is added to fill the remaining space in the channel and is polymerized by exposure to UV light. To seal the top of the channel a layer of NuSil is knife-coated over the entire top surface at a thickness of about 10 micron. The Nusil is allowed to dry and then the sides of the channels are chopped off to expose entrance holes for analyte to diffuse into on the side of each newly separated channel (fig. 3.15).

The sensors are then ready to be hydrated (soaked in saline solution to wet the hydrogel) and tested for sensitivity. Images of an actual sensor made using this process are in fig. 3.16.

Fig. 3.16 Manufactured Channel Sensor. A. The channel sensor formed in epoxy is filled with dye (green) and enzyme hydrogel (clear) and coated with a 10 micron layer of NuSil. B. Then the sensor is chopped to individuate the channels and expose entrance holes on the side. C. Side view of sensor, showing entrance holes.

Sensors of 200, 125, and 50 micron channel width were made using this process. Results showed that the sensitivity range was equal for all channel widths tested, but the dynamic range of the sensor response was lower in the 50 micron channels. The sensors made with 200 micron channels had more variability than the 120 micron channels, so the 120 micron channels were chosen to use for further characterization testing and *in vivo* testing.

In vitro calibrations of 40 lactate sensors made with the same materials and processes in the 120 micron channel sensors were performed. A typical calibration curve is shown in fig.

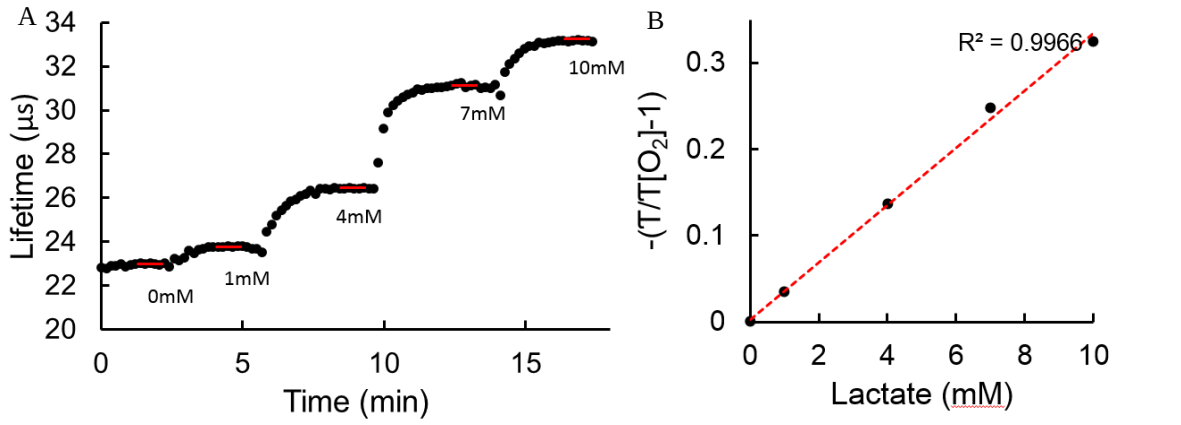

Fig. 3.17 Channel Sensor *In Vitro* Performance. A. The sensor is exposed to increasing lactate concentrations *in vitro* and the sensor's steady state lifetime value at each concentration is recorded. B. The steady state lifetimes are plugged into a modified Stern-Volmer equation and plotted against lactate concentration. A line is fit to the data creating a calibration curve that can be used to convert sensor lifetime values into lactate concentration.

3.17.

Most of the 40 sensors made (28 out of 40) had a sensitivity range at or above 10 mM, confirming the reproducibility of the sensors. 2 of the 40 sensors failed due to errors in manufacturing and had no sensitivity to lactate. A histogram showing the peak sensitivity range (saturation point) for each sensor is shown in fig. 3.18. Sensors that saturated before 10 mM were not used for *in vivo* testing because the animal models I used produce high lactate levels and we wanted to track the lactate level as high as possible. *In vivo* testing would show that conditions different than *in vitro* test conditions seemed to allow the sensors to achieve a higher sensitivity range *in vivo*.

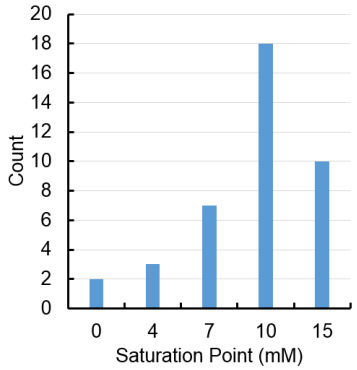

Fig. 3.18 Channel Sensor Sensitivity. The saturation point of 40 sensors made using the same manufacturing technique was measured. Most sensors saturate between 10 -15 mM lactate.

3.5 Continuous Lactate Monitor Performance *In Vivo*

Dr. Matthew Brenner's lab at the Beckman Laser Institute is investigating the effectiveness of novel drug therapeutics to reverse cyanide poisoning. They developed a robust rabbit model of lethal cyanide poisoning followed by injection of a potential antidote. They monitor the anesthetized animal's responses and status over the course of the experiment. This is a great model to test the use and accuracy of a CLM because cyanide is known to cause a buildup of lactate, and consumption thereof upon recovery. This would allow us to test our CLM *in vivo* throughout the clinical/pathological range of lactate values. I tested many different sensor designs in the rabbit cyanide poisoning model in collaboration with the Brenner group and compared the results from a set of experiments performed using the same sensor design for each implanted sensor. The unpublished results are as follows:

Continuous Lactate Monitoring of Cyanide Poisoning in a Rabbit Model with an Implantable, Optical Sensor

Introduction:

There is a need for rapid identification and ability to continuously monitor patients with potential cyanide exposure. Cyanide remains a critical threat to civilian and military personnel through its numerous sources of exposure (Hall and Rumack, 1986). One of the main sources of exposure is smoke inhalation from the combustion of plastics, such as acrylics and acrylonitriles, commonly used in modern commercial and residential construction. Studies of victims of residential fires have found higher blood cyanide concentrations in the deceased than in the survivors, suggesting cyanide toxicity may predominate over carbon monoxide poisoning (Barillo *et al* 1994, Baud *et al* 1991, Riddle 2004, Strickland *et al* 1992). Cyanide poisoning severity is known to have a strong correlation with blood lactate concentration (Graham, 1977) due to cyanide's mechanism of impairing the tissue's ability to utilize oxygen by binding the active site of cytochrome c oxidase. Once bound, the electron transport chain, essential to the oxidative phosphorylation process, is arrested in its reduced form, preventing the donation of an electron. Progressive cytotoxic tissue hypoxia develops. Non-specific symptoms such as pulmonary edema and lactic acidosis are resultant (Graham 1977, Way 1988). Lactic acidosis results from the shift in metabolic state from oxidative phosphorylation (aerobic metabolism) to anaerobic metabolism of glucose, where lactate is produced. High blood lactate concentration confirming metabolic acidosis is key to diagnosing cyanide poisoning, as the symptoms are non-specific. Laboratory tests to measure blood cyanide concentration take too long to be used in directing management of the condition, and are mainly used as confirmation after the treatment period has ended (Brierley *et al* 1976, Groff *et al* 1985). In cases of smoke inhalation, lactate levels greater than 10 mM predict cyanide poisoning with high sensitivity and specificity (Baud 1991).

Frequent measurements of blood lactate concentration have been shown to be a powerful biochemical indicator commonly used to stratify risk and to assess adequacy of resuscitation in critically ill patients (Jansen, 2010). Blood lactate has been reported to be a superior resuscitation endpoint compared to other variables (standard vital signs like heart rate, blood pressure) (Jones 2010). Changes in lactate levels over time can suggest hemodynamic instability or insufficient response to treatment that might justify additional diagnostic or therapeutic interventions (Jansen 2010). Clinical studies show that frequent measurement of lactate reduces the incidence of severe shock, organ failure and death during trauma by indicating early resuscitation (Jansen 2010). Knowledge of lactate concentration and lactate dynamics is important for indicating treatments for hemorrhagic shock (Brohi 2011), cyanide poisoning (Graham, 1977), hypoxia (Hosogai, 2007), and sepsis (Bakker, 1996, Nguyen, 2004) among other life-threatening illnesses. Rising lactate levels are strongly related to the Sequential Organ Failure Assessment (SOFA)

score and consequently, early resuscitation in response to increasing blood lactate has been shown to prevent organ failure (Bakker, 2013).

To address the needs of cyanide poisoning victims, and the needs of many other critical monitoring events, we have developed a continuous lactate monitor that has the potential to provide current lactate levels and trends of rising or falling lactate, without the need for multiple blood draws or manual analysis. To test the efficacy of the sensor we have performed rigorous *in vitro* testing as well as *in vivo* testing in animal models. In order to test the sensor's *in vivo* response to rising and falling lactate levels across the physiologic range we have used a rabbit model of cyanide poisoning with potential recovery from a drug meant to counter the effects of cyanide in the body.

Sensing background:

Continuous lactate sensing for biological applications has been reported (Hu, 1993, Baker, 1995) but there are still no commercial products for continuously measuring lactate. Approaches for continuous lactate sensing have included subcutaneous electrodes (Hu 1993, Baker 1995), non-invasive all-optical methods (Berger, 1996, Sivakesava, 2001, Tamburini 2003), or non-invasive electrode methods using alternative body fluids (i.e. sweat, saliva, tears) (Jia 2013, Kim 2014). The most successful approaches in animal studies have been the subcutaneous electrodes that operate on the same basic principles as current gold-standard bench top analyzers (i.e. YSI 2300), but fail to match the performance of bench top systems *in vivo*. Non-invasive methods typically suffer from interferents (low specificity for lactate), or poor correlation of measurements to blood lactate concentration.

Optical methods using light-emitting compounds for sensing biological analytes have gained popularity due to their stability and accuracy. A class of bright, stable luminophores with oxygen sensitive output called metalloporphyrins are being used frequently in biosensors, such as oxygen and glucose sensors in laboratory tests (Kocincova, 2007, Pasic, 2007). In the case of lactate, by coupling an oxidase enzyme with high specificity for lactate (lactate oxidase) to an oxygen-sensitive metalloporphyrin in a controlled fashion the dye emission is mediated by lactate concentration. Oxygen-sensitive porphyrin dye emission has been measured on the tip of fiber optic probes (Kocincova, 2007) and has been measured through tissue (Borisov, 2008). Our group has also previously shown that pO_2 can be measured through tissue *in vivo* using implanted porphyrin dye based sensors (Weidling, 2014). This proved that our sensors employing porphyrins could be implanted in tissue and measured from outside the body by passing light through skin. A similar approach has been described before for glucose sensing, where instead of using porphyrin compounds, implanted fluorescent molecules were measured from outside the body (Nielson, 2009). Lifetime measurements of the fluorescent decay were measured rather than intensity to avoid interference from changes in tissue light absorption and scattering properties. Our sensing platform also uses lifetime measurements to avoid interference common with intensity measurements. We have

created a new sensor design taking advantage of the stability and brightness of oxygen-sensitive porphyrins that can be coupled to oxidase enzymes in a biocompatible, mass manufacturable package that can be easily implanted, and measured by a reader unit made of low-cost components.

Materials and Methods:

Sensor Design:

Lactate sensors are comprised of reaction chambers filled with a thin layer of oxygen sensitive dye (Platinum Tetraphenyl Tetrabenzoporphyrin, Frontier Scientific) covered with a hydrogel containing an oxidase enzyme (Lactate Oxidase, Sekisui). The Lactate Oxidase (LOX) consumes oxygen and lactate when both are present and produces pyruvate and hydrogen peroxide. Sensors are made by patterning multiple reaction chambers onto one 'sensor chip'. Reaction chambers allow lactate and oxygen in solution to react with LOX. The chambers should be relatively small in order to allow for short diffusional lengths of analyte into a constrained reaction chamber. A single small reaction chamber has little signal that can be collected though, especially if we are to measure the signal from the reaction chamber through biological tissue that will absorb and scatter the emitted light. To overcome this we have patterned many reaction chambers onto the same sensor chip, which provides signal multiplication while maintaining the sensitivity and dynamic response of a small reaction chamber. Short diffusional lengths of analyte can also be obtained in a sensor by creating a thin layer of reactive enzyme over a larger area, but the bulk reaction created by this kind of design can lead to drifting response due to diffusion in multiple directions; or the reaction may become saturated at low levels of analyte, requiring the need for another porous layer to restrict diffusion. Adding a layer to restrict diffusion reduces sensitivity to low levels of analyte and makes the sensor calibration highly dependent on how well stirred/mixed the sensor's environment is, which may vary in the subcutaneous space. By controlling the geometry of the reaction and the size of the analyte diffusional entrance on a small scale we have been able to avoid loss of sensitivity in the lower analyte concentrations and avoid drifting responses, while achieving high signal-to-noise through tissue due to the multiplexing of reaction chambers.

Our sensor measures the amount of oxygen consumed in the LOX enzyme reaction which includes consumption of both lactate and oxygen. In order to control for the effects of changing oxygen concentration within the tissue, and ensure that the measurements taken from the sensor depend on only lactate concentration, we have used an oxygen sensor as a reference. The oxygen sensors are made identical to lactate sensors except the LOX enzyme is removed from the hydrogel. Oxygen sensor measurements can then be directly subtracted from lactate sensor measurements, leaving a measurement that is solely affected by lactate concentration.

Sensor Manufacture:

A wafer of sensor chips was produced by photolithography in SU-8. Then polydimethylsiloxane (PDMS, Dow) was molded off of the SU-8 wafer to make a positive mold that could be used to mold harder plastics. The PDMS mold was coated with epoxy (Epotek 301), bubbles were removed and it was allowed to dry. The molded epoxy formed a thin sheet of many separate patterned channels ready to load with the dye and enzyme mixtures. 2 µl of dye solution (2 mg PtTPTBP and 30 mg polystyrene dissolved in 450 µl chloroform) can be loaded into all of the interconnected channels at once through capillary action, where it dries in a thin film at the bottom of the channels. Then a proprietary hydrogel containing LOX was deposited over the top of the channels such that it accumulates in the channels, covering the dye, where it is UV cured. A silicone layer is then knife-coated over the channels to seal in the reagents and allowed to dry. Finally, the channels are chopped with a razor blade at a specified length to expose the hydrogel at the entrance to each channel (Fig. 1). Sensors are hydrated in phosphate buffered saline (PBS) solution prior to testing. Oxygen sensors are made in the same way, but without enzyme in the hydrogel portion.

Probe Design

The PtTPTBP dye being used has high quantum efficiency (~50%) (Borisov, 2010)[9], and absorption/emission spectra that lie in the 'optical window' for low tissue absorption and scattering, enabling the use of low-cost, widely available amplified silicone photodiodes to detect the emission signal from the sensors implanted in tissue. LED's provide a low-cost alternative to laser excitation sources and are safer for passing light through tissue. The red-orange LED's (Phillips LumiLEDs, Luxeon Star) used have a wavelength emission centered at 615nm which matches up well with the PtTPTBP absorption peak at 614nm. Rather than using fiber optics to guide light into tissue, or guide light onto a detector, we placed LED's around a large area photodetector (PDA100A, ThorLabs) to take advantage of the light scattering properties of the tissue (Fig. 2).

In Vitro Validation

We confirmed the sensitivity of the implantable sensors to lactate on the bench-top prior to implantation. After sensors are hydrated in a well in a 24 well plate filled with 1 mL of 1X phosphate buffered saline solution (PBS), they are tested for responsivity *in vitro* by applying pre-mixed lactate solutions and measuring the sensor's response. The well is aligned over the probe, sensor signals are collected and lifetime decays are recorded every 10 seconds. Once a baseline has been established, different lactate concentrations are added to the sensor, and a steady state response lifetime is recorded for each concentration (Fig. 3a). The steady state response values can be used to create a calibration of corresponding lifetime values to lactate concentration (Fig. 3b). Sensors were also tested to confirm sensitivity *in vitro* upon completion of the *in vivo* experiments.

In Vivo Validation

Animal Preparation:

Animal procedures were reviewed and approved by the University of California Irvine (UCI) Institutional Animal Care and Use Committee (IACUC). Twelve pathogen-free New Zealand White rabbits (Western Oregon Rabbit Supply, Philomath, Oregon), weighing 3.5-4.5 kg were used in this study. Animals were anesthetized with an intramuscular injection of Ketamine HCl 50mg/kg (Ketaject, Phoenix Pharmaceutical Inc., St. Joseph, MI) and Xylazine 5mg/kg (Anased, Lloyed Laboratories, Shenandoah, IA) and intubated. After the initial injection, a catheter was placed in the animal's marginal ear vein to administer continuous intravenous anesthesia with Ketamine/Xylazine. Animals were mechanically ventilated (dual phase control respirator, model 32A4BEPM-5R, Harvard Apparatus, Chicago, IL) at a rate of 20 respirations per min, a tidal volume of 50 cc, and inspired O_2 concentration of 100%. A pulse oximeter (Biox 3700 Pulse Oximeter, Ohmeda, Boulder, CO) with a probe was placed on the tongue, to measure SpO_2 and heart rate. Arterial and venous femoral lines were placed. A lactate sensor and a separate oxygen sensor were made one day prior to implantation. The rabbit belly was shaved and an incision was made penetrating to the subcutaneous space. Blunt dissection was performed with forceps to open a small pocket in the tissue of the subcutaneous space (~1-3 mm deep). The small (4x2x1mm) lactate sensor was placed in the pocket and the wound was closed with a cyanoacrylate based wound sealing adhesive (Gluture, Abbott). The oxygen sensor was placed in a separate subcutaneous pocket approximately 9 cm away from the lactate sensor so that both probes would be aligned above their respective sensor (Fig. 4). Probe alignment was performed by measuring the signal intensity return as the probe was moved above the area of the implant until the spot with the highest return intensity was found. The probes were then locked into place using optical mounting hardware (Newport Optics) and taped to the skin with Tegaderm™ (3M) to avoid shifting position relative to the implant. A lifetime measurement from each sensor was taken at 10 second intervals over the duration of the experiment (each measurement was the averaged lifetime from 25 decays collected at 100 Hz and has high signal to noise ratio (SNR>100). The lifetime calculation has been previously described in detail (Weidling, 2014).

Cyanide Infusion:

20 mg of sodium cyanide (Sigma-Aldrich, USA) dissolved in 60 ml of 0.9% NaCl iwas infused intravenously at .33 mg/min (1cc/min). Cyanide was continuously infused for 30 minutes with 100% oxygen input from the ventilator. Time point measurements, which include arterial and venous blood gases, systemic pressures, heart rate, and SpO_2 were taken at times: 15 min after cyanide infusion has started, 25 minutes, and 35 minutes. At the 30-minute post cyanide infusion time point, the ventilator inlet source was changed from 100% O2 to room air, and the ventilator setting was adjusted to 16 breaths per minute. At about 45 minutes after cyanide fusion begins, a drug meant to reverse the effects of cyanide poisoning was administered intramuscularly (drug used was either DMTS, DMTS and Cobinamide, l-lys sulfanegen, or Spiro-indol). Results for the effectiveness of each drug tested will be published elsewhere. Blood was sampled at time points 5, 10, 15, 30, 45, 60, 90, 120 minutes after the recovery drug is injected and lactate concentration and pH were measured. The rabbit's blood pressure was monitored

throughout the experiment and euthanasia was administered at any time the diastolic blood pressure dropped below 20 mmHg. If the rabbit survived the poisoning event (maintained blood pressure for the duration of the cyanide infusion), monitoring continued for 90 minutes after the injection of drug, or was carried out longer to observe the recovery period, if indications of recovery were present (e.g. falling blood lactate concentration, improving vitals). At the 90-minute time point (or upon completion of recovery observation), final measurements were taken, and the subjects were euthanized with an intravenous injection of 1.0-2.0cc Euthasol (Virbac, Ft. Worth, TX) through the marginal ear vein catheter and the lactate and oxygen sensors were retrieved and tested for responsivity.

Results:

Data was collected from implanted sensors in 11 different rabbit models of lethal dose cyanide poisoning with potential recovery, and in one other rabbit where no cyanide was administered to show that the sensor's response tracks lactate in non-cyanide events also. Typically, the oxygen reference corrected signal from our implanted sensor had a short 'warm up' period where the sensor output dropped to a baseline level over about 15-30 minutes. Blood was sampled at this baseline value and then cyanide infusion began. Tissue lactate (as measured by our implanted sensor) (TL) was measured every 20 seconds. Blood lactate (BL), pH, heart rate (HR), blood pressure (BP), and oxygen saturation (SpO_2) were measured at the time points specified above.

A typical curve showing the implanted sensor response correlated to blood lactate values in a cyanide poisoned rabbit is shown in Fig. 5a. In this experiment the rabbit does not survive through the cyanide infusion, and showed no signs of recovery. In 6 of the 11 cyanide experiments the rabbit survived through the completion of the cyanide infusion, and in two of those survivors, indications of recovery were present. Signs of recovery included falling blood lactate values, increasing blood pressure, and increasing SpO_2. These signs prompted an extended monitoring period to observe the recovery period. In one of the survival cases the implanted sensor had become saturated 5 minutes before the administration of the drug and could not be correlated to blood lactate after the saturation point. Therefore no data analysis or comparison was performed on that implanted sensor data during this recovery period. In the other survival case where the rabbit appeared to be recovering, measurements were collected for an additional 120 minutes to observe the dynamics of recovery (see Fig. 5b). In this experiment it was observed that the lactate-specific response of the sensor implanted in the tissue began to fall about 30 minutes before blood lactate values, upon recovery. Sensors were also tested for sensitivity upon explant, confirming that 100% of sensors remained responsive to lactate after the *in vivo* experiment.

In the experiment where no cyanide was administered, the blood lactate and sensor response remained relatively flat compared to the cyanide group. Blood lactate in the non-cyanide animal varied between 0.8 to 4.5 mM and tissue lactate (measured by our calibrated implanted sensor) varied between 0.4 to 4.6 mM. Blood and tissue lactate concentration increased significantly in every cyanide poisoned animal, as expected. Table 1a is a summary of implanted sensor measurements compared to blood lactate measurements in the 11 cyanide poisoned animals. The average percent difference between tissue and

blood lactate low values was 8.4% and at peak values was 1.8%. The rate of lactate concentration increase from the beginning of cyanide infusion to the end of infusion was also calculated and the percent difference between tissue and blood lactate rate of rise was 5.3% (Table 1a).

The accuracy of the implanted sensor response to rising lactate was evaluated as compared to blood lactate measurements of arterial blood samples. The measurements were performed either at the point of care with a Nova Lactate Plus meter, or at the completion of the study with a YSI 2300 lactate analyzer, using blood samples stored on ice in heparin lined vials. Implanted sensor values were calibrated to blood measurements using a 2-point calibration method. One low blood lactate measurement (before cyanide) and one high blood lactate measurement (during or after cyanide) was chosen for each sensor and the implanted sensor lifetime (in µs) at the corresponding time-point was fixed to the blood lactate concentration in mM. Using these two points, the gain (*m*) and offset (*b*) were calculated using the following equation and the resulting values were used to convert the entire implanted sensor lifetime into lactate concentration in mM.

$$CTL = m(ISL - BL) + b$$

Where *CTL* is the converted tissue lactate in mM of the implanted sensor, *ISL* is the implanted sensor lifetime measured by our probes (calculated by subtracting oxygen sensor lifetime from lactate sensor lifetime in µs), *BL* is the blood lactate concentration in mM, *m* is a gain factor calculated using the two-point calibration, and *b* is an offset factor calculated using the 2-point calibration method. Data during the warm up period (before baseline measurement) and data taken during a recovery period (falling lactate values) was not used as a part of this analysis. Recovery period values were not used because of the apparent time-dependent physiological differences between tissue and blood lactate (dynamic delay) during that period. Average error between blood lactate and the implanted sensors was 26%, with 67% of data within 20% (n=87) (shown as an error grid in Fig. 6a). Factors that contributed to error between reported tissue lactate values and arterial blood lactate values included probe movement due to hyperventilation episodes (brought on soon after switching inhaled gas from 100% oxygen to room air, see Fig. 5a) and sensors that became saturated. Three of the 11 implanted sensors had no sensitivity above 10 mM as evidenced by saturation at 10 mM in *in vitro* tests performed before implantation, and by a premature plateau of lactate concentration *in vivo* after rising (implanted sensor values leveled off while blood lactate continued to rise). When the data points affected by saturation and probe movement were removed the average error between blood lactate and implanted sensors was 11% with 84% of data within 20% (n=57) (shown as an error grid in Fig. 6b).

The time it took for our implanted sensor to respond with increasing lactate concentration to the cyanide infusion was calculated for each implanted sensor and the average response time was compared to the average response time of blood lactate increase, pH decrease, heart rate decrease, blood pressure decrease, and SpO_2 decrease. Table 1b shows the average response time after start of cyanide infusion for each measurement. Blood and tissue lactate were the first measurements to show a response to cyanide on average and blood lactate response was the most consistent (standard deviation of ±5.5 min).

The average response of any vitals measurements (HR, BP, SpO_2) was delayed at least 6.8 minutes from the response of blood lactate. Tissue lactate responded slightly earlier than blood lactate on average, though its response time was less consistent than blood lactate. The arterial blood pH took 32 minutes to respond to cyanide on average, compared to the quicker response of blood lactate or tissue lactate at around 18-19 minutes on average.

Discussion:

Cyanide poisoning causes a cellular metabolic shift, the degree of which can be quantified by measuring lactate concentration. This metabolic shift is also present in more common injuries and diseases including sepsis and various forms of shock. The need for medical intervention is clear for patients with elevated or rising blood lactate concentration, but blood lactate measurements are rarely taken at the point of care and it may take hours before the lactate level of a patient is known. Trends in lactate concentration indicate worsening (rising lactate) or improving patient condition (falling lactate) in a variety of critical care applications. A continuous lactate monitor can autonomously provide real-time lactate concentrations and information on trends that could be used to make treatment decisions. A clinical study has shown that treatment decisions based on frequent lactate measurements can improve survival rates (Jansen, 2010). We have completed a round of rabbit cyanide poisoning experiments using our implantable lactate sensors to track the increase of lactate due to cyanide poisoning and decrease in lactate due to recovery from cyanide poisoning in the case of an effective antidote drug. The studies show that the sensing and detection scheme that we have chosen works repeatedly *in vivo*, that our sensor design can be manufactured for multiple studies, and that implanted sensor measurements in animal subcutaneous tissue correlate well with blood lactate measurements. Additionally, we found that in recovery the implanted lactate sensor in the subcutaneous tissue responded to falling lactate values over 30 minutes before a decrease in blood lactate was observed. This is an indication that tissue lactate may provide an early confirmation of effective treatment as compared to blood lactate and warrants further investigation. Blood and tissue lactate responded to administration of cyanide before standard vital signs in rabbits. In humans this delay may be even more pronounced on larger timelines.

Some of the steps of the sensor manufacturing process were done by hand and may have high variability such as the amount of enzyme hydrogel loaded into the reaction chambers, or the thickness of the knife-coated silicone cap. These may be large contributing factors to the need for a two-point calibration in this study. With more precise manufacturing the sensors may be able to be calibrated with one blood lactate measurement upon insertion. Movement of the probes relative to the implanted sensors caused inaccuracies in the measured lactate values. The probes used were relatively large due to the size of the off-the-shelf amplified photodetector used and we were unable to align them to the implanted sensors without using a support rod fixed to the table. We have since developed a thin, light probe that can be taped to the skin, which will eliminate errors caused by probe movement relative to the sensor, and we plan to test it *in vivo*.

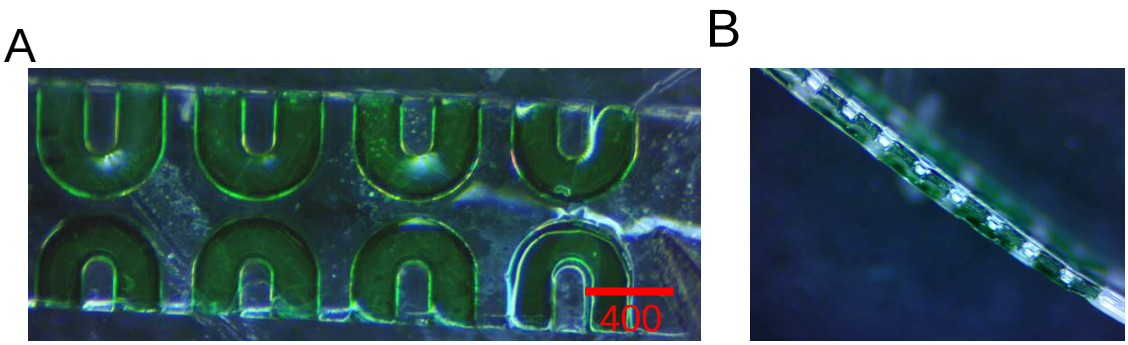

Fig. 1. The implantable sensor. (A) An array of reaction chambers filled with lactate-selective reagents. The chambers appear green due to the dye film coating. (B) Side view of the 200 µm thick sensor shows the open surfaces of the array of reaction chambers.

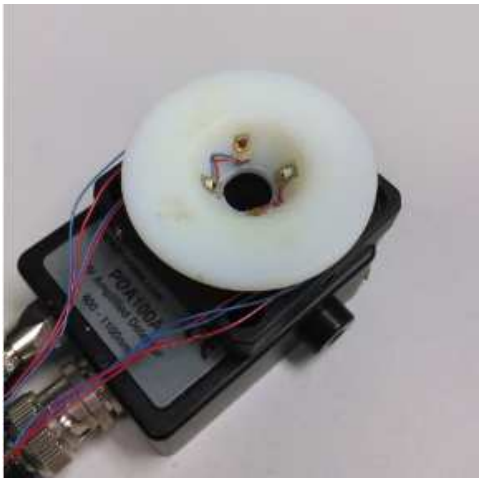

Figure 2. The probe: Lactate and oxygen sensitive lifetime measurements are made by exciting an implanted sensor with LED light and by collecting the sensor's excited light emission on a photodetector. A long-pass optical filter between the LEDs and detector is used to prevent LED light from saturating the detector. LEDs are attached to a custom 3D printed conical mount in order to aim their output light onto a sensor implanted in subcutaneous tissue.

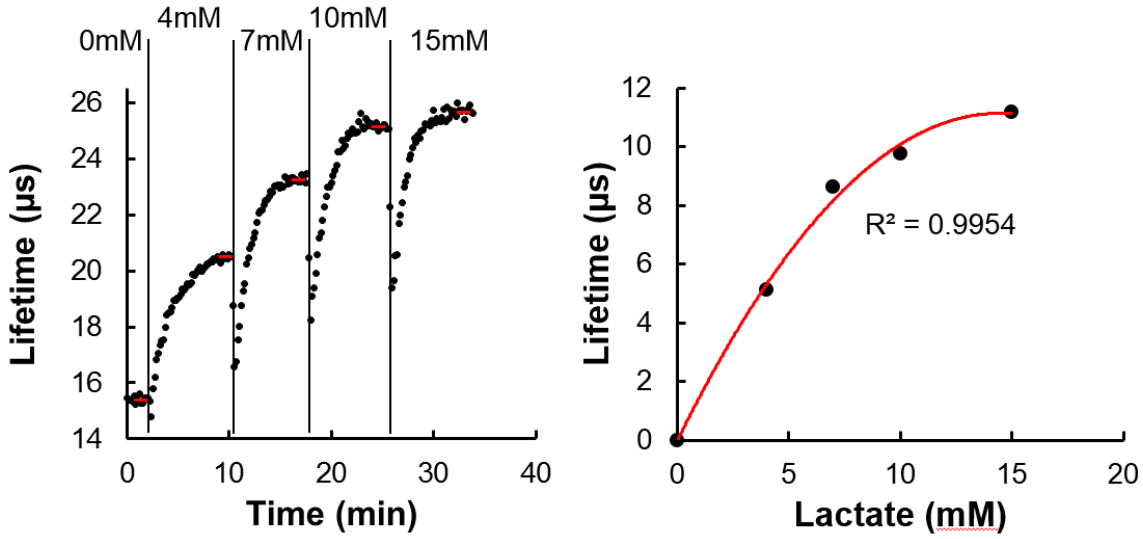

Figure 3. *In Vitro* Sensor Validation. (A) Lifetime measurements of a lactate sensor placed in a well of a 24 well plate are recorded every 10 seconds. Saline solutions containing increasing lactate concentrations were added to the well and the sensor steady state lifetime response for each concentration was recorded. (B) The constant oxygen lifetime value at 0mM lactate was subtracted from the steady state lifetime response values from (a) and a second order polynomial calibration curve was fit to the data ($R^2 > 0.99$).

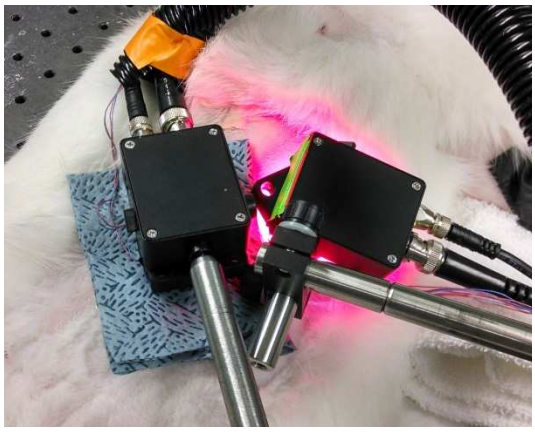

Figure 4. Probe Setup *In Vivo*: The probe on the right was aligned with the lactate sensor implanted in rabbit belly subcutaneous tissue, and the probe on the left was aligned with the implanted oxygen sensor.

Tissue Lactate (TL) vs. Blood Lactate (BL)	TL Low (mM)	BL Low (mM)	TL High (mM)	BL High (mM)	TL Rate of Increase (mM/min)	BL Rate of Increase (mM/min)
Average	2.43	2.65	15.77	15.49	0.26	0.250532
Standard Deviation	0.96	0.96	3.72	3.77	0.16	0.157867
% Difference	8.4%		1.8%		5.3%	

Table 1a, Tissue lactate measurements compared to blood lactate.

Time to response after start of cyanide infusion (min.)	IS	BL	pH	HR	BP	SpO2
Average	18.4	18.9	32.0	32.0	33.0	25.7
Standard Deviation	9.0	5.5	10.2	11.0	16.1	9.5
Delay From Blood Lactate Response	-0.5	0	13.1	13.1	14.1	6.8

Table 1b, Response time of indicators to cyanide poisoning.

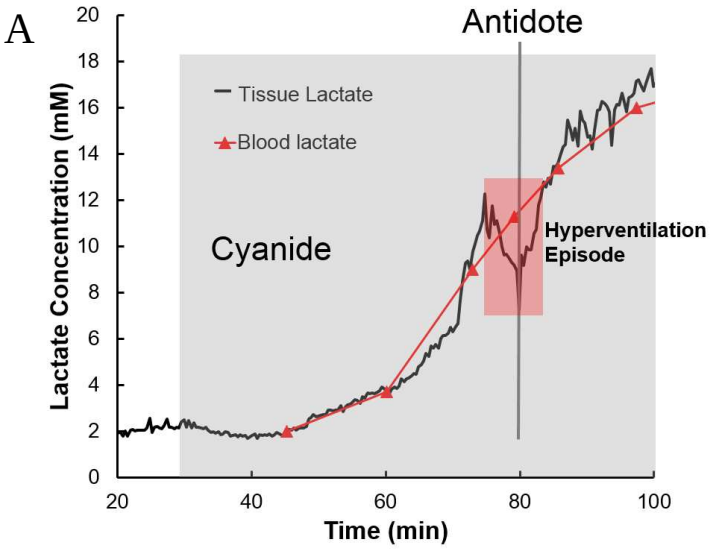

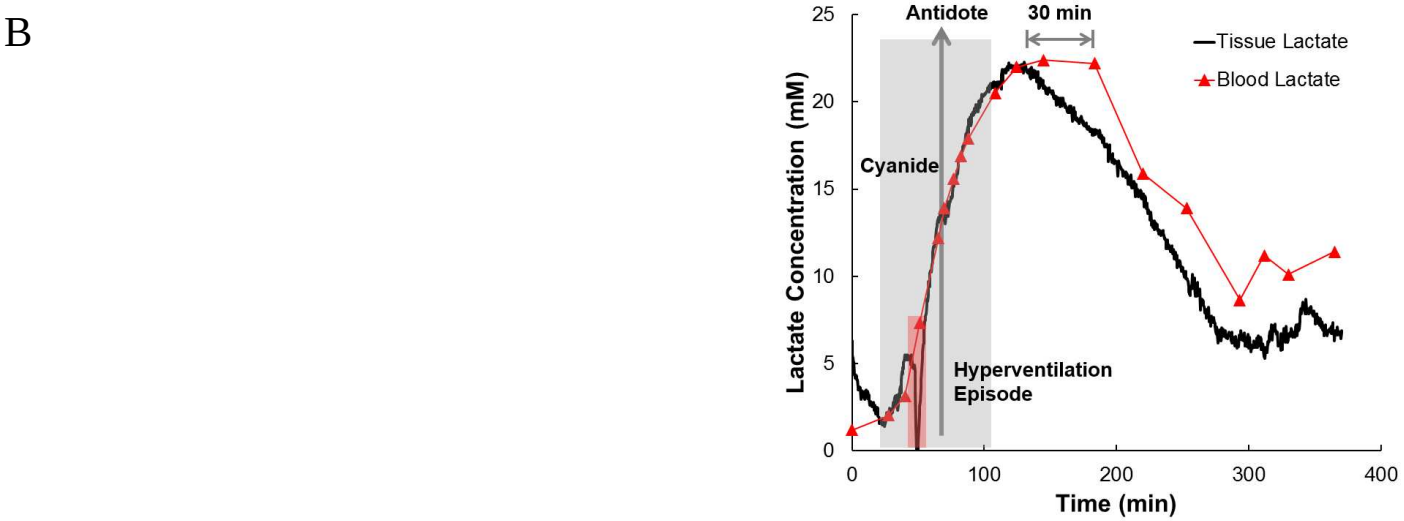

Figure 5. Sensor Performance *In Vivo*: (A) Non-survival example of a calibrated implanted lactate sensor (black) and blood lactate (red) response to cyanide poisoning. Movement of the probe relative to the sensor during a hyperventilation episode causes the implanted sensor response to drop for a short period (highlighted). (B) Survival and recovery example of a calibrated implanted lactate sensor (black) and blood lactate (red) response to cyanide poisoning. When the rabbit begins to recover the implanted sensor lactate response drops over 30 minutes before the blood lactate, providing an early indication of recovery.

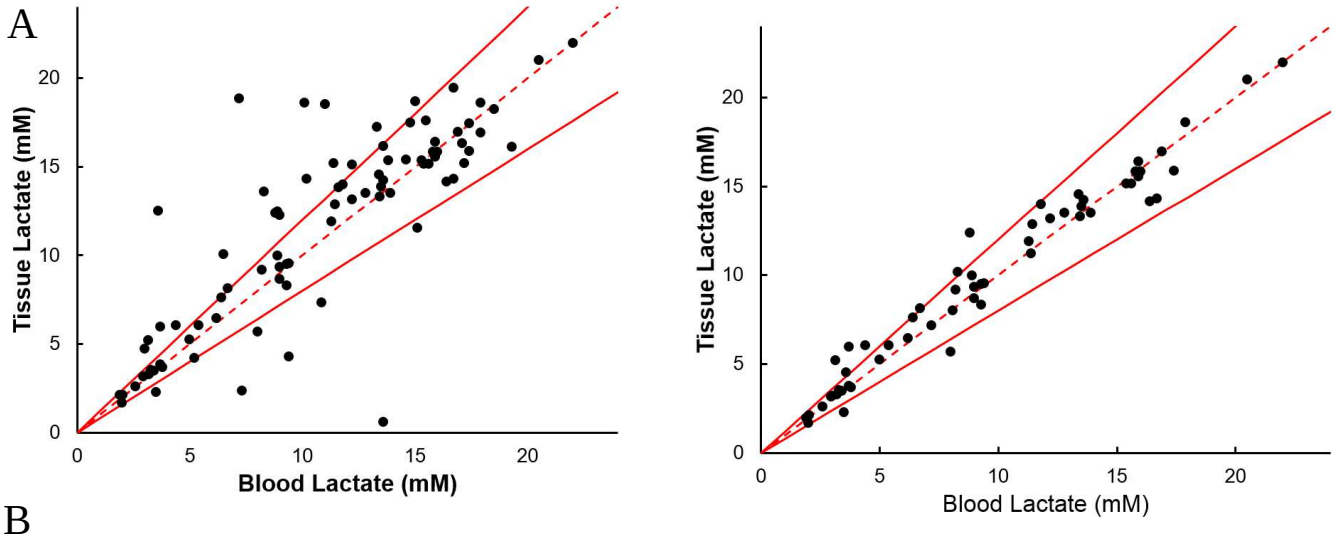

Figure 6: *In Vivo* Lactate sensor accuracy: Error grid comparing implanted sensor measured lactate to blood lactate. The dashed line indicates 100% agreement between the two readings and the lines on either side represent plus or minus 20% error between the two measurements. (A) All data besides warm-up time and falling lactate values included. (B) Data points after sensor saturation and during probe movement due to hyperventilation episodes removed.

References

1. Hall A H and Rumack B H 1986 Clinical toxicology of cyanide *Ann. Emerg. Med.* **15** 1067–74
2. Barillo D J, Goode R and Esch V 1994 Cyanide poisoning in victims of fire: analysis of 364 cases and review of the literature *J. Burn Care Rehabil.* **15** 46–57
3. Baud F J, Barriot P, Toffis V, Riou B, Vicaut E, Lecarpentier Y, Bourdon R, Astier A and Bismuth C 1991 Elevated blood cyanide concentrations in victims of smoke inhalation *N. Engl. J. Med.* **325** 1761–6
4. Riddle K 2004 Hydrogen cyanide: fire smoke's silent killer *J. Emerg. Med. Serv. JEMS* suppl 5 **29** 2
5. Strickland A,Wang R Y, Hoffman R S and Goldfrank L R 1992 Blood cyanide concentrations after smoke inhalation *N. Engl. J. Med.* **326** 1362
6. Graham D L, Laman D, Theodore J and Robin E D 1977 Acute cyanide poisoning complicated by lactic acidosis and pulmonary edema *Arch. Int. Med.* **137** 1051–5
7. Way J L, Leung P, Cannon E, Morgan R, Tamulinas C, Leong-Way J, Baxter L, Nagi A and Chui C 1988 The mechanism of cyanide intoxication and its antagonism *Ciba Found. Symp.* **140** 232–43
8. Brierley J B, Brown A W and Calverley J 1976 Cyanide intoxication in the rat: physiological and neuropathological aspects *J. Neurol. Neurosurg. Psychiatry* **39** 129–40
9. Groff W A Sr S F, Kaminskis A, Froehlich H l and Johnson R P 1985 Plasma free cyanide and blood total cyanide: A rapid completely automated microdistillation assay *Clin. Toxicol.* **23** 133–63
10. Jansen TC, et al. "Early lactate-guided therapy in intensive care unit patients: a multicenter, open-label, randomized controlled trial." *Am J Respir Crit Care Med*, 182(6)(2010):752–761.
11. Jones AE, et al. "Lactate clearance vs central venous oxygen saturation as goals of early sepsis therapy: a randomized clinical trial." *JAMA* 2010, 303(8):739–746.
12. Brohi K, Levy H, Boffard K, Riou B, Kiepert P, Zielske D. 643: Normalization of Lactate Within 8 Hours or a 20% Clearance in Initial 2 Hours Correlates With Outcomes From Traumatic Hemorrhagic Shock. Critical Care Medicine. 2011;39(12):177.
13. Hosogai N, Fukuhara A, Oshima K, Miyata Y, Tanaka S, Segawa K, Furukawa S, Tochino Y, Komuro R, Matsuda M. Adipose tissue hypoxia in obesity and its impact on adipocytokine dysregulation. Diabetes. 2007;56(4):901-11.
14. Bakker J, Gris P, Coffernils M, Kahn RJ, Vincent JL (1996) Serial blood lactate levels can predict the development of multiple organ failure following septic shock. Am J Surg 171:221–226
15. Nguyen HB, Rivers EP, Knoblich BP, Jacobsen G, Muzzin A, Ressler JA, Tomlanovich MC (2004) Early lactate clearance is associated with improved outcome in severe sepsis and septic shock. Crit Care Med 32:1637–1642
16. Bakker, Jan, Maarten WN Nijsten, and Tim C. Jansen. "Clinical use of lactate monitoring in critically ill patients." *Ann Intensive Care* 3.1 (2013): 12.
17. Hu, Yibai, Yanan Zhang, and George S. Wilson. "A needle-type enzyme-based lactate sensor for in vivo monitoring." *Analytica Chimica Acta* 281.3 (1993): 503-511.
18. Baker, Dale A., and David A. Gough. "A continuous, implantable lactate sensor." *Analytical Chemistry* 67.9 (1995): 1536-1540.
19. Berger, Andrew J., Yang Wang, and Michael S. Feld. "Rapid, noninvasive concentration measurements of aqueous biological analytes by near-infrared Raman spectroscopy." *Applied optics* 35.1 (1996): 209-212.

20. Sivakesava, Sakhamuri, Joseph Irudayaraj, and Demirci Ali. "Simultaneous determination of multiple components in lactic acid fermentation using FT-MIR, NIR, and FT-Raman spectroscopic techniques." *Process Biochemistry* 37.4 (2001): 371-378.
21. Tamburini, E., et al. "Near-infrared spectroscopy: a tool for monitoring submerged fermentation processes using an immersion optical-fiber probe."*Applied spectroscopy* 57.2 (2003): 132-138.
22. Jia, Wenzhao, et al. "Electrochemical tattoo biosensors for real-time noninvasive lactate monitoring in human perspiration." *Analytical chemistry*85.14 (2013): 6553-6560.
23. Kim, Jayoung, et al. "Non-invasive mouthguard biosensor for continuous salivary monitoring of metabolites." *Analyst* 139.7 (2014): 1632-1636.
24. Kocincova, Anna S., et al. "Fiber-optic microsensors for simultaneous sensing of oxygen and pH, and of oxygen and temperature." *Analytical chemistry* 79.22 (2007): 8486-8493.
25. Pasic, Alen, et al. "Miniaturized fiber-optic hybrid sensor for continuous glucose monitoring in subcutaneous tissue." *Sensors and Actuators B: Chemical* 122.1 (2007): 60-68.
26. Borisov, S. M., G. Nuss, and I. Klimant. "Red light-excitable oxygen sensing materials based on platinum (II) and palladium (II) benzoporphyrins." *Analytical chemistry* 80.24 (2008): 9435-9442.
27. Weidling, John, et al. "Method measuring oxygen tension and transport within subcutaneous devices." *Journal of biomedical optics* 19.8 (2014): 087006-087006.
28. Nielsen, Jannik K., et al. "Clinical evaluation of a transcutaneous interrogated fluorescence lifetime-based microsensor for continuous glucose reading."*Journal of diabetes science and technology* 3.1 (2009): 98-109.
29. Borisov, Sergey M., Gunter Zenkl, and Ingo Klimant. "Phosphorescent Platinum (II) and Palladium (II) Complexes with Azatetrabenzoporphyrins."New Red Laser Diode-Compatible Indicators for Optical Oxygen Sensing." *ACS applied materials & interfaces* 2.2 (2010): 366-374.

Chapter 4

Summary and Conclusion

A continuous lactate monitor would be transformative in the treatment of critically ill patients. Such a device would enable goal-directed treatment based on real time lactate concentrations. Importantly, such treatment has already been shown to significantly improve outcomes in critically ill patients. However, lactate guided treatment is rarely practiced due to the logistical burden of taking serial measurements using point-of-care devices or as part of a lab panel. We have developed a microchip device to continuously monitor lactate for the duration of inpatient care. Once proven for use in clinical applications, our device will enable lactate concentration goal-directed treatment.

I didn't initially set out to make a continuous lactate monitor when I began my graduate studies, but through a motivating seminar from a department official of the US Combat Casualty Care program and a comprehensive review of literature that supports the value of lactate in improving outcome and reducing mortality rates, the importance of continuous lactate monitoring was apparent. My initial work in the field of mechanobiology and biological imaging supported and advanced our understanding of capillary morphogenesis mechanics and made imaging of large fields of view of capillaries grown in culture possible. I gained experience in biosensing through an externship with a local small business, which would lay the foundation for the knowledge used to make a CLM. Once the goal of developing a CLM was established, my design approach was to use sensing techniques that would lead to accurate measurements *in vivo*. I found from reviewing the state of the art, and current research in lactate sensing, that non-invasive approaches to measuring lactate *in vivo* have not been proven accurate in the literature, and that commercially available

continuous sensors (continuous glucose monitors, CGMs) are not accurate enough to use as an indication to make treatment decisions, which will be necessary for a CLM to provide an advantage over current technology. The evidence suggests that the electrodes used in current CGMs suffer from drift and interferents *in vivo*, which may be the main cause of inaccuracy. Optical oxygen sensing using metalloporphyrins is suggested to have less interferents and exhibit less drift over time compared to electrodes. Optical sensing also opens the possibility of communicating with an implanted device through skin without the need for an electronic wireless communication signal that may require a power source within the body. Oxygen sensing allows for the use of an enzyme that reacts with lactate and oxygen (LOX) as the mediator, providing high selectivity for lactate. A device scheme whose invasiveness is similar to current CGMs, but uses an optical sensing technology reported to be more accurate and stable over time was chosen. A small, passive sensor would be placed just under the skin surface and light passed through skin would excite the sensor, causing lactate-mediated light to be emitted for detection by a probe placed on the skin surface above the implanted sensor.

Design of the measurement probe took advantage of the scattered light through tissue by capturing emitted light over a large surface area, rather than using a more complex optical focusing or fiber optic scheme. A breakthrough in sensor design was achieved when we realized that multiple small reaction chambers with highly controlled size and diffusional distances could be patterned onto one 'chip' to maintain the same response time and sensitivity range in each chamber, while multiplying the intensity of the signal returned through tissue. Reaction chamber patterns were formed using photolithographically formed molds leading to more repeatable sensor manufacture.

Once we had a repeatable manufacturing process I tested the sensors for use and accuracy *in vivo* in rabbit models of cyanide poisoning, where lactate concentrations cover the pathological range of values. This allowed me to quantify the accuracy of the sensors compared to gold standard measurements of blood lactate across the range of clinically expected concentrations. The results showed that in 12 *in vivo* experiments the average accuracy of our implanted CLMs were 89% compared to blood lactate measurements when errors due to movement and sensor saturation were removed. In comparison, CGMs on the market today have average accuracy of 80-85% compared to blood measurements. The next developmental step will correct the movement issue through a redesign of the probe such that it can be taped down to skin. Sensor saturation may be avoided through a more precise manufacturing process where no steps rely on hand-loading / manipulation.

Another interesting finding from the rabbit cyanide experiments was that in the case of recovery from cyanide exposure the lactate concentrations measured by our sensor implanted in the tissue drop about 30 minutes before blood lactate measurements. This indicates that measurements of lactate in tissue may provide an early indication of an effective treatment compared to blood measurements. There was only one observation of this leading indication of recovery in the experiments completed to date, but the promising result warrants further investigation.

Much work is still needed to get a CLM capable of directing therapies into clinical practice, but the observed *in vivo* accuracy of our current CLMs are a large step towards the realization of that goal. The implantable sensor portion will need to be shown to be biocompatible over the required implantation period to ensure that immune response and inflammation do not interfere with sensor use. Safe and accurate performance in clinical

studies will need to be proven, and a user friendly package for insertion, removal, and data collection / display will need to be designed before this potentially life-saving technology could be put to use. Other techniques for monitoring lactate continuously may be developed in the coming years as the importance of lactate levels in identification and treatment of critical patients has been identified in a large body of literature and most likely will continue to be confirmed in the clinical setting. While many theoretical techniques may be able to meet the goal of continuous lactate monitoring eventually, we have found a technique right now that has the potential to overcome the suspected shortcomings of current electrode technologies and have already shown it is accurate in an *in vivo* study.

While the ideal CLM would be completely non-invasive, our minimally invasive technology is much closer to clinical application in the critical patient population than any proposed non-invasive technique described in current literature. Monitoring techniques proposed for measuring lactate levels during exercise may work in an application where accurate measurement of lactate concentration that correlates with blood lactate concentrations is not needed. Critical care applications require that measurements accurately correlate with blood lactate concentration, and in this application the need for accurate results outweighs the desire of complete non-invasiveness.

Evidence suggests that serial point-of-care measurements of lactate concentration, possible with existing products, can save lives by directing therapeutic interventions. Why then are serial lactate measurements not a part of most treatment protocols? Clinical evidence of lactate concentration's power of prediction has been stacking up for over 50 years, but standard vitals monitoring provides the most widely available, easy to use systems. In wide

practice lactate is still thought of as a supplementary measurement that does not justify the burden of taking many blood draws with subsequent device measurements. A device, such as a CLM, that autonomously tracks lactate concentration, provides trends, and sounds alarms due to rapidly increasing lactate may change this perception, and if the evidence in the literature is true, the widespread use of CLMs would save thousands of lives every year. This work focused on lactate sensing due to its medical importance and existence of an unmet need in continuous sensing. The sensor design and measurement probe can also be used to measure other common analytes *in vivo*. We have shown that glucose can also be measured by swapping the LOX enzyme for GOX. Other immediately apparent analytes that could be measured using small modifications to our setup are CO_2 and pH. The sensor design described in this work is really a platform technology for measuring subcutaneous concentrations of multiple analytes, making it a more attractive approach than technologies that are capable of measuring only one analyte of interest.

References

ADA. (2008). Economic Costs of Diabetes in the U.S. in 2007. *Diabetes Care, 31*, 596-615.

Adrie, C., Adib-Conquy, M., Laurent, I., Monchi, M., Vinsonneau, C., Fitting, C., . . . Spaulding, C. (2002). Successful cardiopulmonary resuscitation after cardiac arrest as a "sepsis-like" syndrome. *Circulation, 106*(5), 562-568.

Andersen, L. W., Mackenhauer, J., Roberts, J. C., Berg, K. M., Cocchi, M. N., & Donnino, M. W. (2013). *Etiology and therapeutic approach to elevated lactate levels.* Paper presented at the Mayo Clinic Proceedings.

Angus, D. C., Linde-Zwirble, W. T., Lidicker, J., Clermont, G., Carcillo, J., & Pinsky, M. R. (2001). Epidemiology of severe sepsis in the United States: analysis of incidence, outcome, and associated costs of care. *Critical care medicine, 29*(7), 1303-1310.

Armour, J. C., Lucisano, J. Y., McKean, B. D., & Gough, D. A. (1990). Application of chronic intravascular blood glucose sensor in dogs. *Diabetes, 39*(12), 1519-1526.

Aslar, A. K., Kuzu, M. A., Elhan, A. H., Tanik, A., & Hengirmen, S. (2004). Admission lactate level and the APACHE II score are the most useful predictors of prognosis following torso trauma. *Injury, 35*(8), 746-752.

Baker, D. A., & Gough, D. A. (1995). A continuous, implantable lactate sensor. *Analytical chemistry, 67*(9), 1536-1540.

Bakker, J., Nijsten, M. W., & Jansen, T. C. (2013). Clinical use of lactate monitoring in critically ill patients. *Ann Intensive Care, 3*(1), 12.

Blevins, T. C., Bode, B. W., Garg, S. K., Grunberger, G., Hirsch, I. B., Jovanovič, L., . . . Tamborlane, W. V. (2010). Statement by the American Association of Clinical Endocrinologists Consensus Panel on continuous glucose monitoring. *Endocrine Practice, 16*(5), 730-745.

Brauker, J. (2009). Continuous glucose sensing: future technology developments. *Diabetes Technol Ther, 11 Suppl 1*, S25-36. doi: 10.1089/dia.2008.0137

Brown, A., Reynolds, L. R., & Bruemmer, D. (2010). Intensive glycemic control and cardiovascular disease: an update. *Nature Reviews Cardiology, 7*(7), 369-375.

CARE, P. (2003). Outpatient insulin therapy in type 1 and type 2 diabetes mellitus. *JAMA, 289*, 2254-2264.

Control, D., & Group, C. T. R. (1994). The Effect of Intensive Treatment of Diabetes on the Development and Progression of Long-term Complications in Insulin-dependent Diabetes Mellitus. *RETINA, 14*(3), 286-287.

Cowan, B., Burns, H., Boyle, P., & Ledingham, I. M. (1984). The relative prognostic value of lactate and haemodynamic measurements in early shock. *Anaesthesia, 39*(8), 750-755.

Danaei, G., Finucane, M. M., Lu, Y., Singh, G. M., Cowan, M. J., Paciorek, C. J., . . . Stevens, G. A. (2011). National, regional, and global trends in fasting plasma glucose and diabetes prevalence since 1980: systematic analysis of health examination surveys and epidemiological studies with 370 country-years and 2· 7 million participants. *The Lancet, 378*(9785), 31-40.

Deshpande, A. D., Harris-Hayes, M., & Schootman, M. (2008). Epidemiology of diabetes and diabetes-related complications. *Physical therapy, 88*(11), 1254-1264.

Dixon, B. M., Lowry, J. P., & O'Neill, R. D. (2002). Characterization in vitro and in vivo of the oxygen dependence of an enzyme/polymer biosensor for monitoring brain glucose. *Journal of Neuroscience Methods, 119*(2), 135-142.

Finkelstein, E. A., Corso, P. S., & Miller, T. R. (2006). *The incidence and economic burden of injuries in the United States*: Oxford University Press.

Garg, S., & Jovanovic, L. (2006). Relationship of Fasting and Hourly Blood Glucose Levels to HbA1c Values Safety, accuracy, and improvements in glucose profiles obtained using a 7-day continuous glucose sensor. *Diabetes Care, 29*(12), 2644-2649.

Garg, S., & Jovanovic, L. (2006). Relationship of fasting and hourly blood glucose levels to HbA1c values: safety, accuracy, and improvements in glucose profiles obtained using a 7-day continuous glucose sensor. [Multicenter Study]. *Diabetes Care, 29*(12), 2644-2649. doi: 10.2337/dc06-1361

Ghajar, C. M., Chen, X., Harris, J. W., Suresh, V., Hughes, C. C., Jeon, N. L., . . . George, S. C. (2008). The effect of matrix density on the regulation of 3-D capillary morphogenesis. *Biophysical journal, 94*(5), 1930-1941.

Gonzalez, M. J., G. Sanchez Benavides, JM Verdu Rotellar, M. Cladelles, J. Bruguera, S. Quinones, C. Enjuanes, J. Pena Casanova, and J. Comin Colet. . (2013). Cognitive impairment in heart failure: clinical and functional markers and vital status at 12 months follow-up. *European Heart Journal, 34*(1), 1518.

Green, J., Bishop, P., Muir, I., McLester Jr, J., & Heath, H. (2000). Effects of high and low blood lactate concentrations on sweat lactate response. *International journal of sports medicine, 21*(08), 556-560.
Hashimoto, M., Toshiro Ito, Yoshihiko Kurimoto, Ryo Harada, Nobuyoshi Kawaharada, and Tetsuya Higami. (2013). Preoperative arterial blood lactate levels as a predictor of hospital mortality in patients with a ruptured abdominal aortic aneurysm. *Surgery Today, 43*(2), 136-140.
Heinemann, L. (2008). Finger pricking and pain: a never ending story. *J Diabetes Sci Technol, 2*(5), 919-921.
Henry, C. (1998). Getting under the skin: implantable glucose sensors. *Analytical chemistry, 70*(17), 594A-598A.
Hill, D., & Fisher, M. (2010). The effect of intensive glycaemic control on cardiovascular outcomes. *Diabetes, Obesity and Metabolism, 12*(8), 641-647.
Hirsch, I. B. (2009). Realistic expectations and practical use of continuous glucose monitoring for the endocrinologist. *The Journal of Clinical Endocrinology & Metabolism, 94*(7), 2232-2238.
Hoeks, L. B., Greven, W. L., & de Valk, H. W. (2011). Real-time continuous glucose monitoring system for treatment of diabetes: a systematic review. [Review]. *Diabet Med, 28*(4), 386-394. doi: 10.1111/j.1464-5491.2010.03177.x
Jansen, T. C., van Bommel, J., & Bakker, J. (2009). Blood lactate monitoring in critically ill patients: A systematic health technology assessment*. *Critical Care Medicine, 37*(10), 2827-2839.
Jansen, T. C., van Bommel, J., Mulder, P. G., Rommes, J. H., Schieveld, S., & Bakker, J. (2008). The prognostic value of blood lactate levels relative to that of vital signs in the pre-hospital setting: a pilot study. *Crit Care, 12*(6), R160.
Jansen, T. C., van Bommel, J., Schoonderbeek, F. J., Sleeswijk Visser, S. J., van der Klooster, J. M., Lima, A. P., . . . Bakker, J. (2010). Early lactate-guided therapy in intensive care unit patients: a multicenter, open-label, randomized controlled trial. *American journal of respiratory and critical care medicine, 182*(6), 752-761.
Jia, W., Bandodkar, A. J., Valdes-Ramirez, G., Windmiller, J. R., Yang, Z., Ramirez, J., . . . Wang, J. (2013). Electrochemical tattoo biosensors for real-time noninvasive lactate monitoring in human perspiration. *Analytical chemistry, 85*(14), 6553-6560.
Kniazeva, E., Weidling, J. W., Singh, R., Botvinick, E. L., Digman, M. A., Gratton, E., & Putnam, A. J. (2012). Quantification of local matrix deformations and mechanical properties during capillary morphogenesis in 3D. *Integrative Biology, 4*(4), 431-439.
Kotlarchyk, M. A., Shreim, S. G., Alvarez-Elizondo, M. B., Estrada, L. C., Singh, R., Valdevit, L., . . . Botvinick, E. L. (2011). Concentration independent modulation of local micromechanics in a fibrin gel. *PloS one, 6*(5), e20201.
Kottmann, R. M., Kulkarni, A. A., Smolnycki, K. A., Lyda, E., Dahanayake, T., Salibi, R., . . . Hu, J. Z. (2012). Lactic acid is elevated in idiopathic pulmonary fibrosis and induces myofibroblast differentiation via pH-dependent activation of transforming growth factor-β. *American journal of respiratory and critical care medicine, 186*(8).
Kvist, P. H., Bielecki, M., Gerstenberg, M., Rossmeisl, C., JENSEN, H. E., Rolin, B., & Hasselager, E. (2006). Evaluation of subcutaneously-implanted glucose sensors for continuous glucose measurements in hyperglycemic pigs. *in vivo, 20*(2), 195-203.
Kvist, P. H., & Jensen, H. E. (2007). Recent advances in continuous glucose monitoring: biocompatibility of glucose sensors for implantation in subcutis. *J Diabetes Sci Technol, 1*(5), 746-752.
Levy, M. M. M., FCCP; Fink, Mitchell P. MD, FCCP; Marshall, John C. MD; Abraham, Edward MD; Angus, Derek MD, MPH, FCCP; Cook, Deborah MD, FCCP; Cohen, Jonathan MD; Opal, Steven M. MD; Vincent, Jean-Louis MD, FCCP, PhD; Ramsay, Graham MD. (2003). 2001 SCCM/ESICM/ACCP/ATS/SIS International Sepsis Definitions Conference. *Critical Care Medicine, 31*(4), 1250-1256.
Manikis, P., Jankowski, S., Zhang, H., Kahn, R. J., & Vincent, J.-L. (1995). Correlation of serial blood lactate levels to organ failure and mortality after trauma. *The American journal of emergency medicine, 13*(6), 619-622.
Mastrototaro, J., Shin, J., Marcus, A., & Sulur, G. (2008). The accuracy and efficacy of real-time continuous glucose monitoring sensor in patients with type 1 diabetes. [Evaluation Studies
Multicenter Study]. *Diabetes Technol Ther, 10*(5), 385-390. doi: 10.1089/dia.2007.0291
Mikkelsen, M. E., Shah, C. V., Meyer, N. J., Gaieski, D. F., Lyon, S., Miltiades, A. N., . . . Christie, J. D. (2013). The epidemiology of acute respiratory distress syndrome in patients presenting to the emergency department with severe sepsis. *Shock, 40*(5), 375-381.
Nguyen, H. B., Rivers, E. P., Knoblich, B. P., Jacobsen, G., Muzzin, A., Ressler, J. A., & Tomlanovich, M. C. (2004). Early lactate clearance is associated with improved outcome in severe sepsis and septic shock*. *Critical Care Medicine, 32*(8), 1637-1642.

Odom, S. R., Howell, M. D., Silva, G. S., Nielsen, V. M., Gupta, A., Shapiro, N. I., & Talmor, D. (2013). Lactate clearance as a predictor of mortality in trauma patients. *Journal of Trauma and Acute Care Surgery, 74*(4), 999-1004.

Oliver, N. S., Toumazou, C., Cass, A. E., & Johnston, D. G. (2009). Glucose sensors: a review of current and emerging technology. [Review]. *Diabet Med, 26*(3), 197-210. doi: 10.1111/j.1464-5491.2008.02642.x

Pasic, A., Koehler, H., Klimant, I., & Schaupp, L. (2007). Pasic A, Koehler H, Klimant I, Schaupp L. Miniaturized fiber-optic hybrid sensor for continuous glucose monitoring in subcutaneous tissue. *Sensors and Actuators B: Chemical, 2007*(1), 60-68.

Pasic, A., Koehler, H., Schaupp, L., Pieber, T. R., & Klimant, I. (2006). Fiber-optic flow-through sensor for online monitoring of glucose. [Research Support, Non-U.S. Gov't]. *Anal Bioanal Chem, 386*(5), 1293-1302. doi: 10.1007/s00216-006-0782-x

Patton, S. R., Eder, S., Schwab, J., & Sisson, C. M. (2010). Survey of insulin site rotation in youth with type 1 diabetes mellitus. [Research Support, N.I.H., Extramural

Research Support, Non-U.S. Gov't]. *J Pediatr Health Care, 24*(6), 365-371. doi: 10.1016/j.pedhc.2009.11.002

Pickup, J. C. (2004). Glucose sensors: present and future. *International Textbook of Diabetes Mellitus*.

Pickup, J. C., Hussain, F., Evans, N. D., & Sachedina, N. (2005). In vivo glucose monitoring: the clinical reality and the promise. *Biosensors and Bioelectronics, 20*(10), 1897-1902.

Sciences, N. I. o. G. M. (2014). Sepsis Fact Sheet. Retrieved from

Seo, S., Su, T.-W., Tseng, D. K., Erlinger, A., & Ozcan, A. (2009). Lensfree holographic imaging for on-chip cytometry and diagnostics. *Lab on a Chip, 9*(6), 777-787.

Shapiro, N. I., Howell, M. D., Talmor, D., Nathanson, L. A., Lisbon, A., Wolfe, R. E., & Weiss, J. W. (2005). Serum lactate as a predictor of mortality in emergency department patients with infection. *Annals of emergency medicine, 45*(5), 524-528.

Smith, I., Kumar, P., Molloy, S., Rhodes, A., Newman, P., Grounds, R., & Bennett, E. (2001). Base excess and lactate as prognostic indicators for patients admitted to intensive care. *Intensive care medicine, 27*(1), 74-83.

System, U. H. (2012). 2012 Community Trauma Report. Retrieved from

Trial, C. (2005). Intensive diabetes treatment and cardiovascular disease in patients with type 1 diabetes. *The New England journal of medicine, 353*(25), 2643.

Vadgama, P., & Desai, M. (1991). In vivo biosensors. *Biosensor Principles and Applications. New York: Dekkel*, 303-338.

van Everdinge, K. J., G. H. Visser, C. J. M. Klijn, L. J. Kappelle, and J. Van der Grond. (1998). Role of collateral flow on cerebral hemodynamics in patients with unilateral internal carotid artery occlusion. *Annals of Neurology, 44*(2), 167-176.

Vanni, S., Gabriele Viviani, Michele Baioni, Giuseppe Pepe, Peiman Nazerian, Filippo Socci, Maurizio Bartolucci, Marco Bartolini, and Stefano Grifoni. . (2013). Prognostic value of plasma lactate levels among patients with acute pulmonary embolism: the thrombo-embolism lactate outcome study. *Annals of emergency medicine, 61*(3), 330-338.

VINCENT, J.-L., DUFAYE, P., Berré, J., LEEMAN, M., DEGAUTE, J.-P., & KAHN, R. J. (1983). Serial lactate determinations during circulatory shock. *Critical Care Medicine, 11*(6), 449-451.

Vitek, V. L. A. D. I. M. I. R., and R. A. Cowley. (1971). Blood lactate in the prognosis of various forms of shock. *Annals of surgery 173*(2), 308.

Wang, J. (2008). Electrochemical glucose biosensors. *Chemical reviews, 108*(2), 814-825.

Weidling, J., Isikman, S. O., Greenbaum, A., Ozcan, A., & Botvinick, E. (2012). Lens-free computational imaging of capillary morphogenesis within three-dimensional substrates. *Journal of biomedical optics, 17*(12), 126018-126018.

Weidling, J., Sameni, S., Lakey, J. R., & Botvinick, E. (2014). Method measuring oxygen tension and transport within subcutaneous devices. *Journal of biomedical optics, 19*(8), 087006-087006.

Weinstein, R. L., Schwartz, S. L., Brazg, R. L., Bugler, J. R., Peyser, T. A., & McGarraugh, G. V. (2007). Accuracy of the 5-day FreeStyle Navigator Continuous Glucose Monitoring System: comparison with frequent laboratory reference measurements. [Comparative Study]. *Diabetes Care, 30*(5), 1125-1130. doi: 10.2337/dc06-1602

Wilson, G. S., & Gifford, R. (2005). Biosensors for real-time in vivo measurements. *Biosensors and Bioelectronics, 20*(12), 2388-2403.

Wilson, G. S., Zhang, Y., Reach, G., Moatti-Sirat, D., Poitout, V., Thevenot, D., . . . Klein, J. (1992). Progress toward the development of an implantable sensor for glucose. *Clinical Chemistry, 38*(9), 1613-1617.

WO, C. C., SHOEMAKER, W. C., APPEL, P. L., BISHOP, M. H., KRAM, H. B., & HARDIN, E. (1993). Unreliability of blood pressure and heart rate to evaluate cardiac output in emergency resuscitation and critical illness. *Critical care medicine, 21*(2), 218-223.